CHALMERS
UNIVERSITY OF TECHNOLOGY

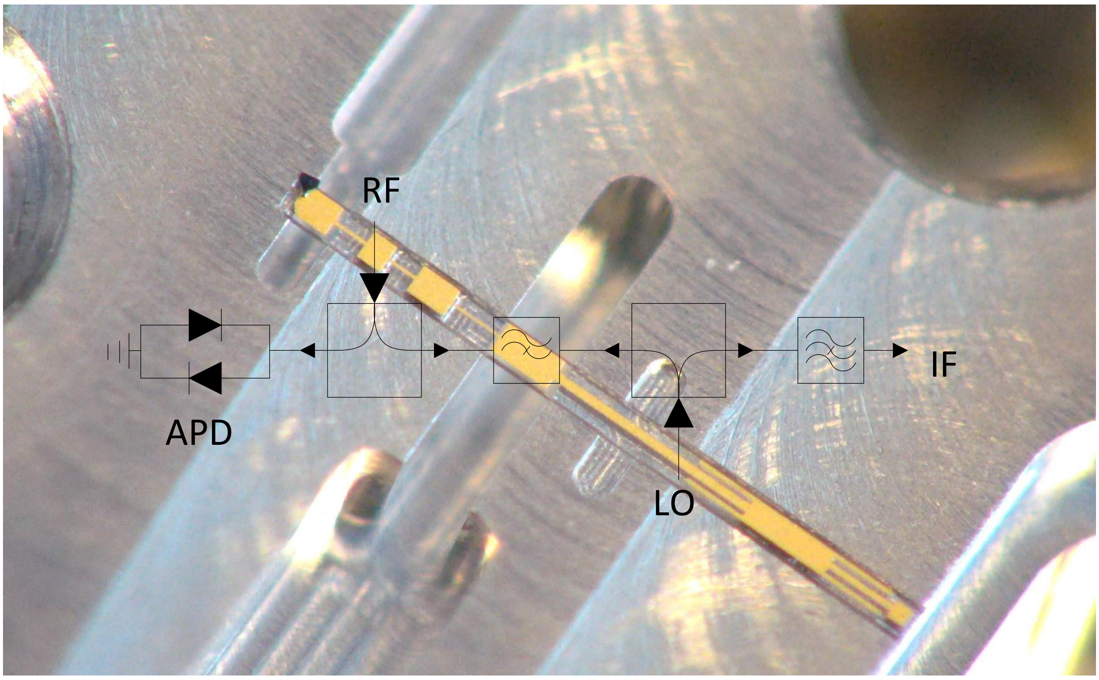

Design of a 183 GHz Subharmonic Mixer Using Membrane Integrated GaAs Schottky Diode Technology

Master's thesis in Wireless, Photonics and Space Engineering

MARTIN ANDERBERG

Department of Microtechnology and Nanoscience
CHALMERS UNIVERSITY OF TECHNOLOGY
Gothenburg, Sweden 2018

Design of a 183 GHz Subharmonic Mixer Using Membrane Integrated GaAs Schottky Diode Technology

MARTIN ANDERBERG

CHALMERS
UNIVERSITY OF TECHNOLOGY

Department of Microtechnology and Nanoscience
Terahertz and Millimetre Wave Laboratory
Chalmers University of Technology
Gothenburg, Sweden 2018

Design of a 183 GHz Subharmonic Mixer
Using Membrane Integrated
GaAs Schottky Diode Technology
MARTIN ANDERBERG

Supervisor: Peter Sobis, Omnisys Instruments AB
Examiner: Jan Stake, Terahertz and Millimetre Wave Laboratory

Department of Microtechnology and Nanoscience
Terahertz and Millimetre Wave Laboratory
Chalmers University of Technology
SE-412 96 Gothenburg
Telephone +46 31 772 1000

Cover: Photograph of a gold plated quartz substrate and a pair of antiparallel Schottky diodes mounted in an aluminium split-block cavity.

Typeset in LaTeX
Gothenburg, Sweden 2018

Design of a 183 GHz Subharmonic Mixer Using Membrane Integrated GaAs Schottky Diode Technology
MARTIN ANDERBERG
Department of Microtechnology and Nanoscience
Chalmers University of Technology

Abstract

Future ground based and space-borne meteorological instruments require sensitive heterodyne terahertz receivers in order to study precipitation and atmospheric temperature. Meteorological research is dependent on accurate water vapour measurements, typically performed with receivers at 183.3 GHz. These receivers require low noise mixers in order to meet the sensitivity requirement. At frequencies below approximately 400 GHz conventional mixers use flip-chip soldered discrete Schottky diodes. The flip-chip technique is unreliable and typically prohibits post-mount visual inspection of the diode anode, which is an important qualification step for space applications. Moreover, mechanical stresses introduced during the mixer circuit assembly can degrade the reliability. To overcome these problems a beamlead GaAs Schottky diode 183 GHz subharmonic mixer, implemented with a microstrip circuit topology, has been designed. The beamlead diode enables full visual inspection and the robust mounting of the microstrip circuit minimises the mechanical stress. Simulations showed a minimum conversion loss of 6.2 dB including conductor losses at a local oscillator frequency of 91 GHz and a power level of 2.5 dBm. The RF bandwidth was 15 % with a centre frequency of 183 GHz and the LO bandwidth was 6 % with a centre frequency of 91 GHz. The mixer was integrated with an IF LNA and measurements showed a state-of-the-art minimum receiver and mixer DSB noise temperature of 550 K and 400 K respectively at 1.6 mW of LO power which was in good agreement with the simulations.

Keywords: Schottky diodes, subharmonic mixer, thin film circuits, heterodyne receivers

Acknowledgements

Firstly I would like to express my sincere gratitude to my supervisor, Adj. Prof. Peter Sobis for happily sharing his expertise and for his guidance in the lab. I will remember the fruitful discussions about the different aspects of microwave design and especially our discussions about mixer noise. Secondly, I would like to thank my examiner, Prof. Jan Stake for his guidance regarding the planning report and the outline of this thesis.

I also want to thank the personnel at Omnisys Instruments AB where this thesis was carried out. Christina Emrich helped me with the mechanical design of the receiver, Daniel Ask milled the split-blocks with superior quality and Martin Petersson mounted the substrates and advised me about mixer assembly. Finally I would like to thank Slavko Dejanovic for letting me be part of the ALMA project team and Vladimir Drakinskiy at the Terahertz and millimetre wave laboratory for fabricating the diodes.

This research has been carried out in the GigaHertz Centre in a project financed by VINNOVA, Chalmers, Omnisys Instruments, Low Noise Factory, Wasa Millimeter Wave, and RISE.

Martin Anderberg, Gothenburg, June 2018

Contents

List of Figures

List of Tables

1 Introduction

1.1 Background

Climate change is an often discussed topic today and the request for meteorological data is increasing as scientists try to understand the mechanisms that drive the climate system. The meteorological research is dependent on ground based and space-borne sensitive instruments with high resolution in order to perform measurements on precipitation, snowfall, atmospheric temperature and the depth of the melting sea-ice [1], [2]. These measurements contribute to a deeper understanding of the present and future climate change.

Water vapour in the atmosphere is of great interest in meteorological research since it plays a major role in the Earth's radiative budget [3] and in the interaction between clouds and aerosols [4] but also since it is used to perform numerical weather forecasts through snowfall coverage imaging [1]. Water vapour can be measured by observing one of the two channels at 23.8 GHz and 183.3 GHz where the latter channel is 10 - 100 times more sensitive to water vapour compared to the 23.8 GHz channel. Receivers need to have high sensitivity when measuring snow fall coverage (high spatial resolution) [1] and when measuring the water vapour profile (high accuracy and temporal resolution) which can be used to calibrate instruments [5].

To obtain sensitive receivers at 183.3 GHz Schottky diode mixers are used as a first detection stage due to their low noise contribution [6]. Low noise amplifiers can also be used as a first detection stage but they have a higher equivalent noise temperature at room temperature in general [7]. The recent Schottky diode mixer designs at frequencies above 100 GHz and below 400 GHz use a so called flip-chip technique where the discrete diode is soldered upside down onto the circuit [8]–[10]. Furthermore, many designs use an inverted suspended microstrip topology where the circuit is glued upside down to minimise the electrical length to the DC-ground [8]–[10]. The diode and the circuitry in such designs cannot be visually inspected which is an important qualification step for space-borne receivers. It has also been observed that the suspended microstrip topology has a degraded reliability due to mechanically stressed substrates [10] making such a mixer hard to implement.

In this thesis is a visually inspectable mixer circuit topology presented which utilise the beamlead GaAs Schottky diode technology from Chalmers University of Technology. The non-flipped beamlead diode is in direct contact with the DC-ground and a modified microstrip topology has been implemented to obtain a relaxed substrate. The mixer design has shown to give low noise at 183 GHz making it suitable for water vapour measurements.

1.2 Summary of room temperature Schottky diode mixers

A summary of room temperature (RT) Schottky diode (SD) mixers is presented in Figure 1.1. Omnisys Instruments AB (Omnisys) has during the past 10 years delivered state-of-the-art receivers for frequencies from 300 GHz up to 1.2 THz [11], these receivers are seen in yellow triangles. The grey curve correspond to 50 times the minimum quantum noise limit, hf/k_B, (h is Planck's constant, f is the frequency and k_B is Boltzmann's constant) which represent the absolute minimum achievable noise. It can be seen that the mixers and receivers follow the grey curve and it is therefore expected that a mixer at 183 GHz should be able to give a noise temperature of 400 K which has not been shown [6], [12].

The increase in noise can be explained by many factors. The parasitic capacitance in the diode becomes more prominent at higher frequencies which decrease the intrinsic cut-off frequency. To compensate for this the diode must be made smaller but this increases the series resistance which then contribute with a higher thermal noise [13]. The resistance of the diode is frequency dependent as well [14].

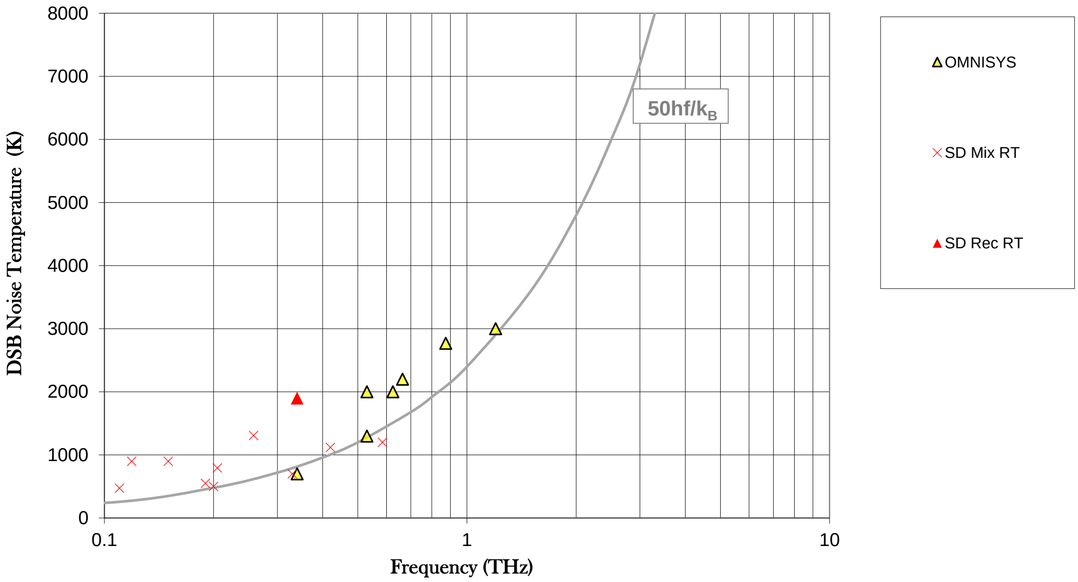

Figure 1.1: A summary of Schottky diode (SD) mixers and receivers at room temperature (RT) as illustrated in [11]. The results are based on [6], [9], [12], [15]–[24].

1.3 Aim

The thesis aims to investigate how a subharmonic Schottky diode mixer at room temperature should be designed to

- exhibit a low double-sideband noise temperature ($T_{DSB} < 1000\,\mathrm{K}$) at a radio frequency of 183 GHz,
- exhibit high repeatability and high reliability,
- provide visual inspection of the diode and the circuit.

1.4 Limitations

The manufacturing and the mechanical computer-aided design of waveguide blocks is outside the scope of this thesis. The Schottky diode used in the mixer will be based on existing planar antiparallel diodes fabricated at Chalmers University of Technology. Measurements to characterise the mixer performance will not be performed.

1.5 Outline of the thesis

The thesis starts with a theory chapter where the planar Schottky diode is introduced and the fundamental mixer theory is presented. A literature study of Schottky diode mixers is also included. Chapter 3 presents the proposed circuit topology and continues with a description of the mixer design. In chapter 4 are the results of simulations and fabrication presented. Future work is presented in chapter 5 where the thesis also is discussed. The conclusion is finally presented in Chapter 6.

2
Theory

This chapter introduces the Schottky diode, used in the designed mixer. This is followed by the fundamental mixer theory. Finally this chapter is summarised with a literature study of Schottky diode mixers.

2.1 The Schottky diode

A Schottky diode is a diode with a semiconductor-metal junction. The name has been awarded to Walter Schottky who worked with metal-semiconductor interfaces back in the 1930's and 40's [25]. The basic structure of the Schottky diode is seen in Figure 2.1 where the junction is seen and the depletion region which is formed when the two materials are connected to each other. When building Schottky diodes different semiconductors can be used. Gallium arsenide (GaAs), silicon (Si), gallium nitride (GaN) and indium phosphide (InP) are examples of commonly used semiconductors. The metal can be titanium (Ti), platinum (Pt), chromium (Cr) and various alloys [14]. The diode used in this thesis uses a GaAs semiconductor together with a Titanium-Platinum-Gold metal interface.

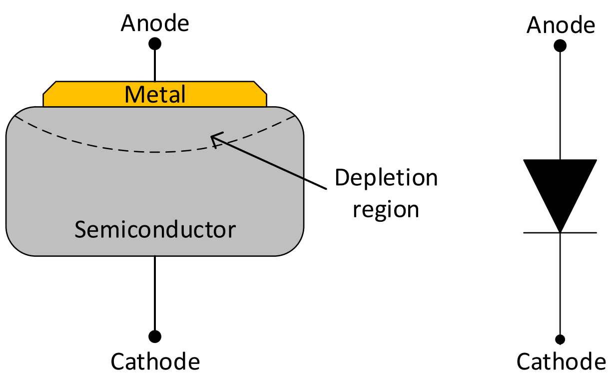

Figure 2.1: The basic structure of a Schottky diode and the symbol.

The energy-band diagram of the ideal Schottky junction is shown in Figure 2.2 where the width of the depletion region, w_d, is seen. When the metal is in contact with the semiconductor a potential barrier is created labelled as Ψ_{bi}. The barrier prevents the electrons to flow from the semiconductor to the metal. Φ_b is the barrier height which is around 0.8 V for a metal-GaAs junction [26]. E_C is the bottom energy level of the conduction band and E_V is the top energy level of the valence band. The bandgap of the semiconductor is labelled as E_g and the Fermi energy is E_F. If a forward voltage is applied to the junction, V_j, the potential barrier, Ψ_{bi}, is reduced and electrons start to flow from the semiconductor to the metal. The resistance of the junction is then a function of the junction voltage, a higher voltage gives a lower resistance. If a reverse voltage is applied the potential barrier and the depletion width are increased. In this case the junction act as a voltage dependent capacitor [27].

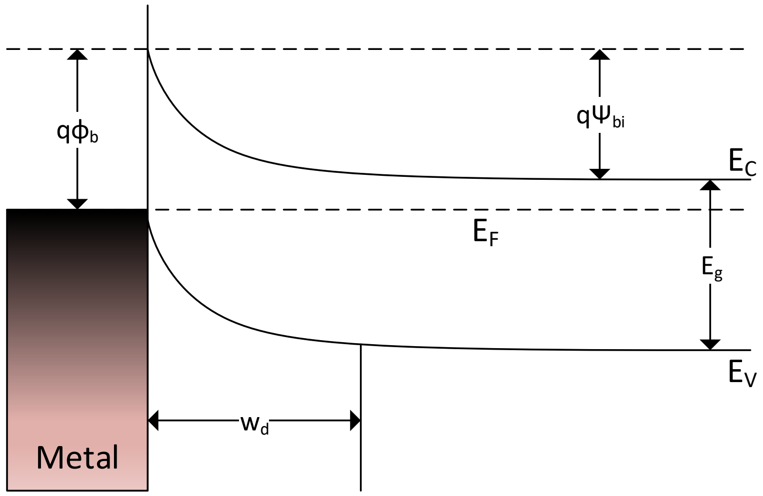

Figure 2.2: The energy-band diagram of the ideal Schottky contact where the depletion region w_d is seen. Φ_b is the barrier height, Ψ_{bi} is the built in potential, E_F is the Fermi energy, E_C is the bottom energy of the conduction band, E_V is the top energy level of the valence band and E_g it the bandgap energy. q is the elementary charge.

A fabricated Schottky diode will have parasitic elements such as resistances and capacitances. The junction itself is a resistance often denoted as $R_{epi}(V_j)$ and due to the depletion region the junction also has an associated capacitance, $C_j(V_j)$, [13], [14]. The equivalent circuit of a Schottky diode is shown in Figure 2.3 where the junction capacitance and the series resistance $R_s(V_j, f)$ is included. The epilayer resistance, R_{epi} is included in the series resistance which depends on both the junction voltage V_j and on the frequency f due to the skin effect [13]. The current voltage relationship for a Schottky diode is given by [27]

$$I_j(V_j) = I_S\Big(e^{\frac{qV_j}{\eta k_B T}} - 1\Big) \tag{2.1}$$

where

$$I_S = AA^{**}T^2 e^{\frac{-q\Phi_b}{k_B T}}, \tag{2.2}$$

I_j = junction current,
I_S = reverse saturation current,
q = elementary charge (1.6 x 10^{-19} C),
η = ideality factor,
A = Schottky anode junction area,
A^{**}= effective Richardson's constant,
Φ_b = barrier height ($\approx 0.8\,\mathrm{V}$ for a metal-GaAs junction [26]),
T = absolute temperature,
k_B = Boltzmanns's constant (1.37 x 10^{-23} J/K).

The ideality factor is ideally unity but due to tunnelling electrons this factor increase to 1.3 - 1.4 [14]. The series resistance in the equivalent circuit will dissipate power and thereby stop power from reaching the junction. The intrinsic cut-off frequency of the diode is given by [13]

$$f_c = \frac{1}{2\pi R_s C_j} \tag{2.3}$$

showing that a high series resistance and junction capacitance degrade the high frequency performance of the mixer [13] and it is therefore necessary to keep the resistance and capacitance low. The mixer designed in this thesis is a resistive mixer which means that the diode is used in the forward direction where it act as a non-linear resistance.

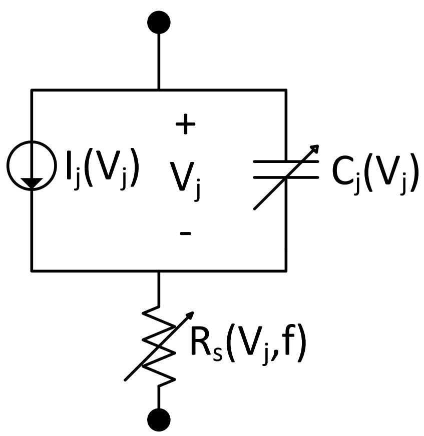

Figure 2.3: Equivalent circuit of the Schottky diode where the junction capacitance and the series resistance is included.

2.1.1 The planar Schottky diode

For high frequency applications whisker contacted diodes were used for many years but these diodes had reliability problems [15], [28]. Planar Schottky diodes, which is used in this thesis, is more reliable and easier to mount [14]. Among planar Schottky diodes the surface-channel type offers the lowest possible parasitic capacitance [29]. These diodes has an air channel and a bridge (often called a finger) which makes it possible to connect the outer circuitry to the anode of the diode. Figure 2.4 shows the planar Schottky diode with the parasitic resistances and capacitances [14]. The ohmic contact at the cathode and the resistance in the buffer layer forms the series resistance together with the epilayer resistance R_{epi}. The finger creates a series inductance and a finger resistance and between the finger and the semiconductor is a parallel capacitance introduced. The capacitances together with the inductance limits the power coupling to the diode junction thereby reducing the bandwidth of the mixer [14].

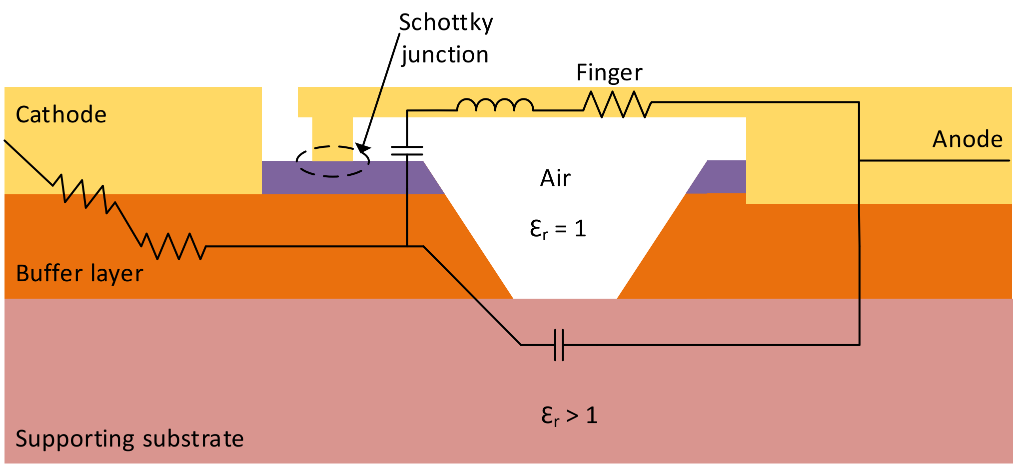

Figure 2.4: A planar Schottky diode with a surface channel and a finger as illustrated in [14].

2.2 Mixer theory

A mixer is a device that converts a signal to a higher frequency (upconverting mixer) or to a lower frequency (downconverting mixer). The first one is used in transmitters in various applications and the latter one is applied in different kind of receivers. The frequency conversion is possible due to the fact that the mixer is a non-linear device meaning that an input signal with a certain frequency can be transformed to other frequencies, to achieve this a non-linear element is required such as a diode or transistor.

To understand the principle of a mixer consider a device with two input signals, the local oscillator (LO) and the radio frequency (RF) signal. These signals have a frequency of $\omega_{LO} = 2\pi f_{LO}$ and $\omega_{RF} = 2\pi f_{RF}$ respectively. The non-linear behaviour of a mixer can be described by a simple multiplication,

$$v_o = v_{LO}v_{RF} = \Big[V_{LO}\cos\omega_{LO}t\Big]\Big[V_{RF}\cos\omega_{RF}t\Big] \tag{2.4}$$

where V_{LO} and V_{RF} is the amplitude of the LO and the RF signal respectively. By using the well known trigonometric identity,

$$\cos x \cos y = \frac{1}{2}(\cos(x-y) + \cos(x+y)) \tag{2.5}$$

the output voltage, v_o, becomes

$$v_o = \frac{V_{LO}V_{RF}}{2}\Big(cos(\omega_{LO} - \omega_{RF})t + cos(\omega_{LO} + \omega_{RF})t\Big). \tag{2.6}$$

It is here seen that the mixer produces two frequency components in the output signal $\omega_{IF} = \omega_{RF} - \omega_{LO}$, where IF stands for the intermediate frequency and $\omega_{sum} = \omega_{LO} + \omega_{RF}$. The IF signal is used in receivers and ω_{sum} is filtered. It can now be concluded that the mixer is a three-port device with two inputs and one output which explains its symbol seen in Figure 2.5.

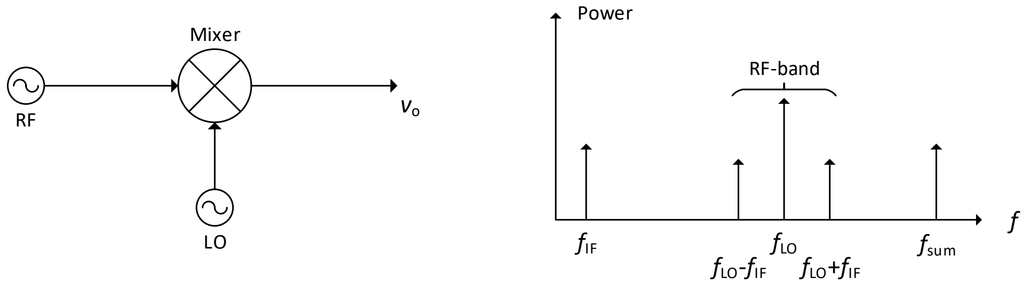

Figure 2.5: The symbol of a mixer in a receiver configuration and the spectral content of the output signal v_o.

It can be seen from (2.6) that if f_{RF} equals $f_{LO} - f_{IF}$ or $f_{LO} + f_{IF}$ both these cases downconverts to the same IF. These frequencies are called the lower sideband $f_{LSB} = f_{LO} - f_{IF}$ and the upper sideband $f_{USB} = f_{LO} + f_{IF}$ respectively. In a double-sideband (DSB) mixer both these bands are used and the RF-band is symmetric around the LO signal as seen in Figure 2.5. In a single-sideband (SSB) mixer either the upper sideband or the lower sideband is used, the unused sideband is then called the image frequency. The mixer in this thesis is a double-sideband mixer.

One of the most important figure of merits of a mixer is the conversion loss, it is defined as [30]

$$L_c = 10 \log \frac{\text{available RF input power}}{\text{available IF output power}} \qquad [\text{dB}] \tag{2.7}$$

and thereby quantifies the power conversion from the RF signal to the IF signal. Other important parameters for a double-sideband mixer is the mixer noise, the conversion loss flatness, sideband balance, LO power and spurious generation. The LO power becomes most critical for high frequency applications since it is harder to generate power. The sideband balance (SBB) describes the conversion symmetry around the LO frequency. It is defined as,

$$SBB = 10 \log \left| \frac{L_{c,LSB}}{L_{c,USB}} \right| \qquad [\text{dB}]. \tag{2.8}$$

2.2.1 Mixer noise

The noise produced by a mixer is, together with the conversion loss, the most important figure of merit. The non-linear element (e.g a diode) produces noise as well as the thermal sources due to resistive losses which adds up and become an added noise, N_{added}. Depending on if the mixer is a single-sideband or a double-sideband mixer the noise figure changes by a factor of 2 [30]. This can be shown by investigating the input signals and the output signals of the two cases and using the definition of noise figure [30]. An expression for the noise figure is given by Pozar [30],

$$F_{DSB} = \frac{2}{K^2 L_c} \left(1 + \frac{N_{added}}{k_B T_0 B} \right) = \frac{1}{2} F_{SSB} \tag{2.9}$$

where K accounts for the conversion loss at each sideband, $T_0 = 290\,\text{K}$ and B is the bandwidth.

In a diode mixer exists two main noise contributions, shot-noise and thermal noise. The shot-noise is due to the discrete nature and random variations of electrons passing through the Schottky contact. For a DC-biased diode the shot-noise is Gaussian with a mean-square current amplitude given by [31]

$$\overline{i_s^2} = 2qI_jB. \tag{2.10}$$

The noise source producing the shot-noise current can be seen as a current source in parallel with junction current I_j in Figure 2.3. The thermal noise is associated with the series resistance R_S and can be modelled as a voltage source in series with R_S. The mean square voltage amplitude of the thermal noise is given by [32], [33]

$$\overline{v_n^2} = 4k_BBTR \tag{2.11}$$

where R is a resistance. Since the thermal noise and shot-noise are uncorrelated their contributions can be added together, however when calculating their respectively contributions the correlation between the noise currents at the different frequencies must be accounted for [34]. For the shot-noise this is due to the fact that the diode is pumped by the LO meaning that the junction current, I_j, becomes a function of time which implies that the shot noise is not Gaussian distributed. Instead the shot-noise becomes a periodically amplitude modulated Gaussian noise [35].

2.2.1.1 Noise temperature of an ideal mixer

In [36], Saleh presents a noise figure calculation which applies for a mixer with an ideal exponential diode where all the undesired (out-of-band) frequencies are terminated reactively and R_s is neglected. Then the shot-noise is the only noise contribution and the noise figure is given by

$$F_{DSB} = \frac{1}{2}L_c + 1. \tag{2.12}$$

This is an interesting result since it shows that

$$T_{mix} = (F-1)T_0 = \frac{1}{2}L_c T_0. \tag{2.13}$$

By translating this temperature to the output of the mixer it is seen that

$$T_{mix,IF} = \frac{T_{mix}}{L_c} = \frac{1}{2}T_0. \tag{2.14}$$

This result shows that the total noise (shot-noise) of an ideal mixer with an ideal diode is equal to the noise from a resistance with half the temperature. The minimum mixer noise temperature is therefore 145 K in room temperature. In a practical mixer this temperature will not be reached due to the series resistance which adds thermal noise. In a subharmonic mixer which use two diodes this result still applies [37].

2.2.2 Resistive mixers

Mixers using a non-linear resistance are categorised as resistive mixers, however reactive elements are present as well but these are referred to as the parasitic elements of the mixer [36]. In practise the diodes operate in a mix of varistor and varactor mode since for example a Schottky diode, depending on the operating point, is both a varistor and a varactor [14]. The general theory of resistive mixers is presented by Saleh in [36] where four types of mixers are given labelled as Z-, Y-, G-and H-mixers. The difference between these mixers is the termination of the out-of-band frequency components at the input and the output of the mixer. Ideally all the out-of-band components should be terminated with a short or open circuit, obviously this will not be the case in a practical mixer and this will degrade the mixer performance [36].

The Z-mixer is a mixer where the out-of-band components are open-circuited [36], it can be illustrated with the circuit in Figure 2.6 where the filters on the input and output provides the open circuits for every frequency except for ω_{RF} and ω_{IF}. For the Y-mixer, all the out-of-band frequencies are terminated with a short-circuit illustrated by the circuit in Figure 2.7 where the time dependent resistor has been replaced with a time dependent conductance, $g(t)$. In order to analyse the mixer it is considered to be a linear time-invariant network with an infinite number of ports where each port represent a frequency component. Considering only the IF and RF frequencies the equation for the Z-mixer becomes [36],

$$\begin{bmatrix} V_{RF} \\ V_{IF} \end{bmatrix} = \overline{Z} \begin{bmatrix} I_{RF} \\ I_{IF} \end{bmatrix} = \begin{bmatrix} r_0 & r_1 \\ r_1^* & r_0 \end{bmatrix} \begin{bmatrix} I_{RF} \\ I_{IF} \end{bmatrix} \tag{2.15}$$

where r_0 is the resistance relating the RF voltage to the RF current and r_1 is the resistance relating the IF voltage to the RF current. If the image frequency is considered to be in-band then (2.15) expands and the Z-matrix becomes a 3x3 matrix relating the voltages at RF, image and IF to the currents. For the Y-mixer the equation becomes [36],

$$\begin{bmatrix} I_{RF} \\ I_{IF} \end{bmatrix} = \overline{Y} \begin{bmatrix} V_{RF} \\ V_{IF} \end{bmatrix} = \begin{bmatrix} g_0 & g_1 \\ g_1^* & g_0 \end{bmatrix} \begin{bmatrix} V_{RF} \\ V_{IF} \end{bmatrix}. \tag{2.16}$$

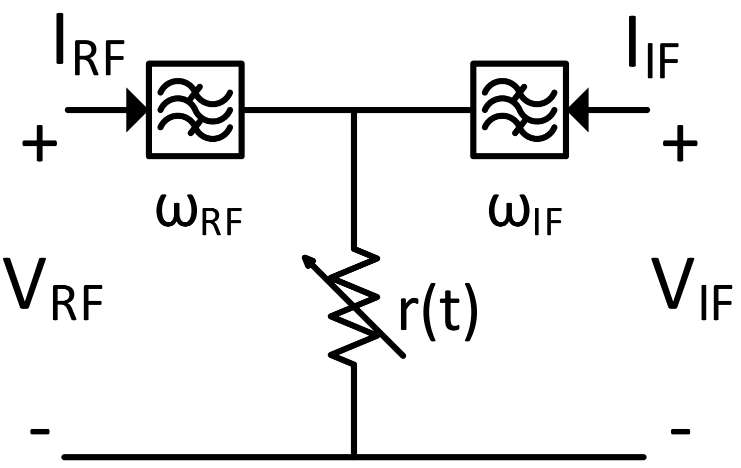

Figure 2.6: The Z-mixer as described by Saleh in [36]. The out-of-band frequencies are open-circuited and the RF and IF signals are not affected by the bandpass filters.

Depending on which type of mixer being used different performances are obtained. However all the mixer types have a minimum conversion loss of unity (0 dB) if the series resistance is neglected and all the out-of-band frequencies are terminated reactively [36]. In this thesis the Z-mixer and the Y-mixer will be considered as they represent the most basic mixers. It will also be presented later that these mixers represents the best and worst case when analysing a mixer with a diode as non-linear element. The theory presented follows the work of Saleh in [36]

Given a mixer type, such as the Y-mixer or the Z-matrix, one can find the optimum conductance (resistance) waveform that gives the minimum conversion loss [36]. The

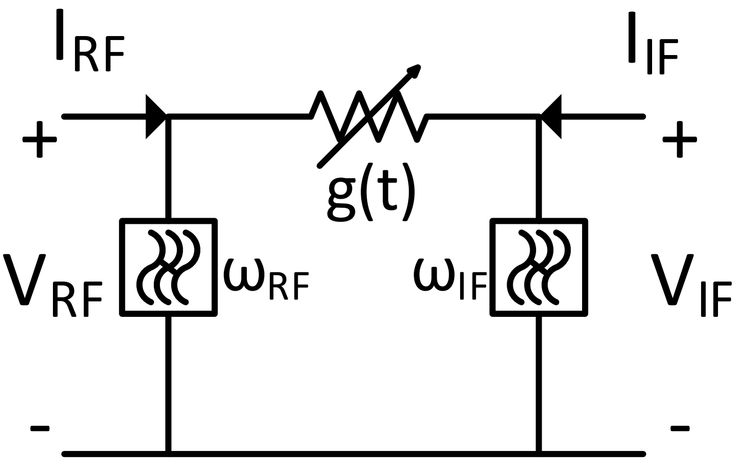

Figure 2.7: The Y-mixer as described by Saleh in [36]. The out-of-band frequencies are short-circuited and the RF and IF signals are open circuited at the bandstop filters.

optimum conversion loss, obtained when the input and output are matched with their conjugates, can be expressed as

$$L_{opt} = \frac{1+\sqrt{1-\epsilon}}{1-\sqrt{1-\epsilon}} \tag{2.17}$$

where

$$\epsilon = (\frac{g_1}{g_0})^2. \tag{2.18}$$

The variables g_0 and g_1 is the first and second term in the infinite series that describes the time dependent conductance,

$$g(t) = g_0 + 2g_1 \cos(\omega_{LO} t) + ... \tag{2.19}$$

It is clear that in order to minimise the conversion loss the ratio between g_1 and g_0 must be maximised. The solution to this problem is given by,

$$g(t) = \begin{cases} G_{max} & , |t| \leq \Delta/2\omega_{LO} \\ G_{min} & , |t| \leq \pi/\omega_{LO} \end{cases} \tag{2.20}$$

where Δ is the solution to the transcendental equation,

$$\tan(\Delta/2) = \frac{\Delta}{2} + \frac{\pi G_{min}}{G_{max} - G_{min}}. \tag{2.21}$$

Rewriting the expression for the conversion loss gives,

$$L_{opt} = \frac{1+\sin(\Delta/2)}{1-\sin(\Delta/2)}. \tag{2.22}$$

Equation (2.20) gives the optimum conductance waveform for the Y-mixer, it is a square wave with a maximum value of G_{max} and a minimum value of G_{min}. The waveform is seen in Figure 2.8, it is periodic with a period of $2\pi/\omega_{LO}$. The optimum conversion loss obtained with this waveform is plotted versus the ratio G_{min}/G_{max} in Figure 2.9 where it is seen that $L_{opt} \to 0$ when $G_{min}/G_{max} \to -\infty$. The duty cycle is also plotted and is expressed as

$$D = \frac{\Delta/\omega_{LO}}{2\pi/\omega_{LO}} = \frac{\Delta}{2\pi} \tag{2.23}$$

which is deduced from the conductance waveform in Figure 2.8. An approximate expression for the conversion loss is given by [36]

$$L_{opt} \approx 18.3\left(\frac{G_{min}}{G_{max}}\right)^{1/3} \qquad [\mathrm{dB}]. \tag{2.24}$$

From the above it can be concluded that the Y-mixer should have a non-linear element giving a small G_{min}/G_{max} ratio and that the mixer should be pumped such that the conductance varies as a square wave with a low duty cycle. The same conclusion applies for the Z-mixer since it is the dual case. Saleh [36] gives the proof of the Z-mixer and the resulting waveform is a square wave as the one seen in Figure 2.8 but with a maximum value of $R_{max} = 1/G_{min}$ and a minimum value of $R_{min} = 1/G_{max}$.

The simulated resistance waveform of the diode used in this thesis is seen in Figure 2.10, it is quite similar to a square wave with low duty cycle. Using the maximum and minimum resistance values of this curve gives

$$L_{opt} \approx 18.3\left(\frac{R_{min}}{R_{max}}\right)^{1/3} = 1.6\,\mathrm{dB} \tag{2.25}$$

indicating a mixer with low conversion loss. Due to practical limitations together with non-terminated frequency components and a non-zero series resistance the conversion loss will become higher.

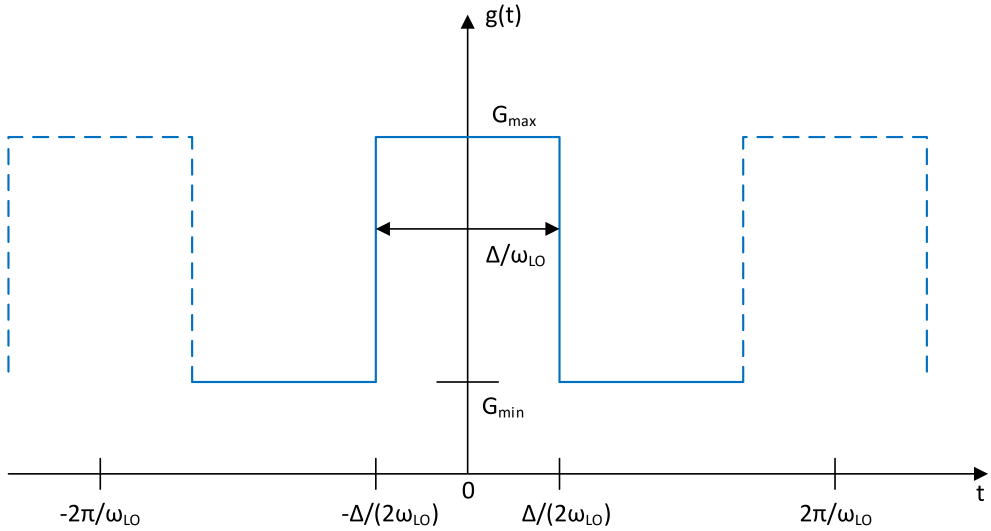

Figure 2.8: Optimum conductance waveform for the Y-mixer.

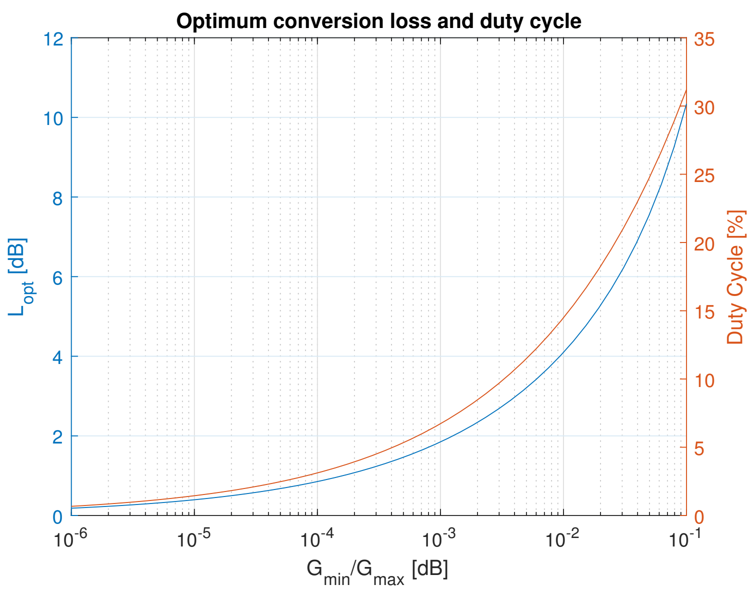

Figure 2.9: Optimum conversion loss for the Y-mixer. The corresponding duty cycle is also plotted.

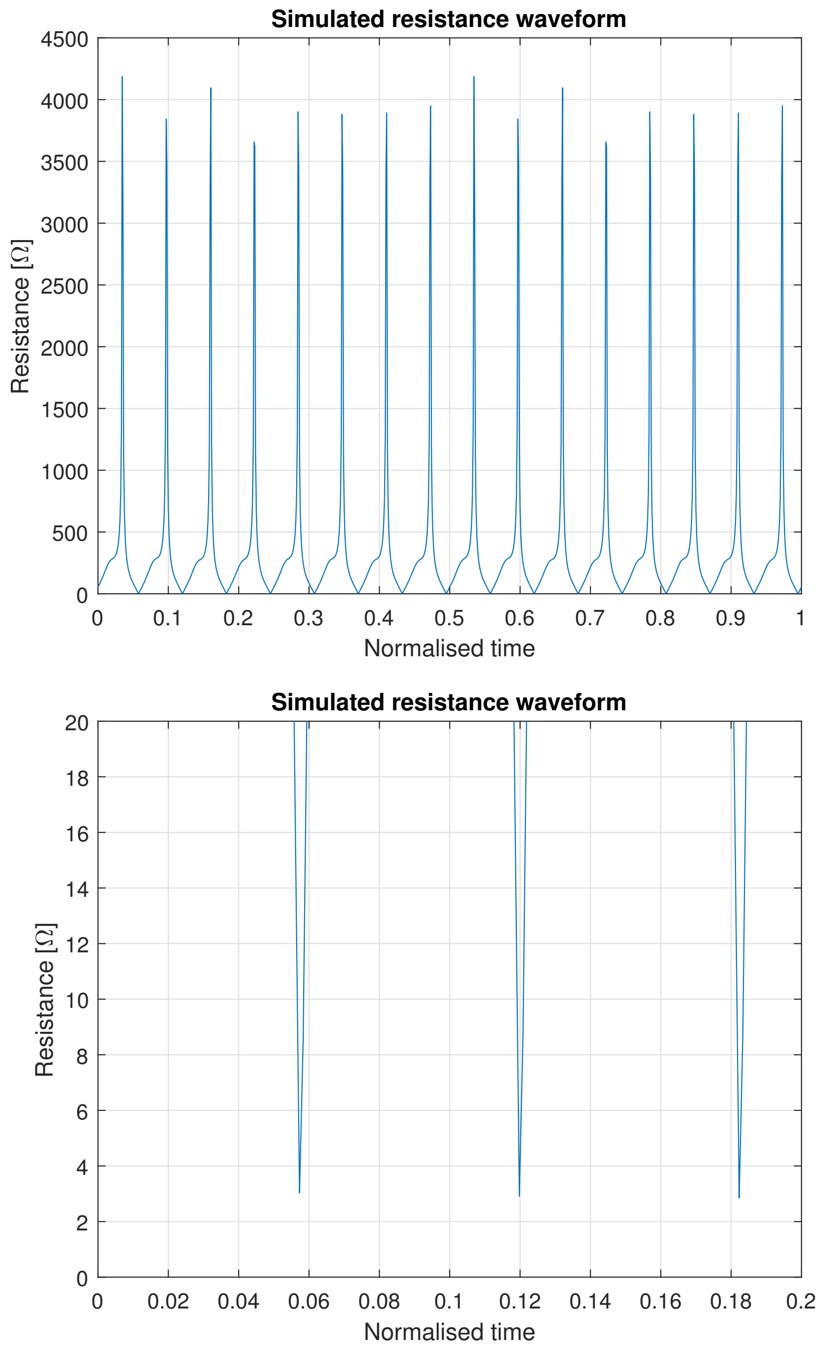

Figure 2.10: The simulated resistance waveform of the used diode. The bottom plot is a zoomed-in version of the upper plot.

2.2.2.1 Optimum mixer for a sinusoidal waveform

By using a more general form of the Z- and Y-mixer it is possible to obtain optimum mixers for specific waveforms [36]. If the waveform of the resistance in a Z-mixer is set to have a sinusoidal waveform described by,

$$r(t) = r_0 + 2r_1 \cos(\omega_{LO} t), \begin{cases} r_0 > 0 \\ |r_1| \leq r_0/2 \end{cases} \tag{2.26}$$

then the Z-mixer equation in (2.15) becomes [36]

$$\begin{bmatrix} V_{RF} \\ V_{IF} \end{bmatrix} = r_1 \begin{bmatrix} \frac{\sinh((l+2)\alpha)}{(\sinh(l+1)\alpha)} & 1 \\ 1 & \frac{\sinh((k+2)\alpha)}{(\sinh(k+1)\alpha)} \end{bmatrix} \begin{bmatrix} I_{RF} \\ I_{IF} \end{bmatrix} \tag{2.27}$$

where

$$\cosh\alpha = \frac{r_0}{2r_1} \tag{2.28}$$

and l and k are the number of short circuited frequency components at the input and at the output respectively. The optimum conversion loss is given by (2.17) where ϵ now becomes

$$\epsilon = \frac{\sinh((l+1)\alpha)\sinh((k+1)\alpha)}{\sinh((l+2)\alpha)\sinh((k+2)\alpha)}. \tag{2.29}$$

It can now be seen that the conversion loss decrease when l and k increase since $\epsilon \to \infty$ with l and k. This proves that for a sinusoidal resistance the optimum mixer is actually a Y-mixer, since the conversion loss goes to unity when the number of short circuited out-of-band frequencies goes to ∞. Saleh [36] provides the asymptotic optimum conversion loss with $R_{max} = r_0 + 2r_1$ and $R_{min} = r_0 - 2r_1$ for the sinusoidal resistance,

$$L_{opt,r\sim} \approx 17.4 \left(\frac{R_{min}}{R_{max}}\right)^{1/4} \quad \text{[dB]} \tag{2.30}$$

which can be compared to (2.24). If the conductance in the Y-mixer is set to be

$$g(t) = g_0 + 2g_1 \cos(\omega_{LO} t), \begin{cases} g_0 > 0 \\ |g_1| \leq g_0/2 \end{cases} \tag{2.31}$$

then the same optimum conversion loss is obtained but l and k becomes the number of open circuited out-of-band frequency components at the input and at the output respectively. This implies that the optimum mixer for a sinusoidal g is a Z-mixer. The conversion loss for the Y-mixer with a sinusoidal conductance is

$$L_{opt,g\sim} \approx 17.4 \left(\frac{G_{min}}{G_{max}}\right)^{1/4} \quad \text{[dB]} \tag{2.32}$$

where $G_{min} = g_0 - 2g_1$ and $G_{max} = g_0 + 2g_1$. Figure 2.11 shows the conversion loss for the Y-mixer and Z-mixer with a sinusoidal waveform together with the conversion loss for a Y- and Z-mixer with a square wave waveform. The curves reveals that the sinusoidal resistance or conductance will not be as good as when having a square wave waveform. Using (2.30) and the simulated values in Figure 2.10 gives $L_{opt} \approx 2.8\,\text{dB}$ which is a degradation by 1.2 dB compared to the 1.6 dB in (2.25).

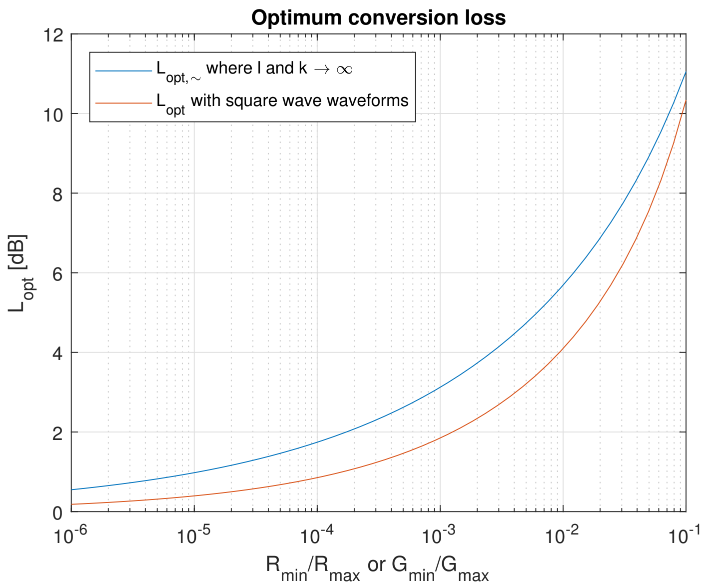

Figure 2.11: The optimum conversion loss for the sinusoidal waveform when l and k go to infinity and the conversion loss for the basic mixer with a square wave waveform.

2.2.2.2 The Y-mixer and Z-mixer with a diode

In this thesis the non-linear element is a Schottky diode. This particular device has specific voltage to current relation which is an exponential function as described in section 2.1. The equation for the Schottky diode is repeated here as it will be used in the following analysis,

$$i(v) = I_S(e^{\frac{qv}{\eta kT}} - 1) = I_S(e^{\beta v} - 1). \tag{2.33}$$

where

$$\beta = \frac{q}{\eta kT}. \tag{2.34}$$

By using (2.33) one can analyse the Y-mixer and Z-mixer with a diode. This is of interest since then the optimum mixer for the diode can be determined. The following analysis follows the work in [36] where Saleh presents a rigorous analysis of the Z-, Y-, H, and G-mixer with an exponential diode.

The two circuits that will be analysed is shown in Figure 2.12 where a diode has been placed in the Z-mixer and the Y-mixer. The input filter in the Z-mixer has a passband for the RF-signal and the LO-signal indicated by the frequencies ω_{RF} and ω_{LO}. All the out-of-band frequencies are terminated by an open-circuit provided by the filters as described before. The out-of-band frequencies in the Y-mixer are short-circuited by the filters which have stopbands at ω_{RF}, ω_{LO} and ω_{IF}. Saleh [36] includes DC bias in the analysis, this has been omitted in Figure 2.12 but will be included in the analysis. The LO power is assumed to be much larger than the RF signal and the IF signal, the currents and voltages can thereby be described by the LO frequency and its harmonics.

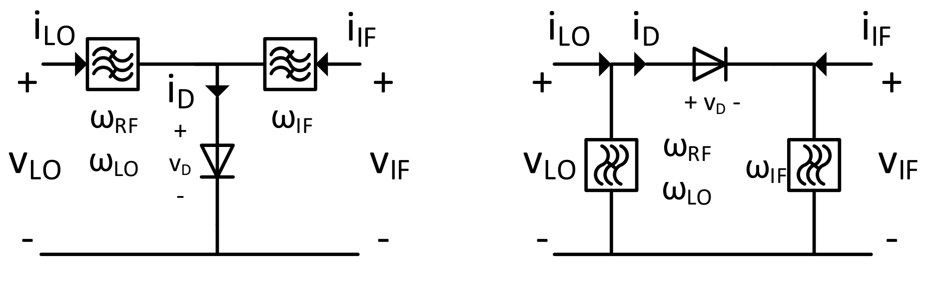

Figure 2.12: The Z-mixer (left) and Y-mixer (right) with a diode. DC biases are not shown in the circuits.

Starting with the Y-mixer, the diode current is given by

$$i_D = I_S(e^{\beta(V_{DC}+V_{LO}\cos(w_{LO}t))} - 1) \tag{2.35}$$

from which the small signal conductance can be found to be [36],

$$\begin{gathered} g(t) = \frac{di_D}{dv_D} = \beta I_S e^{(V_{DC}+V_{LO}\cos\omega_{LO}t)} = \\ y_0 + 2y_1\cos(\omega_{LO}t) + 2y_2\cos(2\omega_{LO}) + ... \end{gathered} \tag{2.36}$$

where

$$y_n = \beta I_S e^{(\beta V_{DC})} I_n(\beta V_{LO}) \quad , n \in [0, \infty). \tag{2.37}$$

I_n is the modified Bessel function of the first kind of order n. If the LO power is increased which implies that βV_{LO} is increased then, according to (2.36), $g(t)$ approaches a square wave which has been shown to be the optimum conductance waveform for a Y-mixer. Increasing the LO power will therefore improve the conversion loss such that it approaches the loss in Figure 2.9. One can also conclude that the ideality factor affects the mixer performance. Since $\beta \sim 1/\eta$ an increase of η decrease βV_{LO} which in turn degrades the waveform of g.

For the Z-mixer in Figure 2.12, the small signal conductance becomes [36]

$$g(t) = \frac{di_D}{dv_D} = \beta(i_D + I_S) \approx \beta i_D = \beta I_{DC}(1 + a\cos(\omega_{LO}t)) \tag{2.38}$$

where

$$a = \frac{I_{LO}}{I_{DC} + I_S}. \tag{2.39}$$

Equation (2.38) shows that the conductance is a sinusoidal. The Z-mixer is the optimum mixer for a sinusoidal conductance waveform as shown before, it is therefore expected that the Z-mixer is the optimum mixer when using a single diode. Another interesting property of the Z-mixer is that it seems to be less sensitive to variations in the ideality factor. Equation (2.38) shows that the conductance waveform will keep the same shape independent of η.

Saleh, [36], presents a comparison between the Y-, Z-, G- and H-mixer using a diode. In this investigation, which analyse the mixer conversion losses for the same bias and LO power, it was concluded that the Z-mixer is superior to the other mixers. This is expected since the conductance waveform turned out to be the optimum one in this case. Also, the Y-mixer was shown to be the worst mixer, which might be explained by the fact that it needs infinite power to obtain the square wave conductance waveform. These mixers therefore represent the best and worst mixer when using a single diode which is a result that can be used when designing mixers. Saleh discuss a disadvantage of the Z-mixer related to a restricted LO-power. However, according to Saleh, this does not apply for a mixer with low RF power which usually is the case in a receiver.

2.2.3 Subharmonically pumped antiparallel diodes

In high frequency applications the LO power requirement becomes harder to meet due to the fact that the available LO power decrease with higher LO frequency. A solution to this problem is to use subharmonically pumped mixers where half of the harmonic LO frequency is used. To do this one needs to implement a pair of antiparallel diodes, the circuit of such a pair of diodes is seen in Figure 2.13. If the ideal Schottky diode (2.33) is used for the purpose of the analysis the conductance of each diode is

$$g_1 = \frac{di_1}{dv} = \beta I_S e^{\beta v} \tag{2.40}$$

and

$$g_2 = \frac{di_2}{dv} = \beta I_S e^{-\beta v} \tag{2.41}$$

where $\beta = q/(\eta kT)$. Since the diodes are in parallel the total conductance is the sum of g_1 and g_2 given by

$$g = \beta I_S(e^{\beta v} + e^{-\beta v}) = 2\beta I_S \cosh \beta v. \tag{2.42}$$

If the RF signal is neglected such that the LO signal drives the diodes the conductance becomes

$$g = 2\beta I_S \cosh\left(\beta V_{LO} \cos \omega_{LO} t\right). \tag{2.43}$$

A comparison between the conductance of the antiparallel diodes and a single diode is shown in Figure 2.14. As seen, the waveform of the antiparallel diodes has a period half of the one produced by the single diode. This implies that the antiparallel diodes will act as a single diode but with twice as high switching frequency and thereby only half of the LO frequency is needed. If the RF signal is included the current becomes [38]

$$\begin{split} i =& A \cos \omega_{LO} t + B \cos \omega_{RF} t + C \cos 3\omega_{LO} t + D \cos 5\omega_{LO} t + E \cos\left(2\omega_{LO} + \omega_{RF}\right)t + \\ & F \cos\left(2\omega_{LO} - \omega_{RF}\right)t + G \cos\left(4\omega_{LO} + \omega_{RF}\right)t + H \cos\left(4\omega_{LO} - \omega_s\right)t + \ldots \end{split} \tag{2.44}$$

where $A, B, C\ldots$ are constants. It is concluded that the antiparallel diodes give only odd harmonics and intermodulation products which is illustrated in Figure 2.15 where m and n represents multiplies of the LO frequency and the RF respectively. The red case is the one used in subharmonic mixers and represent $2\omega_{LO} - \omega_{RF}$.

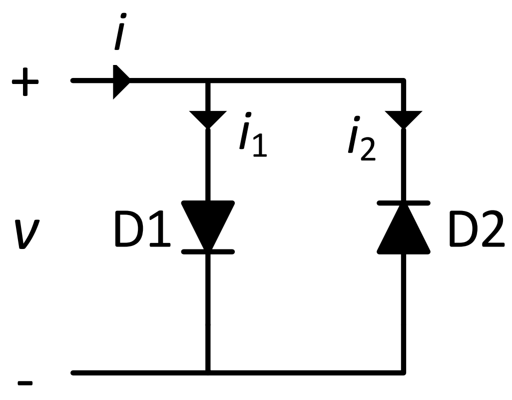

Figure 2.13: A pair of antiparallel diodes.

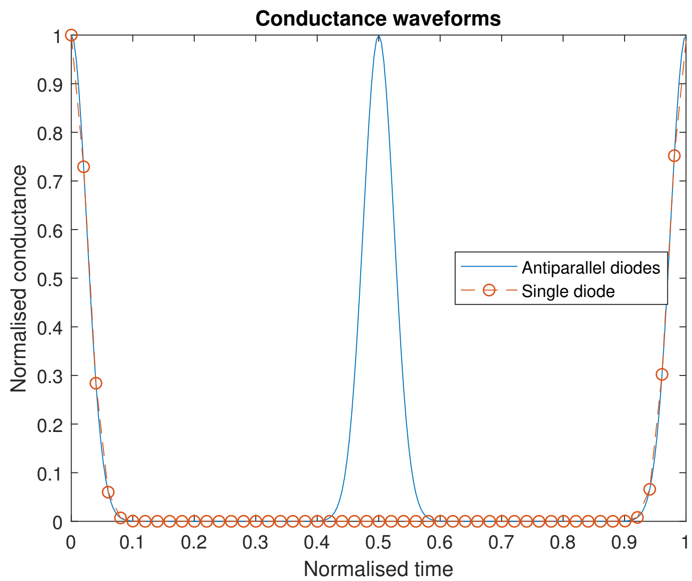

Figure 2.14: Conductance waveforms for a pair of antiparallel diodes and for a single diode.

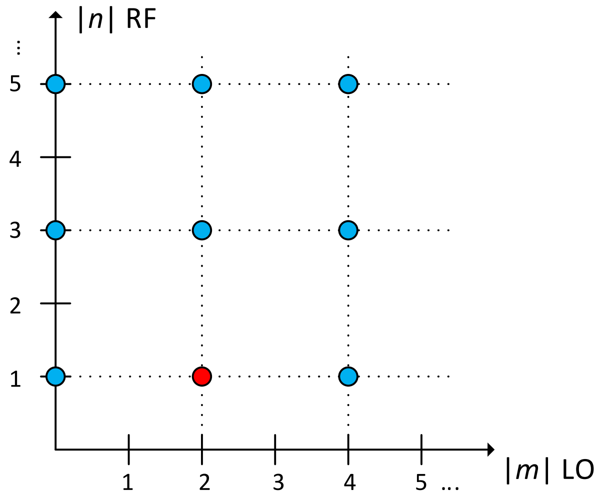

Figure 2.15: Frequency terms (in blue) of the total current of the antiparallel diodes. The red case is used in subharmonic mixers.

2.3 Microwave filters

In this section two types of filters are presented, the stepped impedance filter and the hammerhead filter. These filters are implemented in the mixer design as will be seen in chapter 3.

2.3.1 Stepped impedance filters

The stepped impedance filter is a simple filter which utilise a repeating structure with high and low impedance sections. These sections can easily be implemented in a microstrip circuit by alternating the width of the microstrip. The impedance of a microstrip is given by [30]

$$Z_0 = \begin{cases} \frac{60}{\sqrt{\epsilon_e}} \ln\left(\frac{8d}{W} + \frac{W}{4d}\right) & , \frac{W}{d} \leq 1 \\ \\ \frac{120\pi}{\sqrt{\epsilon_e}\left(W/d + 1.393 + 0.667\ln\left(W/d + 1.444\right)\right)} & , \frac{W}{d} \geq 1 \end{cases} \tag{2.45}$$

where d is the height of the substrate and W is the width of the conductor. ϵ_e is the effective dielectric constant given by

$$\epsilon_e = \frac{\epsilon_r + 1}{2} + \frac{\epsilon_r - 1}{2}\frac{1}{\sqrt{1 + 12d/W}} \tag{2.46}$$

with ϵ_r being the relative permittivity of the substrate. By plotting the impedance of the microstrip versus the conductor width for the two cases in (2.45) it can be seen how the impedance depend on the width, this has been done in Figure 2.16 for $\epsilon_r = 3.78$.

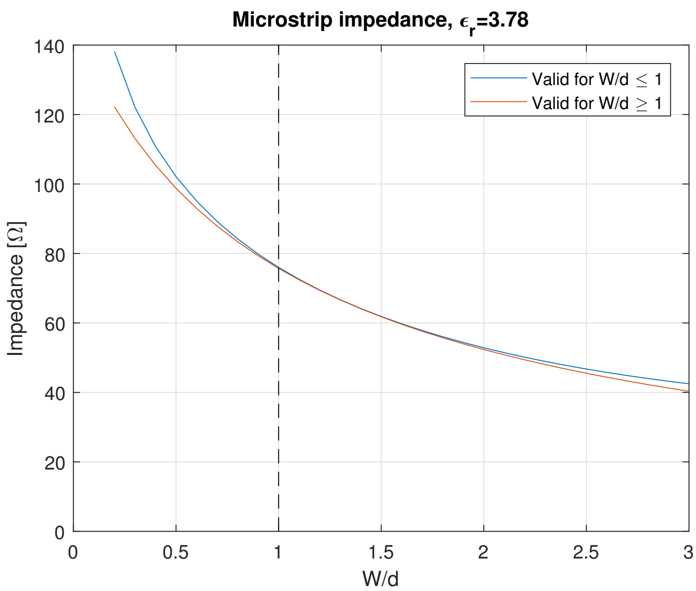

Figure 2.16: Theoretical microstrip impedance for a relative permittivity of 3.78.

The repeating low and high impedance sections act as an n-th order low-pass filter, where n is the number of sections. This is due to the fact that the high impedance sections are series inductances and the low impedance sections are capacitances in parallel [30]. The structure of a stepped impedance filter is seen in Figure 2.17 together with its equivalent circuit which is the circuit of a low pass filter. The filter in Figure 2.17 is of order $n = 5$ since it has 5 elements where $X/2$ is the reactance of the inductor and B is the reactance of the capacitor.

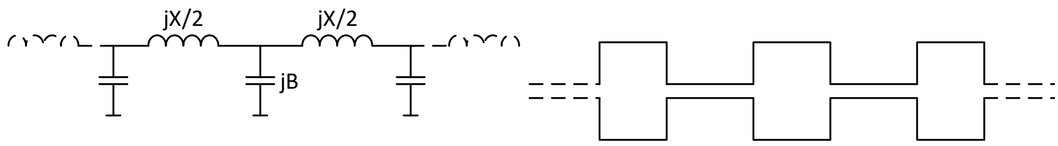

Figure 2.17: A low pass filter circuit and the corresponding stepped impedance structure.

If $\beta l < \pi/2$, where β is the propagation factor and l is the physical length, it can be shown that [30]

$$\frac{X}{2} = Z_0 \tan\left(\frac{\beta l}{2}\right) \tag{2.47}$$

$$B = \frac{1}{Z_0} \sin(\beta l) \tag{2.48}$$

which implies that a high impedance (narrow) section gives $X \approx Z_0 \beta l, B \approx 0$ and a low impedance (wide) section gives $X \approx 0, B \approx 1/Z_0 \beta l$ which correspond to a series inductor and a parallel capacitor respectively as stated earlier. To get the best possible filter suppression the ratio between the highest and lowest impedance should be as high as possible. The length of the different sections does not necessarily need to be equal, it depends on the type of low-pass filter (maximally flat or equal ripple) and the filter order [30].

2.3.2 Hammerhead filters

To achieve high filter suppression the filter order needs to be increased. Since the order of a stepped impedance filter is equal to the number of sections a higher suppression implies a longer filter and thereby more losses in the passband. In order to increase the suppression of a filter and at the same time keeping the filter short a hammerhead filter can be applied [10]. The name ”Hammerhead” origins from the structure which is seen in Figure 2.18. The heads on the sides of the transmission line provides additional inductances L_f and coupling capacitances C_f. The transmission line itself provides series inductances L_s and the main body of the filter provides a parallel capacitance C_s to ground. The fingers of the head creates capacitances, C_w, to the sidewalls which surrounds the circuit. From the circuit two resonances can be found [10], these are indicated by red boxes labelled as R1 and R2. By tuning these subcircuits individually the filter suppression can become high for a narrow frequency band if the resonance frequencies are placed close to each other. If placed further apart, the bandwidth will increase but the flatness of filter will be degraded. The coupling capacitances, C_w, are connected in parallel with C_s thereby increasing the total capacitance to ground which gives a better suppression.

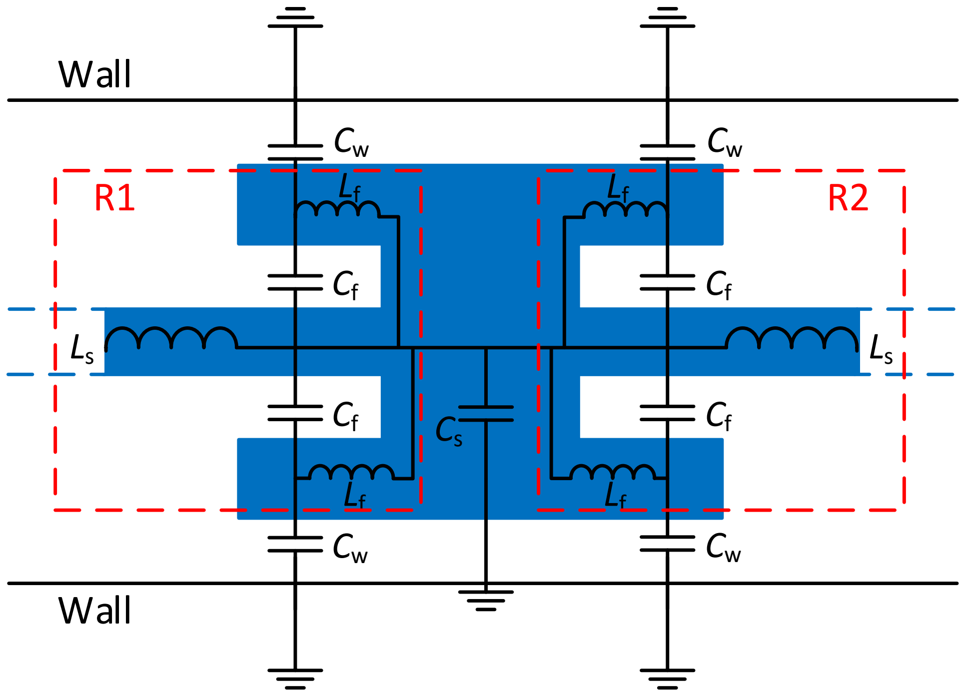

Figure 2.18: The structure (blue) and the equivalent circuit of a hammerhead filter. The red boxes indicates the two resonances, R1 and R2.

2.4 Literature study of Schottky diode mixers

Schottky diode mixers have been used for more than 30 years and have shown to give low conversion loss and low noise contribution in the terahertz region compared to mixers using transistors [9], [15], [22], [24], [39]. Before the 1990's whisker-contacted diodes were used as the nonlinear element in mixers [28], however these diodes were less reliable [15] and had problems with maintaining the same properties between different semiconductor wafers [28]. Due to the structure of the whisker-contacted diodes they were also nearly impossible to integrate with other circuits [22]. The planar Schottky diode [22] is a more reliable and rugged component [15] and is the commonly used diode today for submillimeter wavelength mixers.

Lehikoinen *et al.* [15] presented in 1996 a 119 GHz single ended harmonic mixer using a planar Schottky diode. It was used in the Odin satellite and showed a 7 dB SSB conversion loss and a noise temperature of 900 K (SSB) at room temperature. The mixer circuit was based on a microstrip layout, the substrate was made of quartz and the diode was mounted on top of the quartz substrate. Siegel, Dengler, Mehdi, Bishop and Crowe presented in 1992 a subharmonic mixer at 200 GHz using an antiparallel pair of planar Schottky diodes in a split-block structure. The IF bandwidth was low ($\sim 1\,\mathrm{GHz}$) and the minimum noise temperature was 1590 K (SSB) and the best conversion loss was 8.7 dB (SSB) with a LO power of 5.7 mW. In 1993, Ali-Ahmad, Bishop, Crowe and Rebeiz [17] presented a mixer design with a quasi-integrated horn antenna using a planar Schottky diode. It achieved a conversion loss of 7.2 dB (DSB) and a mixer noise temperature of 1310 K (DSB) at 250 GHz.

Today, at frequencies below 400 GHz, the designs use discrete antiparallel planar Schottky diodes mounted on quartz substrates, similar to the previous mentioned designs [39]. At frequencies above 400 GHz membrane Monolithic Integrated Circuits (MIC) is used due to a limited substrate thickness when using discrete Schottky diodes [40]. The most commonly used circuit topology when having discrete Schottky diodes is the suspended microstrip where the diode is flip-chip mounted at a position close to the RF waveguide to minimise the loss. Thomas, Maestrini and Beaudin [9] presented a subharmonic mixer design at 300 - 360 GHz with very good performance using this technology. The DSB mixer noise temperature was at minimum 700 K and the conversion loss was 6.3 dB at 330 GHz with 4 mW of LO power. Sobis [13] presented in 2011 a mixer design with a large IF bandwidth, it used a flip-chip mounted diode and a suspended microstrip. The simulated conversion loss was below 7 dB from 320 GHz to 370 GHz with an integrated LNA. The DSB receiver noise temperature varied from about 900 K to 1500 K for a IF from 3 GHz to 16 GHz.

Wang *et al.* [10] presented in the end of 2017 a mixer design where the problem with mechanically stressed substrates were addressed. They pointed out that the length to width ratio of previous designs is large (>20) and thereby the expanding aluminium becomes a problem when heating the circuit. This causes the substrates to bend and eventually break. To solve this problem Wang *et. al* replaced the more traditional stepped impedance filters with hammer-head filters, this reduced the length of the substrate. The mixer used a suspended microstrip with a silver epoxy glue at one end of the substrate to obtain a DC-ground. The measurements showed a very good performance, a minimum conversion loss of 5.5 dB (DSB) at 339 GHz, a minimum mixer noise temperature of 757 K and a 50 GHz 3 dB bandwidth were measured.

3

Mixer design

In this chapter the proposed circuit topology is presented. The mixer topology is described and the optimum diode circuit embedding impedance is determined. This is followed by a presentation of the mixer design.

3.1 Design methodology

The 183 GHz mixer was designed using a divide and conquer approach where the circuit was divided into subcircuits which were solved separately. When solved, the subcircuits are put together and tuned to give the correct response. Before beginning with the circuit design the optimum diode circuit embedding impedance must be found which will be the design goal for the whole circuit. An iterative process is adapted by performing the initial design in a circuit simulator (ADS [41]) with ideal transmission lines and then verifying it in a Finite Element Method (FEM) simulator (HFSS [42]).

To keep the design work simple, the stepped impedance technique described in section 2.3.1 was adopted. This will make it easier to get good correspondence between the circuit simulator and the FEM simulator than using hammer-head filters. The trade-off is a longer substrate but this can be tolerated since the proposed circuit topology, presented in section 3.5, is far less sensitive to mechanical stress.

3.2 Design requirement

The 183 GHz front-end, where the mixer is the first detection stage, should give a noise temperature below 1000 K which is the upper limit for the mixer noise. To minimise the noise contribution from the low noise amplifier connected to the mixer the conversion loss should be less than 7 dB. Other parameters are bandwidth and sideband balance which are presented in Table 3.1. The RF port interface should be a WR-5 (1.3 mm x 0.648 mm) rectangular waveguide and the LO port interface should be a WR-10 (2.54 mm x 1.27 mm) rectangular waveguide.

Table 3.1: Subharmonic mixer requirement

L_c (DSB)	T_{mixer} (DSB)	RF BW ($f_c = 183\,\mathrm{GHz}$)	LO BW ($f_c = 91.5\,\mathrm{GHz}$)	SBB
$\leq 7\,\mathrm{dB}$	$\leq 1000\,\mathrm{K}$	9 %	3 %	$\leq 1\,\mathrm{dB}$

The fabrication tolerances are specified in Table 3.2. It can be concluded that the substrate cavity and the quartz have the most critical tolerances.

Table 3.2: Fabrication tolerances for the mixer

Substrate cavity	Quartz substrate	Gold plating	Substrate position
$\pm 20\,\mu m$	$\pm 25\,\mu m$	$\pm 5\,\mu m$	$\pm 10\,\mu m$

3.3 Circuit technology

The circuit technology can be of different types. The hybrid circuit technology uses low loss substrates with gold plating which reduces the cost [13]. Discrete planar Schottky diodes are soldered onto the gold conductor, these diodes have a low noise and an enhanced robustness compared to whisker contacted Schottky diodes [22], [24], [39], [43]. The more advanced circuits are membrane Monolithic Integrated Circuits (MIC) which use components such as on-chip resistors, on-chip capacitors and integrated active components [13]. Microwave Monolithic Integrated Circuits (MMIC) or Terahertz Monolithic Integrated Circuits (TMIC) is a technology with an even higher level of integration, complete receivers can be designed on a single chip at frequencies above 100 GHz [44], [45]. These receivers have higher noise figures then those using planar Schottky diodes [9], [13], [44]–[46] at frequencies below 400 GHz.

The 183 GHz mixer in this thesis will use a commercially available technology [47] using quartz as a substrate with a thickness of 4 mil. It is a hybrid technology where the conductor (gold) can be plated on both sides of the quartz substrate and the conductor thickness is $5\,\mu$m which is much larger than the skin-depth at 183 GHz ($\sim 0.2\,\mu$m). An antiparallel Schottky diode, fabricated at Chalmers University of Technology, will be mounted onto the plated gold. The circuit technology offers a cost-effective production and a high accessibility which are two important aspects from a industrial perspective.

The RF and LO inputs of the mixer are rectangular waveguides which guide the incoming waves. E-field probes are used to couple the signals to the circuit consisting of the gold plated substrate and the diode. A cavity will provide the necessary space for the substrate which is glued to the mechanics. The mixer has a split-block configuration where the mechanical block is divided into a lower and upper block. This makes it possible to mill the waveguides and the substrate cavity.

3.4 Subharmonic mixer topologies

A subharmonic mixer can be configured in different ways. The antiparallel Schottky diodes can be connected in series or in parallel with the signal sources as described by [13]. The series and shunt connected topology can be seen in Figure 3.1. The series connected diodes requires a LO and IF short at the RF side and a RF short at the LO side. In the shunt connected case these conditions change to open circuits and the antiparallel diodes needs to be connected to a DC-ground [13]. The success of these topologies are dependent on the RF and LO short/open circuits that needs to be realised by the surrounding circuitry. Independent of topology the circuitry will not be able to achieve a perfect open or short circuit for the whole frequency band of interest and the performance will therefore be degraded.

The proposed topology for the 183 GHz mixer, seen in Figure 3.2, is based on the topology presented in [48]. It is a modification of the shunt connected diodes but here the antiparallel diodes are connected directly to ground and the RF and LO sources are placed at the same side of the diode. The DC-ground is obtained by suspending the diode between the mechanics and the end of the substrate as seen in Figure 3.3 where the beamlead antiparallel Schottky diode is seen. The parallel fingers and the beamleads are supported by the GaAs membrane. The diode is mounted on top of the substrate making it possible to do a visual inspection of the bonding surfaces and the diode itself. This is a great improvement from the flip-chip mounted diodes and the inverted substrates as in the suspended microstrip topology. By combining the RF and LO matching network the LO open circuit can be removed. To prevent the RF from leaking to the LO waveguide a RF filter is needed. This topology simplifies the shunt schematic by removing not only the LO open circuit but also the IF open circuit. Another feature is that the RF, LO and IF short circuits always will be well defined by the DC-ground, this is an improvement from the series schematic which is dependent on virtual grounds provided by filters and quarter wavelength transmission lines which have limited bandwidths. A combined LO and RF matching network with large bandwidth is the most challenging part in the proposed schematic and is likely to be the limiting factor.

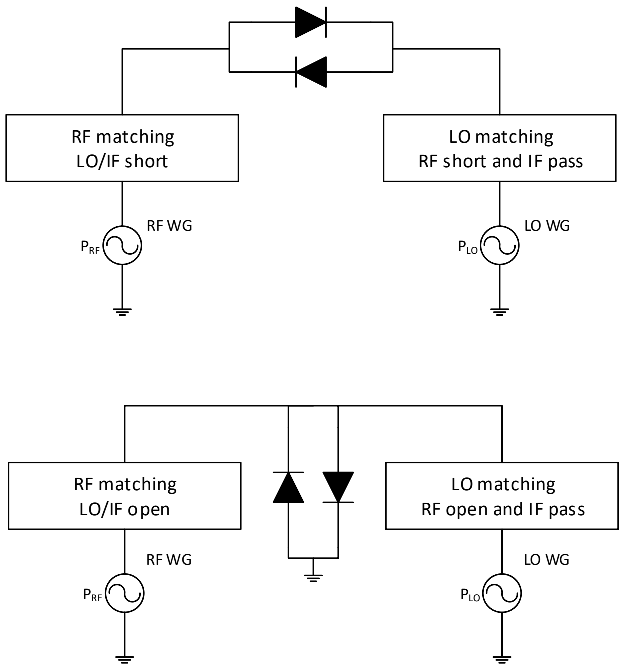

Figure 3.1: Schematic of a series (top) and shunt (bottom) connected antiparallel diode as described by [13]. The matching conditions are described as well.

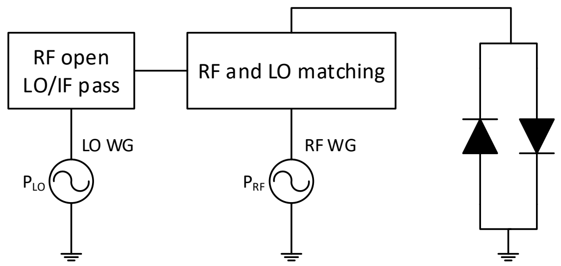

Figure 3.2: Schematic of the proposed topology which is a modification of the shunt connected topology.

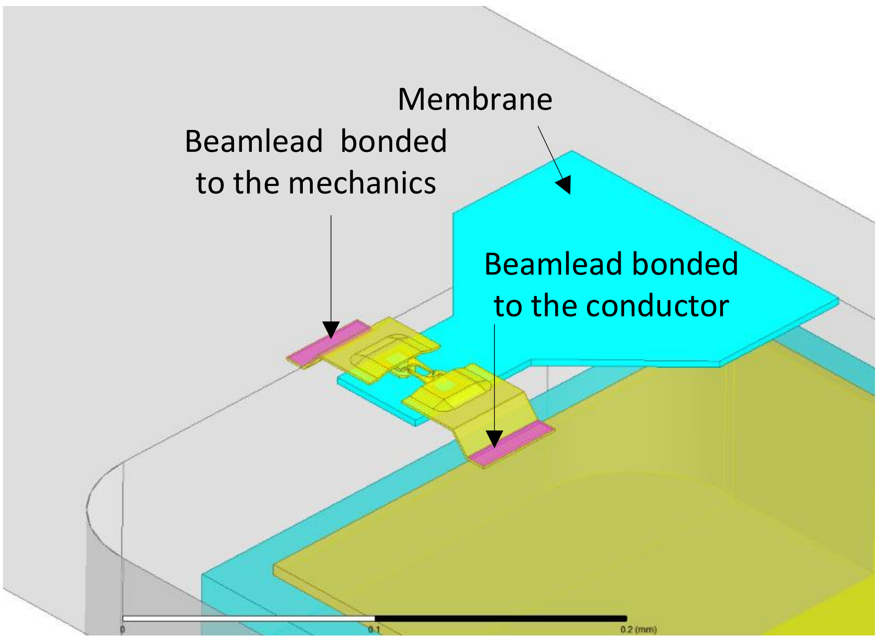

Figure 3.3: Illustration of the mounted diode. It is suspended between the mechanics and the end of the substrate. The proposed circuit topology allows for a visual inspection of the diode and bonding surfaces and the DC-ground is provided directly at the diode interface.

3.5 Circuit topologies

The position of the substrate and the shape of substrate cavity defines the circuit topology. A suspended microstrip topology where the substrate is surrounded completely by air is flip-chip mounted inside the cavity, such a topology is illustrated in the left picture of Figure 3.4. By placing a conducting glue between a mechanical platform and the plated gold at the end of the substrate a DC-ground can be obtained. In the other end of the substrate glue or ribbons can be used to keep the substrate fixed. The glue interface introduce mechanical stress to the structure when heating is applied during curing [10], [49]. Due to the difference in thermal expansion coefficients between aluminium and quartz the aluminium puts pressure on the quartz which is forced to either bend or break.

The microstrip topology has a substrate which is in contact with the cavity floor as seen in the right picture of Figure 3.4. The topology is not commonly used but has shown to give good mixer performance [15]. The circuit can be mounted by placing glue between the floor and the substrate at a few places along the substrate, this will however introduce an air gap since the glue has a certain thickness. The air gap is hard to control which will reduce the repeatability of the design. In order to obtain a DC-ground a bondwire to the mechanics is necessary.

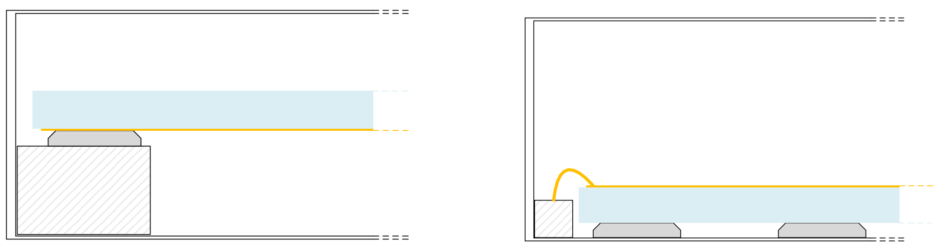

Figure 3.4: An illustration of two circuit topologies, the grey areas indicate the position of the glue. The left picture shows a suspended microstrip implementing the flipchip technique and the right picture shows a microstrip which is glued to the floor. A bondwire to the mechanics provides a DC-ground for the microstrip and a conducting glue provides a DC-ground for the suspended microstrip.

The proposed topology is a modification of the microstrip topology. By placing platforms along the cavity the substrate is raised from the floor, the glue can then be placed in the air gaps between the platforms as illustrated in Figure 3.5 which also shows the T-shaped cavity. When mounting the circuit the substrate is pushed down such that it is in contact with the platforms which will assure a correct and repeatable glue thickness, hence the uncertainty related to glue thickness is reduced. The mechanical stress can be considerably reduced by placing glue at one or possible two positions close to each other.

The proposed circuit topology is far less sensitive to mechanical stress which has been a major problem when assembling suspended microstrip mixers [10], however when placing the glue beneath the substrate a new uncertainty is introduced. If the glue expands and pushes the substrate upwards the impedance of the circuit will change thereby affecting the mixer performance. A simple experiment was conducted to investigate the thickness of the glue before an after curing. Quartz substrates were glued with a conducting glue, H20E [50], and a non-conducting glue, 2216 [51]. None of these glues expanded more than 10 µm.

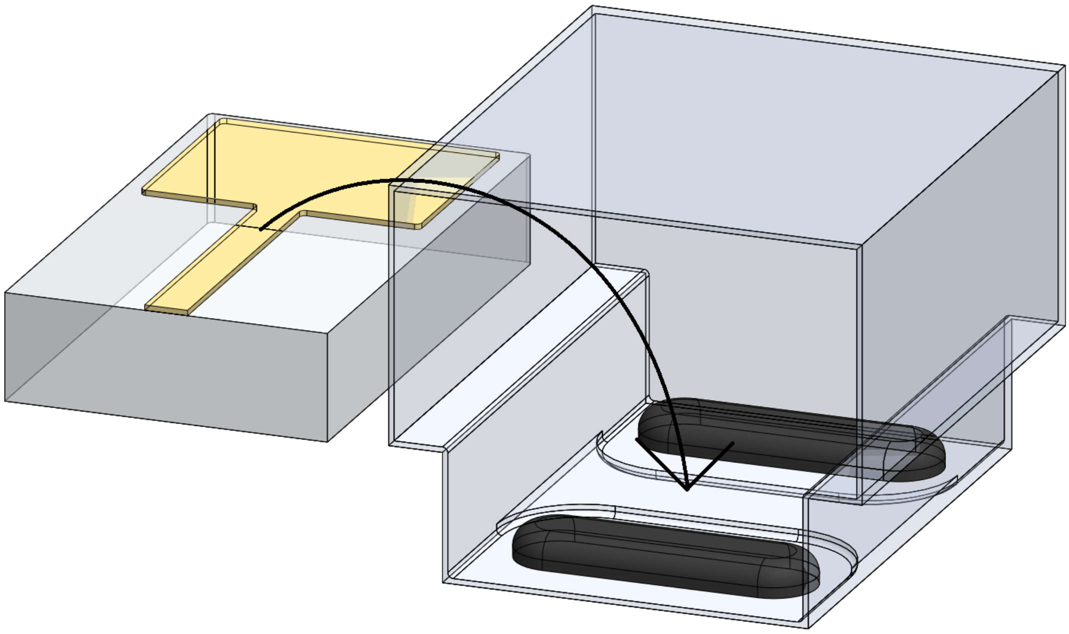

Figure 3.5: Proposed circuit topology where platforms are milled to raise the substrate from the floor. As indicated by the black bodies, glue can be placed between the platforms. The substrate cavity surrounds the substrate which is seen in grey.

3.6 Excited modes in the substrate cavity

As described in [30] a microstrip can excite a transverse resonance if the transmission line is wide enough, this can become troublesome if the substrate is too thick. Another issue is the possible excitation of a TE wave in the microstrip cavity which can be seen as a partially loaded rectangular waveguide [30]. If the width of the cavity becomes larger the cut-off frequency of this mode decreases. In this section the investigation of the higher order modes is presented. Based on this analysis the cavity dimensions and substrate width were set.

The geometry of the cavity is seen in Figure 3.6 where the split-plane is indicated in red. Since the substrate thickness and gold thickness is set (100 µm and 5 µm respectively) the height of the lower split-block channel (where the substrate is placed) is already defined. This is because the split-plane must be in the same plane as the conductor when bonding the diode beamlead to the mechanics. The upper part of the cavity was made wider than the lower part to make the design less sensitive to misalignment between the two blocks. Figure 3.7 shows a cross section of the cavity with the substrate placed in the lower channel.

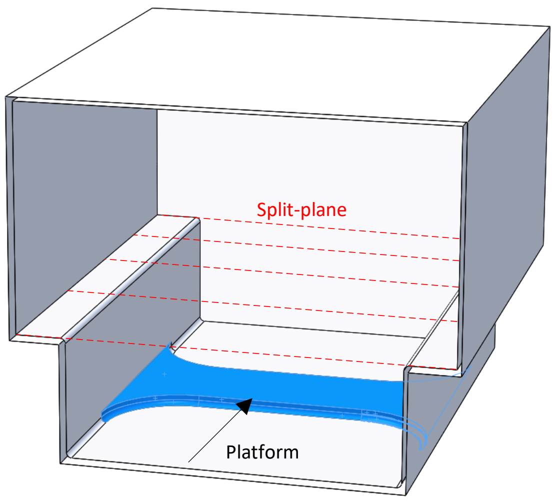

Figure 3.6: Split-block cavity with a substrate platform seen in blue. The split-plane is indicated in red which is the interface where the cavity is divided into top and bottom channel. The top and bottom part form a T-shaped cavity.

To increase the ratio between the maximum and minimum impedance the substrate was made as wide as possible. To find the cut-off frequencies of the higher order modes the width of the cavity was swept. The substrate followed the width of the lower cavity channel but was set to be 40 µm narrower. Two cases were investigated; a wide transmission line (40 µm narrower than the substrate) and a narrow transmission line (20 µm wide). Simulations showed that the transverse mode was the most critical one and this mode was excited for the case with a wide transmission line. The propagation factors for the different modes are shown in Figure 3.8 and the electric field distributions are found in Figure 3.9. The width of the upper cav-

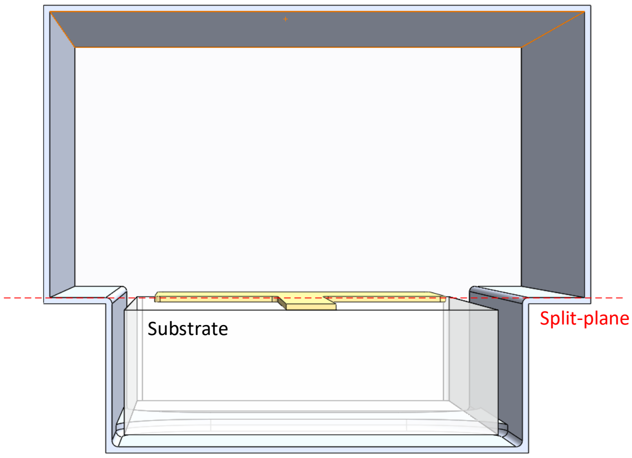

Figure 3.7: Cross section of the split-block cavity where the substrate also is seen.

ity channel starts at 400 µm and increases to 600 µm by steps of 20 µm. As seen in Figure 3.8, the fundamental propagation factor increases linearly with frequency as expected but depending on the cavity width the propagation at a certain frequency varies. Considering a manufacturing tolerance of ±20 µm an upper cavity width of 440 µm was considered to give a high enough second order cut-off frequency (220 GHz). The substrate width was set to 300 µm which is 40 µm narrower than the lower split-block channel. As seen in the bottom picture of Figure 3.8 the third order mode is excited at 220 GHz for a cavity width of 600 µm implying that this mode will not be critical. The cavity dimensions and the obtained upper and lower impedance limit are specified in Table 3.3.

As described before, the substrate will be placed on platforms that are distributed across the cavity. The platforms are positioned below the wide sections in order to reduce the impedance as much as possible. The height of the substrate platforms were set to 10 µm. This was considered to give enough space for the glue to expand during the curing process without raising the substrate. An additional airgap of 5 µm was added between the substrate and the platform to include mechanical manufacturing errors and an imperfect substrate placement.

Table 3.3: The dimensions and impedance limits at 183 GHz of the T-shaped cavity as a result of the mode excitation analysis. The platforms have a height of 10 µm above the floor.

Lower width	Upper width	Lower height	Upper height	Z_{low}	Z_{high}
340 µm	440 µm	120 µm	240 µm	53 Ω	140 Ω

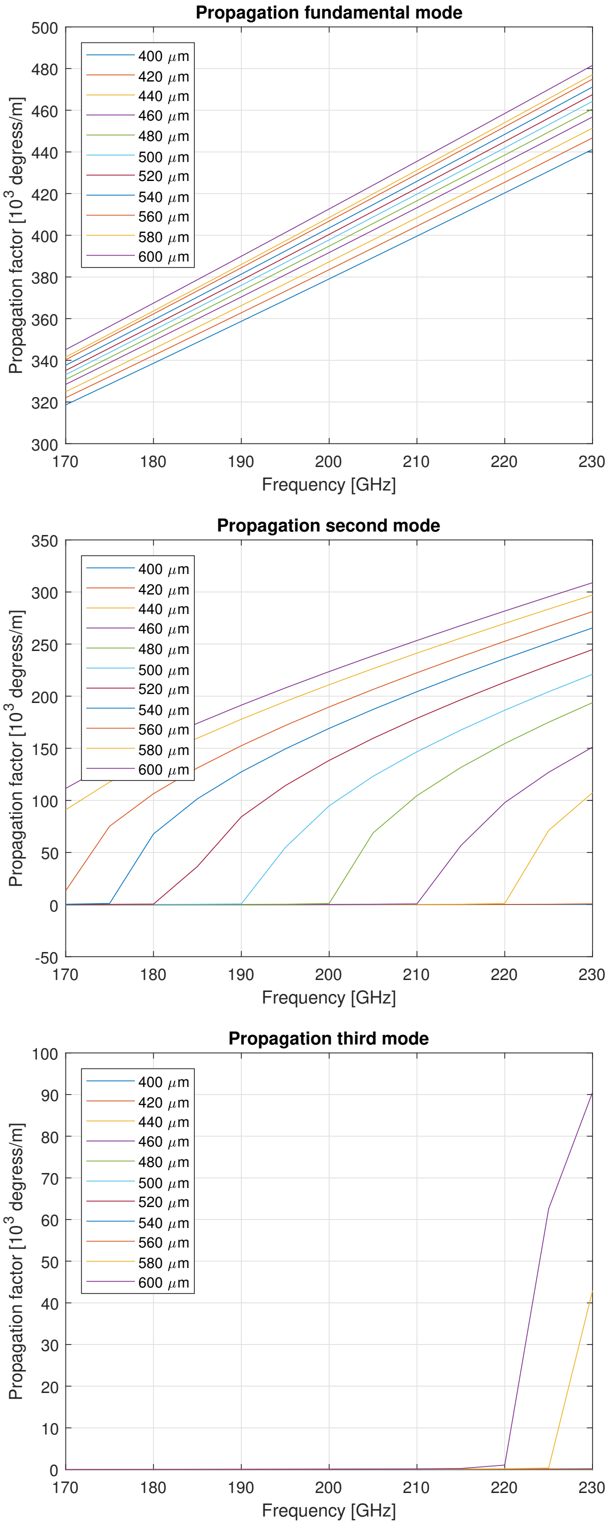

Figure 3.8: Propagation factor for the fundamental, second order (transverse) and third order (TE) mode. The parameter is the width of the upper cavity channel.

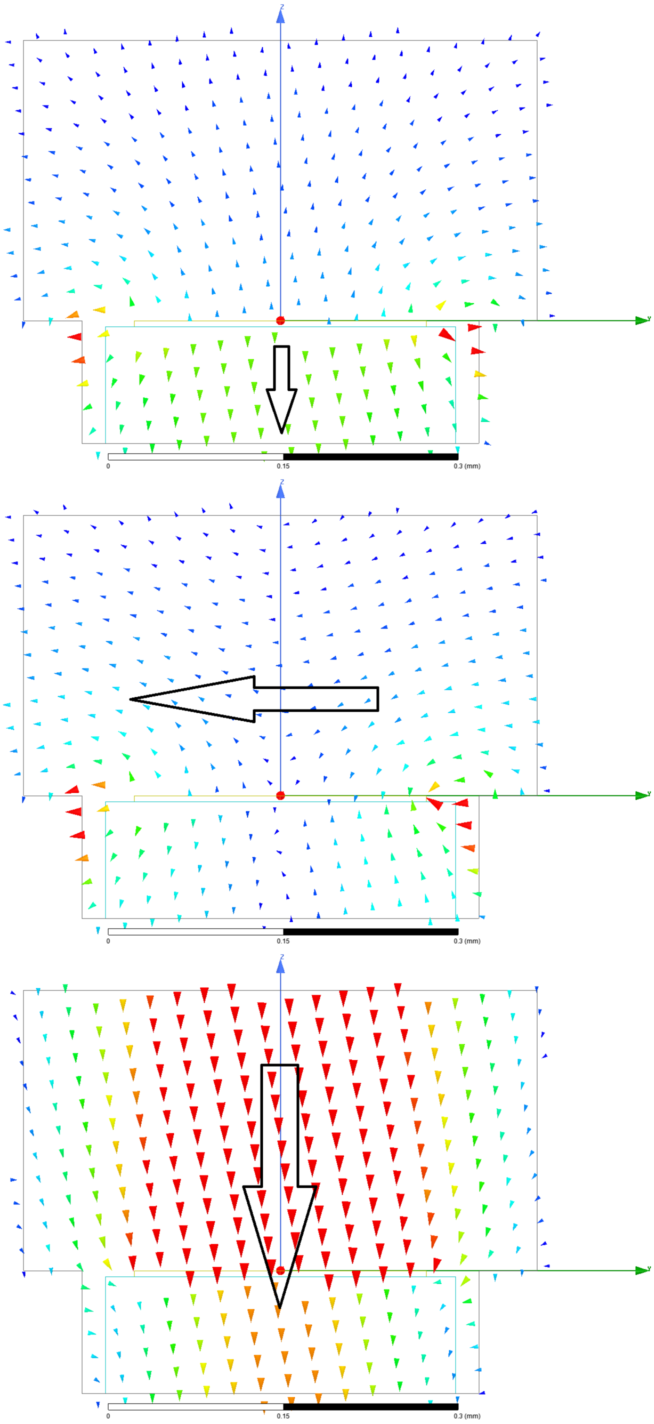

Figure 3.9: Electric field distribution of the fundamental (top), transverse/second order (middle) and TE/third order (bottom) mode.

3.7 Optimum diode circuit embedding impedance

A pumped diode has a diode impedance, Z_{diode}, which is the impedance seen into the diode. The conjugate of Z_{diode} is the optimum diode circuit embedding impedance, $Z_{opt,circuit}$, since it is the mixer circuit impedance seen by the diode giving the lowest conversion loss. The optimum diode circuit embedding impedance is frequency dependent and power dependent. In order to find $Z_{opt,circuit}$ two setups of a load pull simulation were used. The first setup swept the RF impedance seen by the diode and the LO impedance was set to a fix value. The second setup swept the LO impedance seen by the diode with a fix RF impedance. These simulations were performed in an iterative manner to find the optimum impedance for the RF and the LO frequency. The load pull simulations resulted in contours for different conversion losses in the Smith chart and the optimum impedance was found in the centre of the contours. The mixer was optimised for a diode anode area of 1.6 µm^2 having an ideality factor of $\eta = 1.3$, a junction capacitance of $C_j = 4.8\,\text{fF}$ and a series resistance of $R_s = 7\,\Omega$.

The ideal load-pull schematic is seen in Figure 3.10 where the antiparallel diodes are connected in series with the diode circuit embedding impedance, $Z_{circuit}$, which is seen by the diodes. By sweeping the resistance and the reactance of $Z_{circuit}$ the optimum impedance can be found. This was done for two frequencies, 91 GHz and 183 GHz. The multi-tone signal source provided the LO and the RF signal and the current, i, contained the fundamental frequency components but also the mixing products. Figure 3.11 shows the conversion loss contours for 183 GHz (blue) and 91 GHz (red). At a LO power of -3 dBm the obtained minimum conversion loss was 5.5 dB at 91 GHz and 4.9 dB at 183 GHz indicated by the triangles. When the LO power was increased to -1 dBm the position of $Z_{opt,circuit}$ shifted to the position of the stars.

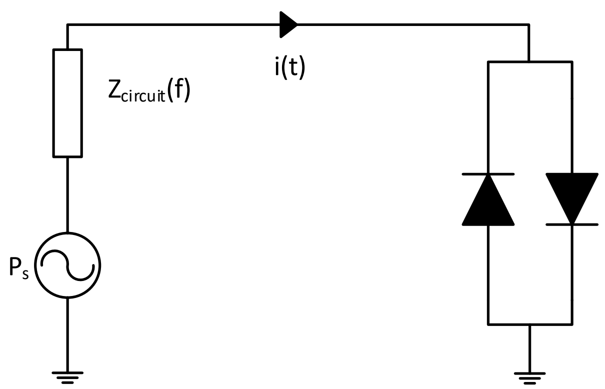

Figure 3.10: A load pull schematic with a pair of ideal antiparallel diodes. The diode circuit embedding impedance, $Z_{circuit}$, is swept in order to find the optimum diode circuit embedding impedance which gives the lowest conversion loss.

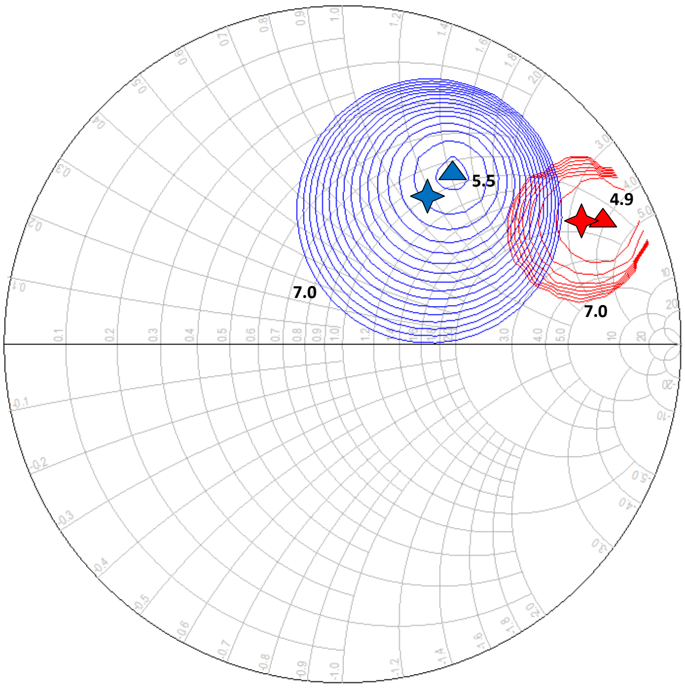

Figure 3.11: The conversion loss contours from the ideal load pull simulations. The blue contours correspond to a frequency of 183 GHz and the red contours correspond to a frequency of 91 GHz. A RF step of 0.1 dB has been used and the LO step is 0.3 dB. The triangles show the optimum diode circuit embedding impedances at a LO power of -3 dBm. At -1 dBm the optimum impedances drift towards the position of the stars.

3.7.1 S-parameter simulation setup

When performing S-parameter simulations to investigate the diode circuit embedding impedance, the Schottky junctions are replaced with lumped ports, this is described by Figure 3.12. One of the lumped ports is terminated with an open circuit (o.c.), this represents the diode which is non-conducting (the diodes do not conduct at the same time) and the other port is terminated with 50 Ω. To investigate the return loss at the RF port (WR-5 waveguide interface) and the LO port (WR-10 waveguide interface) the lumped ports are terminated with an open circuit and the diode impedance, Z_{diode}, as illustrated in Figure 3.13. This is also the case when investigating insertion losses between different ports. This simulation setup makes it possible to verify the harmonic balance simulations which result in return losses at the RF and LO port.

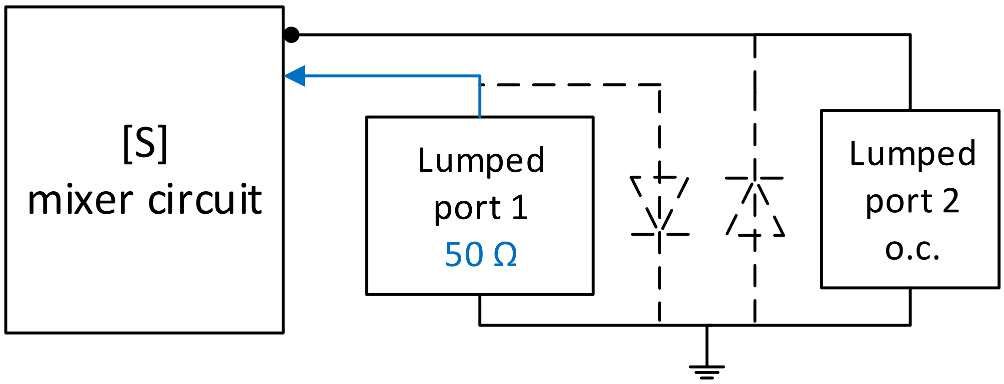

Figure 3.12: Illustration of the termination of the diode lumped ports when investigating the diode circuit embedding impedance. The ports replace the Schottky junctions (dashed) and are connected to the mixer circuit which include the diode structure. The used lumped port (blue arrow) is terminated with 50 Ω and the opposite lumped port is terminated with an open circuit.

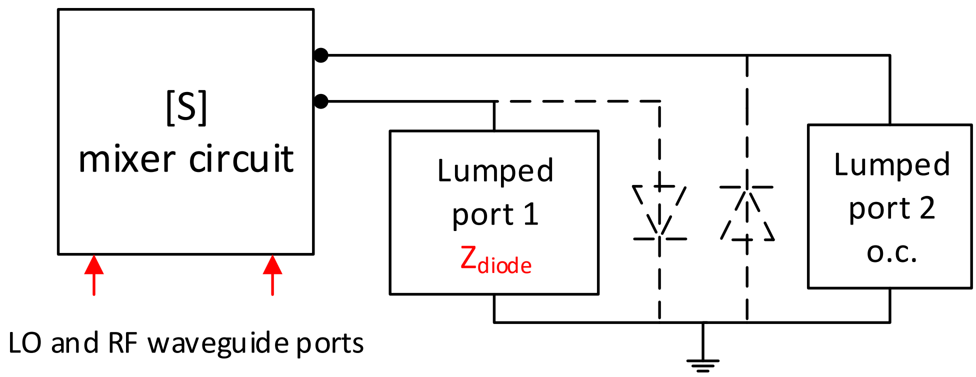

Figure 3.13: Illustration of the termination of the diode lumped ports when investigating return losses at the RF and LO port as well as when investigating insertion losses between different ports. One lumped port is terminated with the diode impedance Z_{diode} and the opposite lumped port is terminated with an open circuit.

3.8 LO and RF matching network

As described in section 3.4 the LO and RF matching is integrated into a common network. This network includes the RF waveguide with backshort and the RF E-probe that couples the incoming wave to the diode. The probe is positioned in the centre of the E-plane of the rectangular waveguide to achieve the best possible coupling. To obtain a broadband frequency response the height of the waveguide is reduced in the vicinity of the probe and the probe is made as wide as possible as described by [9]. The RF waveguide, having the dimensions according to the WR-5 standard, is connected to the waveguide with reduced height. This introduce a stepped impedance interface which is also part of the matching network.

As a first step the probe and the reduced waveguide was designed, this initial 3D-model is seen in Figure 3.14 where the arrow represents the deembedding distance done at the microstrip ports. The 4-port model, consisting of two waveguide ports and two microstrip ports, was tuned in ADS by importing the 3D-model S-parameters. One of the waveguide ports was short circuited to represent a backshort and the other waveguide port was terminated with the WR-5 impedance. The two microstrip ports are labelled as ”Schottky diode port” (SD port) and ”filter port” to distinguish between the two sides of the probe. The response of the probe was analysed at the SD port and the filter port was terminated with a close to open circuit to represent the future RF filter. Two different waveguides were analysed, one with a reduced height of 400 µm and one with a strongly reduced height of 300 µm.

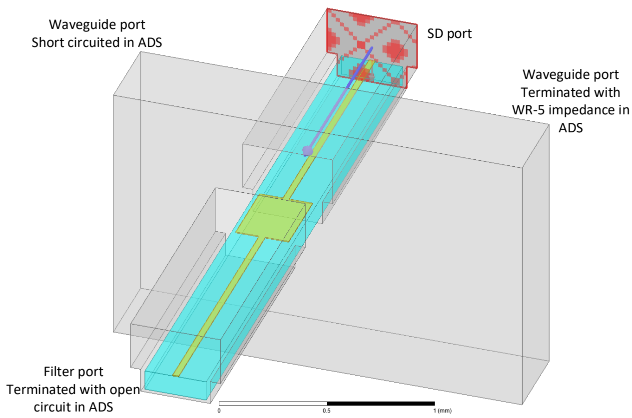

Figure 3.14: Model of the waveguide with reduced height and the E-probe positioned in the centre of the E-plane. The arrow indicates the deembedding distance at the microstrip ports.

The impedance at the SD port for the model having a waveguide height of 400 µm is seen in the top Smith chart of Figure 3.15. As seen the RF impedance (blue) is well confined and close to the optimum impedance seen in purple. However the LO impedance (red) is far from the optimum position. The bottom Smith chart shows the response of the model having a strongly reduced waveguide. The LO impedance has been improved, at 91 GHz it is now close to the optimum impedance but it is not well confined. This is not necessary a problem since the LO bandwidth is small.

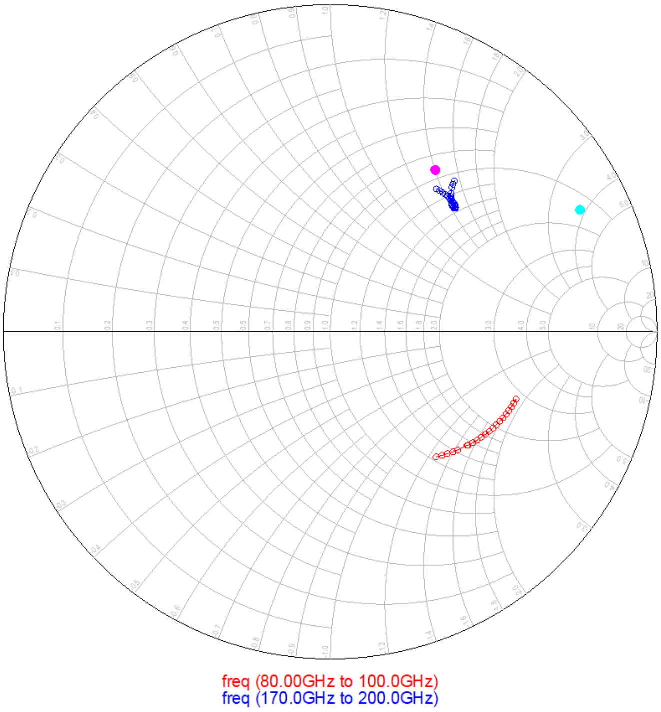

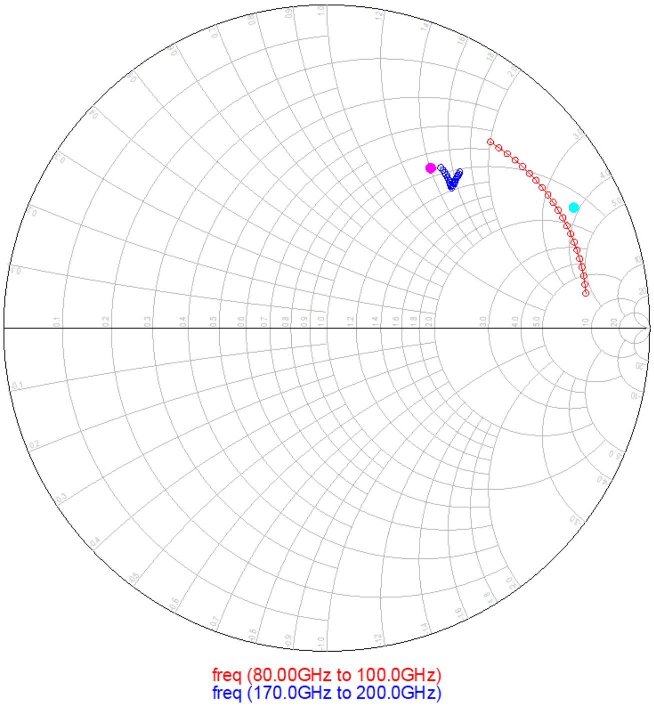

Figure 3.15: Response obtained in ADS of the final optimised RF probe. The top Smith chart correspond to a waveguide with a height of 400 µm and the bottom chart correspond to a height of 300 µm. The purple dot and the blue dot is the optimum diode circuit embedding impedance for the RF and the LO frequency respectively.

Since the RF probe with a strongly reduced waveguide gave a good match for both the LO frequency and the RF it was decided to continue with this model. The next step was to implement the circuit design as a 3D model where the backshort, stepped impedance interface and the Schottky diode are included, this model is seen in the top picture of Figure 3.16. The SD port has been replaced with two lumped ports located at the Schottky junctions. By looking into one of these ports, with the other port open circuited, the response of the complete matching network can be analysed. As shown before the diode is suspended between the substrate and the mechanics to provide the DC-ground. So far the backshort is modelled using 90° corners, this is not possible to manufacture. The edges need to be adapted to the tool that will mill the split-block but this will be done at a later stage to make it possible to tune the backshort during the design work.

The response of the optimised 3D-model is seen in the Smith chart in the bottom part of Figure 3.16, both the RF and LO impedance correspond well to the impedances obtained in ADS. The RF impedance has become a bit less confined but it encircles the optimum impedance in a favourable way. The contours from the ideal load-pull simulation are also shown. It can be seen that the RF impedance stays within the 5.6 dB contour and that the LO match has a bandwidth of 6 GHz centred at 91 GHz (within the 5.6 dB contour).

Another way to characterise the performance of the matching network is to look at the return loss at the RF port (the waveguide interface) and the insertion loss between the RF port and the diode. When performing this S-parameter simulation the RF port is terminated with the WR-5 impedance and one of the diode lumped ports is terminated with the diode impedance at RF. The other lumped port is open circuited as described in section 3.7.1. The same simulation can be done for the LO frequencies. Figure 3.17 shows the return losses and insertion losses for a frequency band of 80 GHz to 100 GHz and 170 GHz to 200 GHz. It is seen that the RF port return loss is better than 14 dB and that the insertion loss is better than 0.5 dB. The LO port return loss is centred at 90.5 GHz but has a lower bandwidth. However the required LO bandwidth is low, the centre frequency is of more importance.

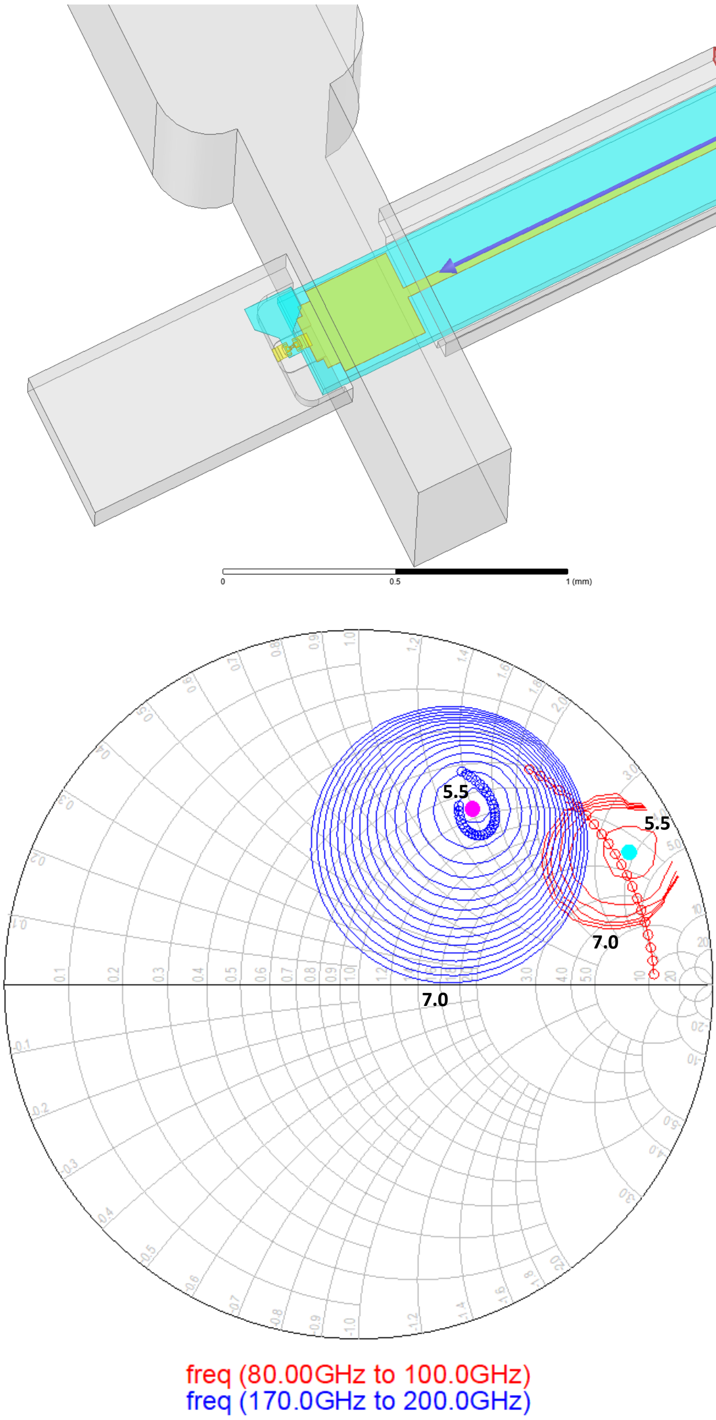

Figure 3.16: 3D-electromagnetic model of the combined LO and RF matching network where a fix backshort with 90° corners is used together with a stepped impedance section in the waveguide. The Smith chart shows the obtained diode circuit embedding impedances at the RF and the LO frequencies, the dots indicate the optimum impedances at 183 GHz (purple) and at 91 GHz (light blue). The blue contours applies for 183 GHz and has a step of 0.1 dB, the red contours applies for 91 GHz and has a step of 0.3 dB.

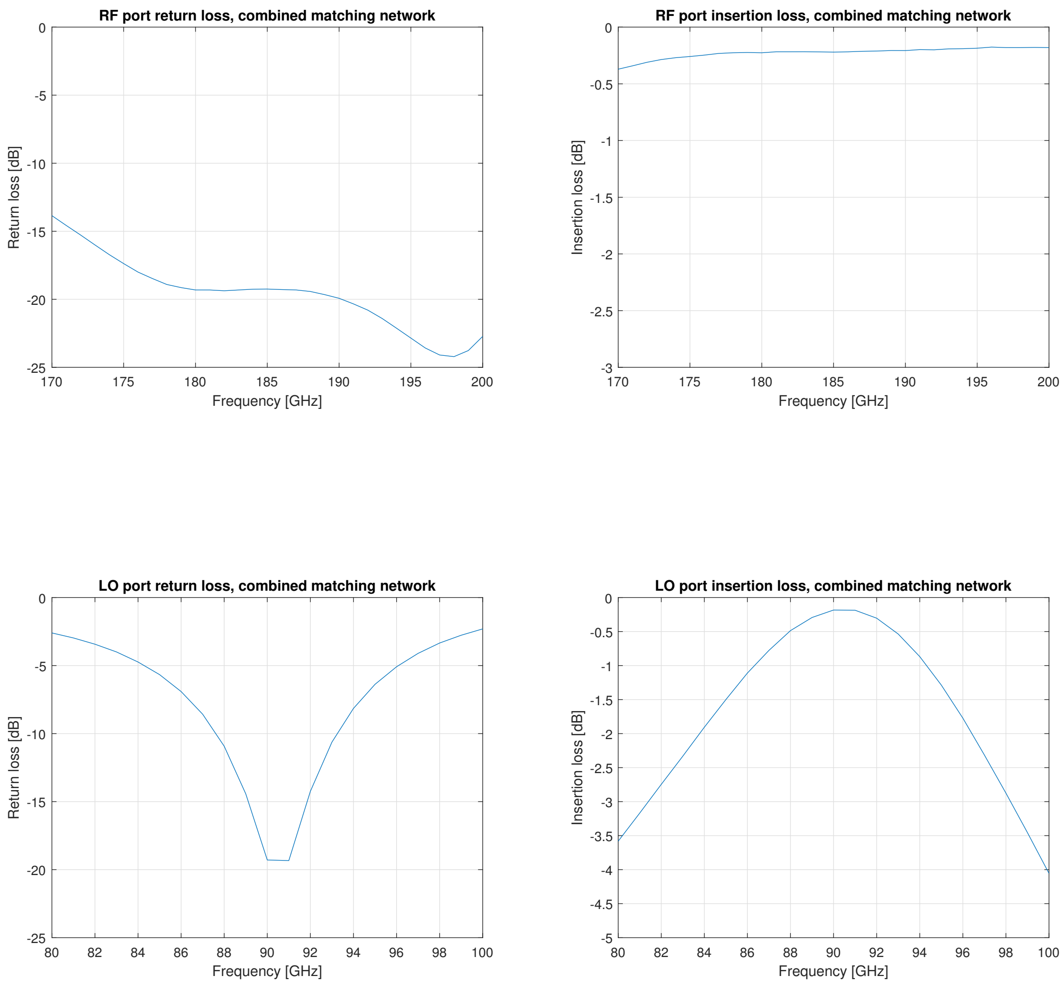

Figure 3.17: Return losses and insertion losses for the combined matching network obtained with a S-parameter simulation where the RF port is terminated with the WR-5 impedance and the diode lumped ports are terminated with Z_{diode} and an o.c. The LO port was terminated with a preliminary LO probe reflection of $\Gamma = 0.6\underline{/69°}$
.

3.9 RF filter

When designing the combined LO and RF matching network the termination at the filter port was assumed to be an open circuit for the RF. This assumption was based on the mixer topology schematic where a RF choke filter is connected to the matching network. The design goal of the RF filter is therefore to get a reflection coefficient given by $\Gamma \approx 1\underline{/0^\circ}$. A stepped impedance filter was chosen due to the simple structure which makes it easier to implement in a circuit simulator.

By tuning the filter in ADS and then implementing the design in HFSS the model seen in Figure 3.18 was obtained, the filter is of order 5 since it contains three narrow sections acting as inductances and two wide sections acting as capacitors. Beneath the substrate, seen in light blue, are the substrate platforms located. These are placed underneath the low impedance sections in order to lower the impedance as described in section 3.6.

As described by the mixer topology, a LO probe will be connected to the RF filter. The RF response of the LO probe is however hard to predict since the LO waveguide is a cavity with multiple modes at RF. To predict the filter performance when connecting it to the LO probe the port termination was varied. Figure 3.19 shows the suppression and the reflection coefficient for a RF filter termination of 50 Ω, 100 Ω and 150 Ω. The flatness and RF suppression was below 1 dB and between -19 dB and -14 dB respectively indicating that the RF filter is not very sensitive to different loadings at the LO side. Simulations shows that the reflection coefficient at RF remains almost constant for all terminations, the phase is however shifted from the desired open circuit condition but this can be tuned by increasing the length of the transmission line. It should also be mentioned that the filter and the matching network were tuned in parallel as two separate networks. This to obtain a similar response as in Figure 3.16 when the filter is connected to the matching network.

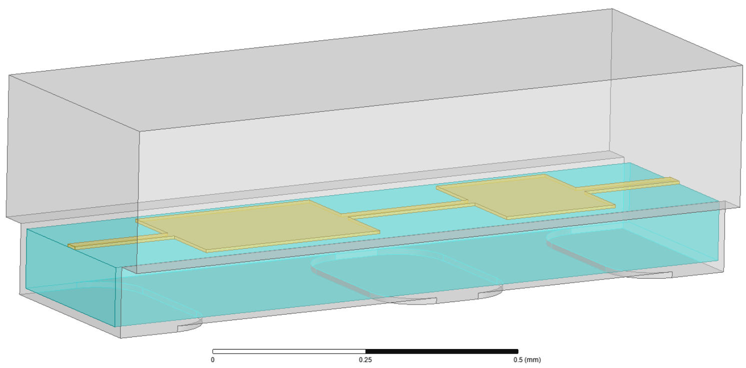

Figure 3.18: RF choke filter implemented as a stepped impedance filter of order 5. Notice the platforms on which the substrate rests.

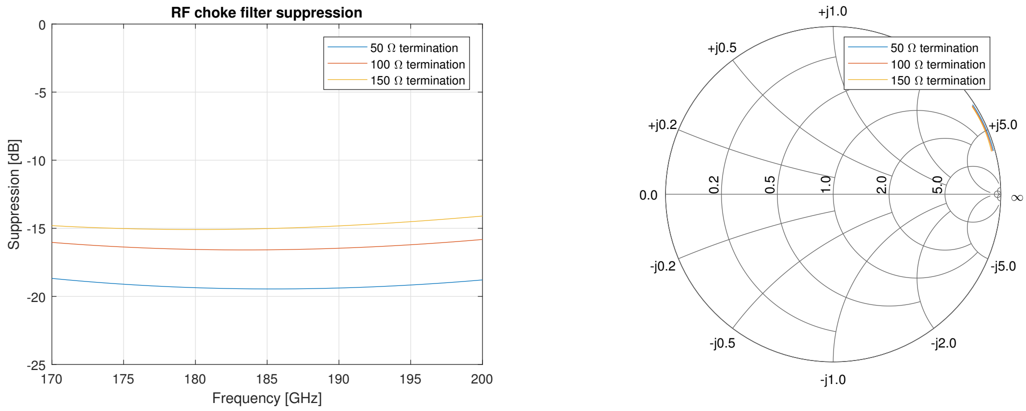

Figure 3.19: RF filter performance in terms of suppression and S_{11} presented in the Smith chart. The different curves correspond to different filter terminations.

3.9.1 Filter and matching network verification

To verify the filter and the LO/RF matching network a full 3D-model was implemented. The filter position was tuned such that the correct phase was obtained at the interface between the two circuits. The final model is seen in Figure 3.20 where the blue arrow represents the deembedding distance at the LO port to which the LO probe will be connected. The return loss at the RF port and the LO port are seen in Figure 3.21. Two cases are presented, the circuit simulator (ADS) design and the 3D model (HFSS). As seen the correspondence between the circuit simulator, using ideal transmission lines, and the full 3D-model is good. Figure 3.22 shows the filter suppression which is better than the suppression shown in Figure 3.19. This is due to an additional low-high impedance transition between the RF probe and the RF filter.

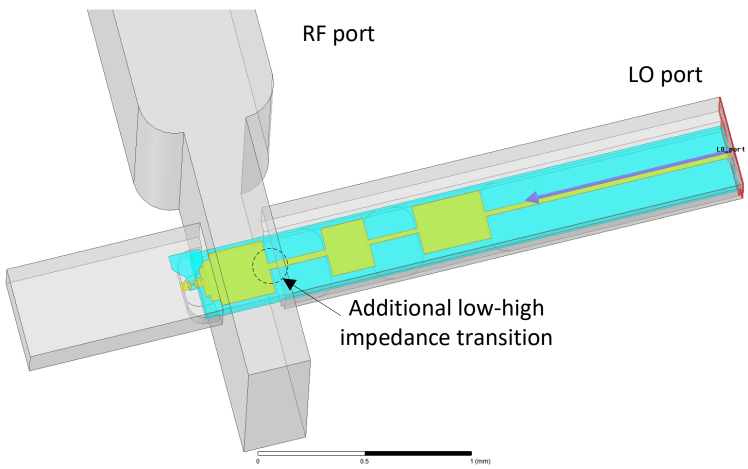

Figure 3.20: 3D-electromagnetic model of the matching network connected to the RF filter. The blue arrow represent the deembedding distance.

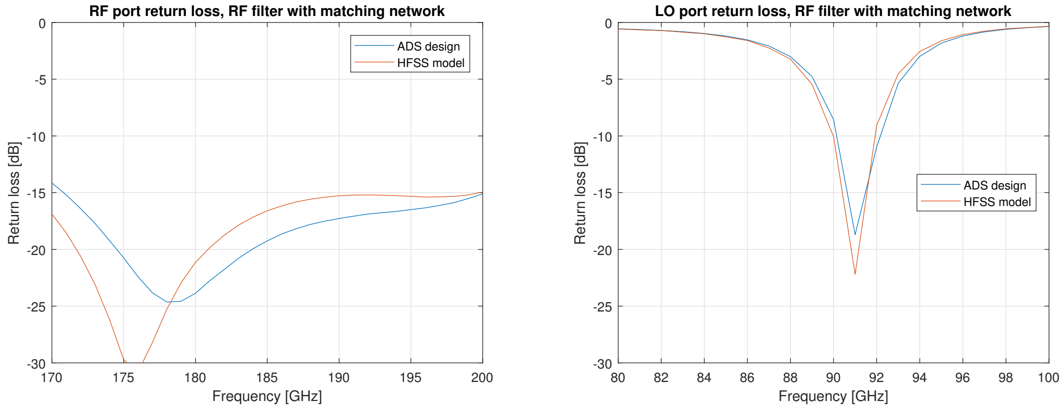

Figure 3.21: Return losses at the RF port (terminated with the WR-5 impedance) and the LO port (terminated with a preliminary LO probe impedance of $\Gamma = 0.6\underline{/69°}$) for the ADS design where the filter and matching network were tuned and the HFSS design where a full 3D-electromagnetic model was used. The diode lumped ports was terminated with Z_{diode} and an o.c.

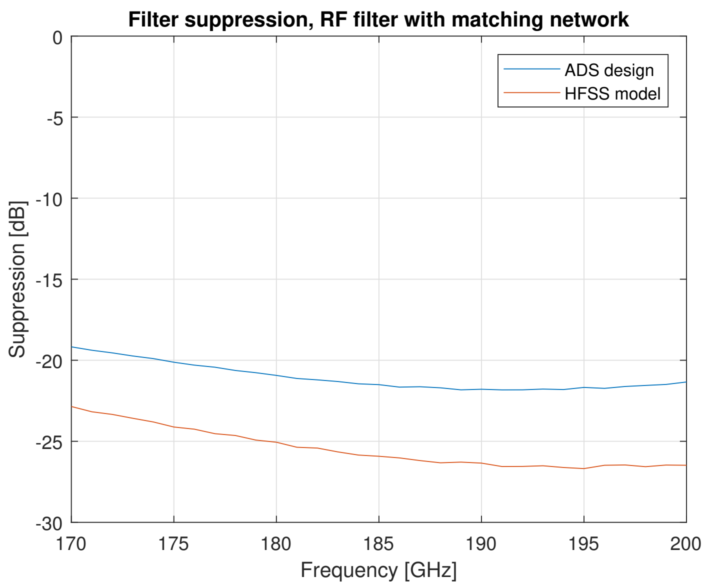

Figure 3.22: RF suppression between the RF port (terminated with the WR-5 impedance) and the LO port (terminated with a preliminary LO probe impedance of $\Gamma = 0.6\underline{/69°}$). The diode lumped ports was terminated with Z_{diode} and an o.c.

3.10 Initial mixer simulation

Up till now only linear simulations have been performed (S-parameter simulations) but in order to analyse the mixer performance a non-linear simulation is required. A harmonic balance simulation, using the model in Figure 3.20, was performed to verify the circuit design. The microstrip conductor loss was included in the simulation. The conversion loss and return loss at the RF port is seen in Figure 3.23 and Figure 3.24 respectively. As the conversion loss plot shows the design is centred at a LO frequency of 91.5 GHz as desired and at this frequency the conversion loss is below 6 dB for the whole RF band indicated by the dashed lines. The conversion loss has a minimum of 5.4 dB at 183.1 GHz indicating a close to ideal impedance match. The reason for the narrow LO bandwidth, seen in the conversion loss plot, is due to the port termination at the LO port which was set to a single point impedance for the whole LO band. By performing a S-parameter simulation the Smith chart in Figure 3.25 was obtained.

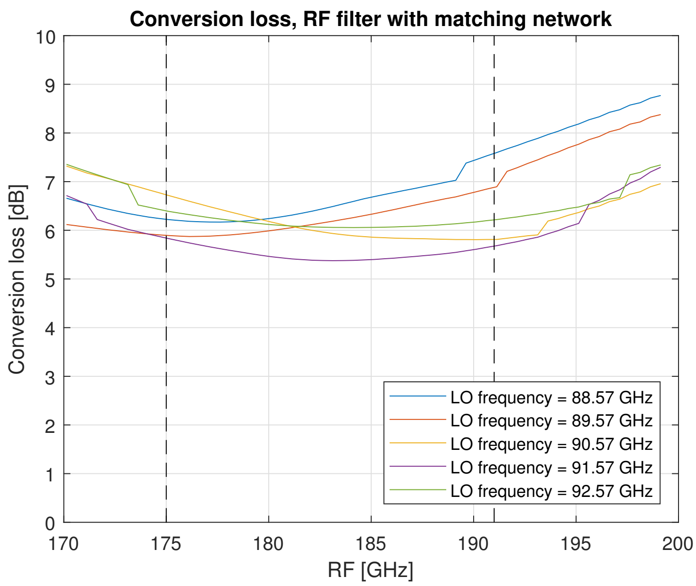

Figure 3.23: Conversion loss obtained with the matching network and the RF choke filter. The minimum conversion loss is 5.4 dB and the LO power is 1.5 dBm. Only the microstrip conductor loss was included.

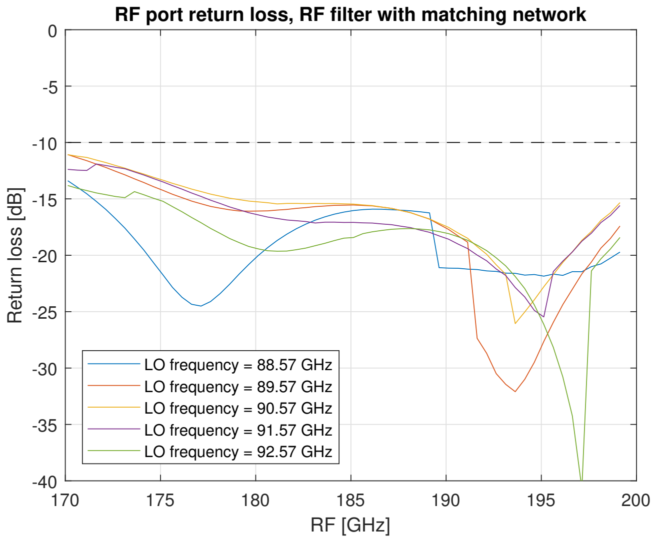

Figure 3.24: Return loss at the RF port obtained with a harmonic balance simulation using a LO power of 1.5 dBm. The 3D-electromagnetic model includes the matching network and the RF choke filter. The loss is less than -10 dB for all LO frequencies indicating a good impedance match.

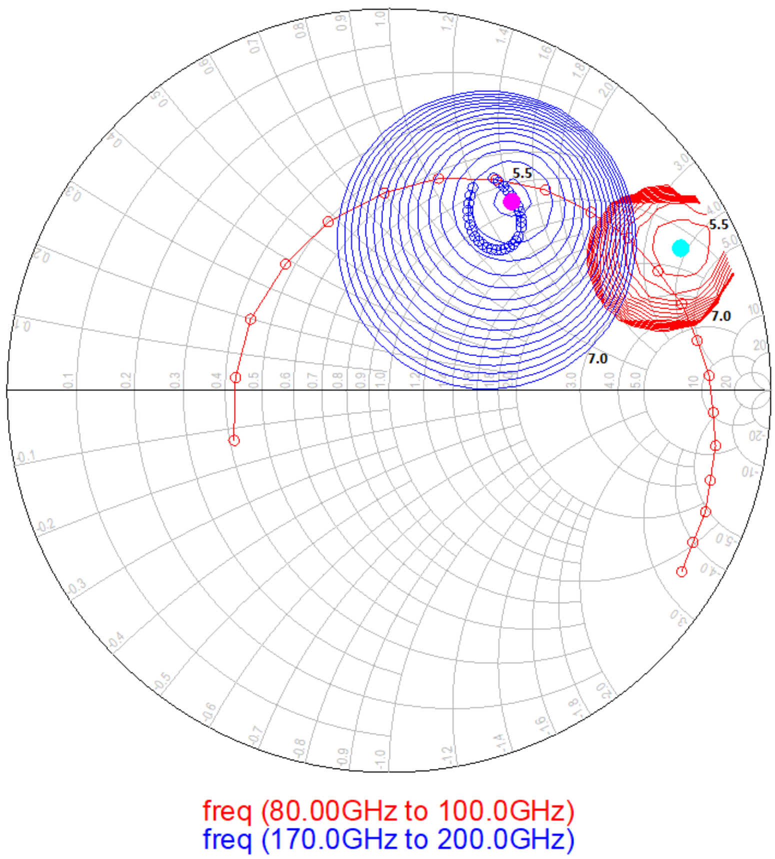

Figure 3.25: The impedance seen at one of the Schottky junction lumped ports with the opposite port terminated with an open circuit. The contours and optimum impedances (dots) are at 183 GHz and 91 GHz.

3.11 LO probe and LO choke filter

When tuning the LO/RF matching network and the RF choke filter the LO frequency reflection coefficient at the LO port was set to $\Gamma_{LO} = 0.6\underline{/69°}$. This assumption was based on a S-parameter simulation of the LO probe which showed a large inductive response at the port connecting to the RF filter. To obtain a broadband frequency response the waveguide height, the position of the waveguide backshort and the position of the waveguide stepped impedance interface were tuned.

Figure 3.26 shows a simple LO probe where the waveguide backshort is to the right and the blue arrow indicates the deembedding distance at the port connecting to the RF filter. A similar deembedding is done at the IF port located on the opposite side of the probe. The width of the conductor has been adjusted to fit the conductor width of the RF filter. Depending on the waveguide height the reflection coefficient at the RF filter port changes, this can be seen in Figure 3.27. The waveguide with a strongly reduced height (560 µm) gives a reflection coefficient with larger inductive reactance while its resistance is constant for a frequency range of 80 GHz to 100 GHz. This is desired since $\Gamma_{LO} = 0.6\underline{/69°}$ has a large inductive reactance. A LO probe with a waveguide height of 560 µm was thereby chosen. By tuning the backshort and the waveguide stepped impedance interface the return loss seen in Figure 3.28 was obtained. The return loss is below -10 dB from 83 GHz to 97 GHz and below -20 dB form 85 GHz to 95 GHz.

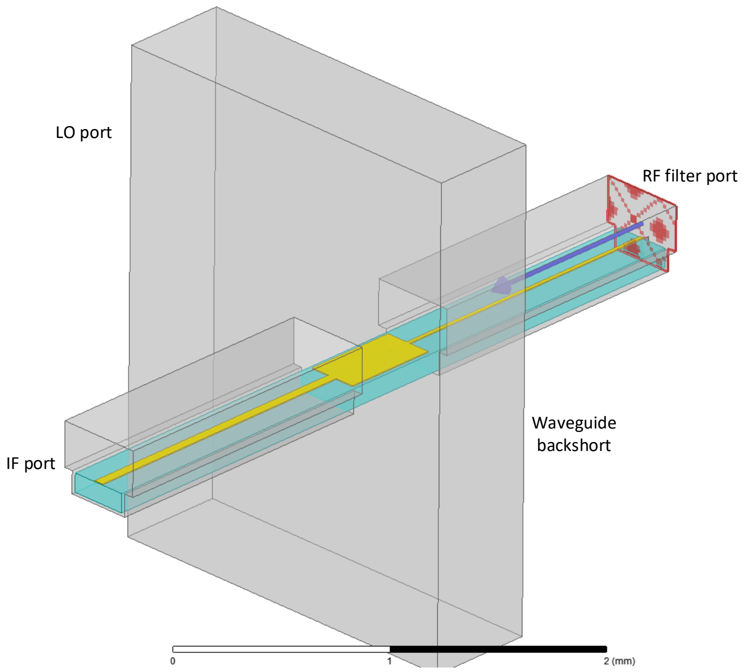

Figure 3.26: A simple 3D-model of the LO probe which is tuned to give a high inductive response. The blue arrow shows the deembedding distance at the port connecting to the RF filter.

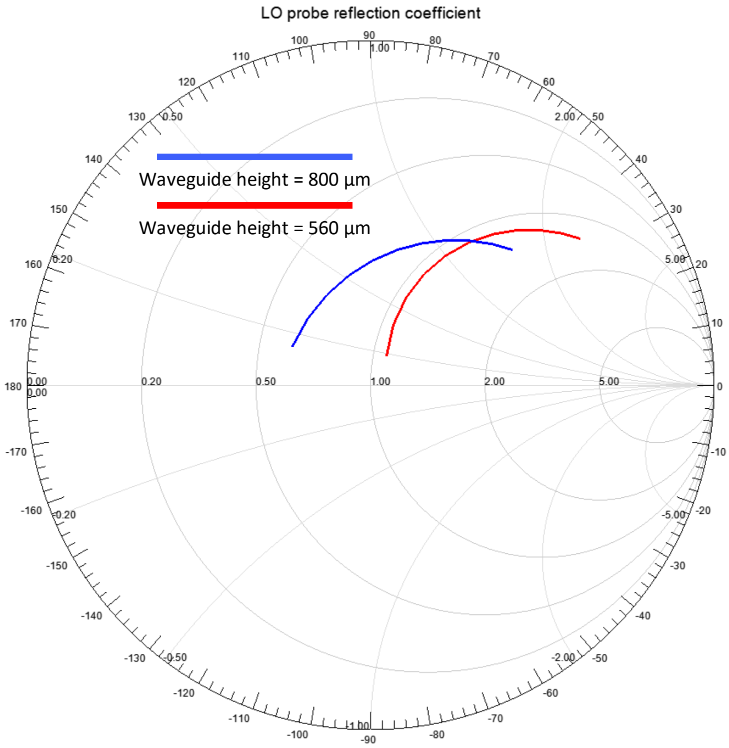

Figure 3.27: The LO probe response at the RF filter port for different waveguide heights. The waveguide with strongly reduced height (560 µm) gives a reflection with larger inductive reactance. The frequency range is 80 GHz to 100 GHz.

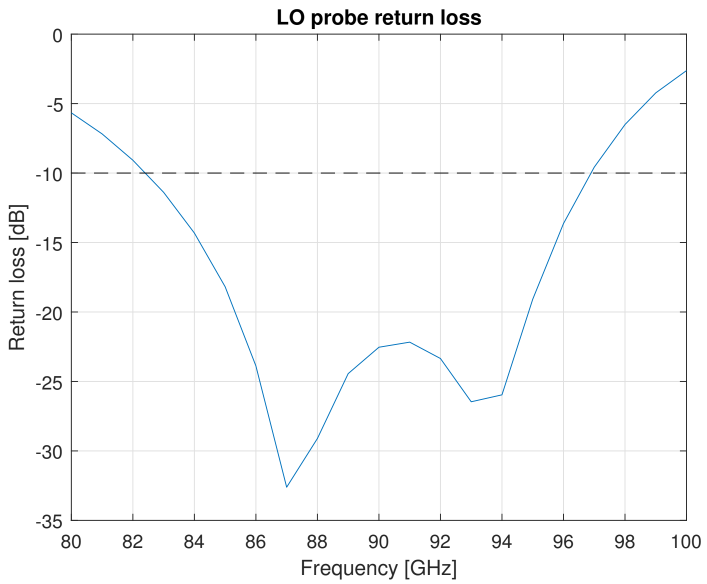

Figure 3.28: Return loss of the LO probe at the RF filter port normalised to $\Gamma_{LO}^{*} = 0.6\underline{/-69}$. The LO port is terminated with the WR-10 impedance.

3.11.1 LO choke filter

To achieve a good LO impedance match a high rejection LO choke filter at the IF port was required, this was observed during the tuning of the LO probe. As described in section 2.3.2 a hammerhead filter provides high rejection due to its multiple resonances, moreover the length can be decreased compared to a stepped impedance filter. Due to these advantages the hammerhead filter was the most reasonable choice. The LO choke filter was directly implemented in HFSS to include the coupling to the walls and the coupling between fingers. The design can be seen in Figure 3.29 where the filter is located in the cavity. The main body of the filter was made as wide as possible to introduce a large capacitance to the ground. The length of the fingers were set to a quarter wavelength (at a frequency of 91 GHz) and the design was then tuned by changing the length of the fingers and the length of the main body. By tuning these lengths the suppression could be centred around 91.5 GHz. The filter performance is shown in Figure 3.30, the suppression is better than -20 dB from 85 GHz to 98 GHz which covers the LO band. The resonances at 90 GHz and 94 GHz give a high level of suppression (- 50 dB) at the centre of the LO band.

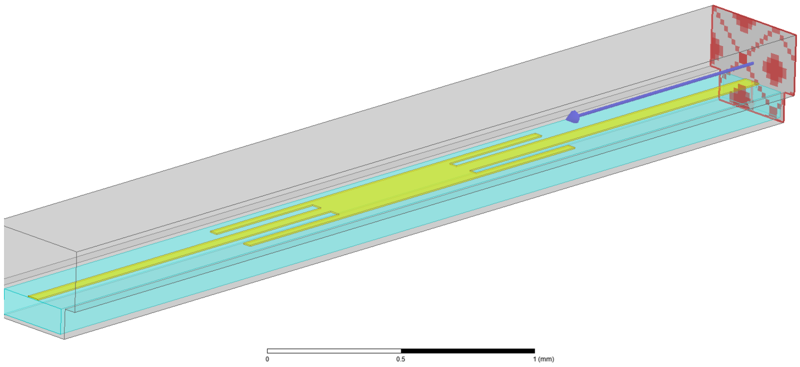

Figure 3.29: LO choke filter implemented as a hammerhead filter to obtain high rejection and to reduce the filter length.

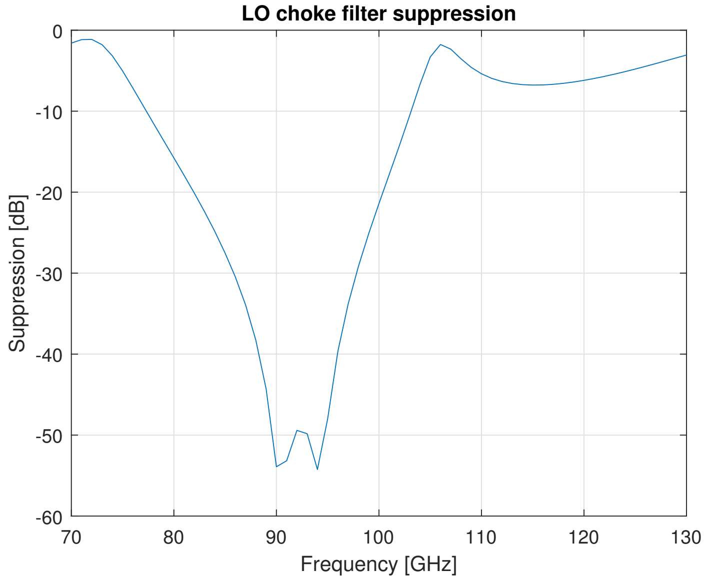

Figure 3.30: Suppression obtained with the hammerhead filter 3D-model.

3.12 The mixer S-parameters

A final S-parameter simulation was performed with the full mixer model, the result is shown in Figure 3.31 where the diode circuit embedding impedance is plotted in the Smith chart. It can be seen that the RF impedance is kept at a conversion loss level of 5.6 dB or better and that the LO match is at a conversion loss level around 7 dB or worse. However the contours are at a minimum LO power (-3 dBm), the LO match is therefore expected to become better when increasing the LO power. By comparing with the Smith chart in Figure 3.25 it can be concluded that the RF match is maintained and that the LO match is worse implying that the LO probe and LO choke filter is degrading the LO match. Improving the LO impedance requires tuning of the LO probe but this would degrade the impedance match at RF, a trade off was therefore done in favour of the RF match.

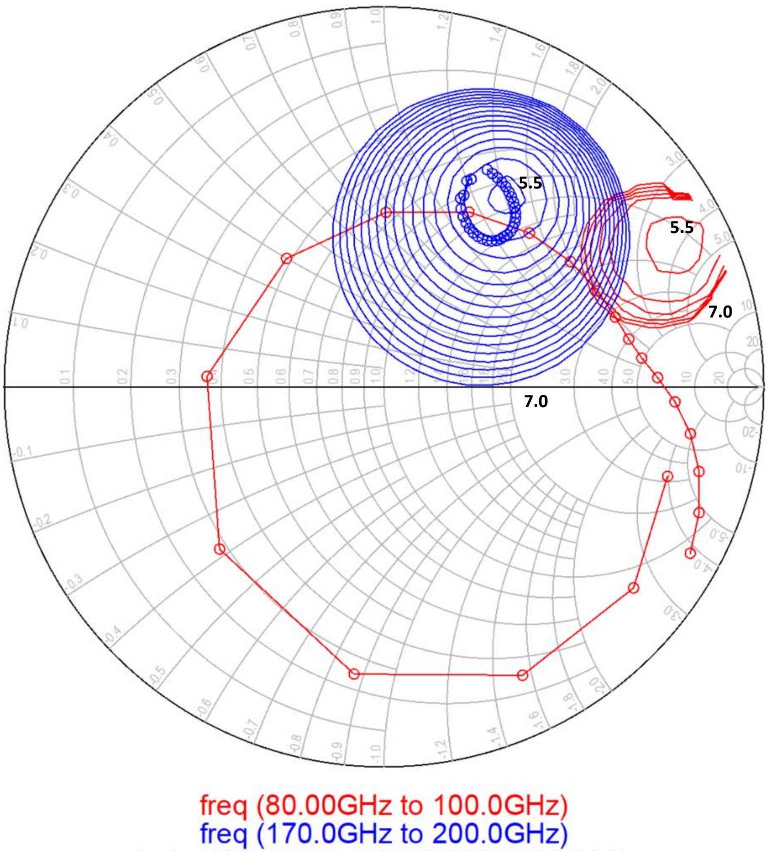

Figure 3.31: Diode circuit embedding impedance of the mixer seen at one of the Schottky junction lumped ports with the opposite port terminated with an open circuit. The conversion loss contours are taken from the ideal load-pull simulation where the LO power was -3 dBm, the RF was 183 GHz and the LO frequency was 91 GHz. The RF contour step is 0.1 dB and the LO contour step is 0.3 dB.

3.13 Glue position

The final step of the mixer design was to decide where to position the glue that holds the substrate in place. Figure 3.32 shows the final design without the diode and the substrate. The substrate platforms have a height of 10 µm and it is possible to place glue in between these. The glue will occupy a volume of about 300 µm x 300 µm x 10 µm which means that the length of the glue is about $\lambda/4$ at RF, it is therefore not a good choice to place the glue in the region of the RF filter or the LO/RF matching network since it will increase the RF loss. Positioning the glue at the IF side of the LO probe is likely to give the best performance since then it will not affect the RF signal nor the LO signal. To ease the assembly of the substrate another platform was added beneath the LO filter and this made it possible to place glue between the LO filter and the LO probe. By first placing the glue onto the cavity floor and then positioning the substrate, using the LO waveguide as reference, a good substrate alignment is likely to be obtained. Positioning the glue in the centre of the substrate gives a relaxed substrate.

By only applying glue at one position the problem related to mechanically stressed substrates is avoided which improves the reliability of the mixer.

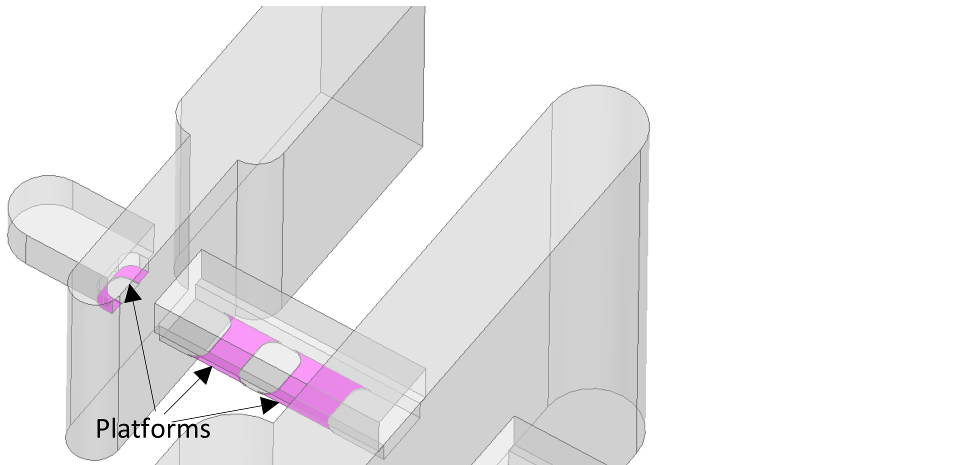

Figure 3.32: Substrate platforms in the model with the LO waveguide implemented. Another platform below the LO choke filter was added to this model.

Incisions in the cavity walls were created in the region of the glue, this to make it possible for excess glue to escape when pushing down the substrate. Figure 3.33 shows the model with incisions which are seen to the right of the hammerhead filter.

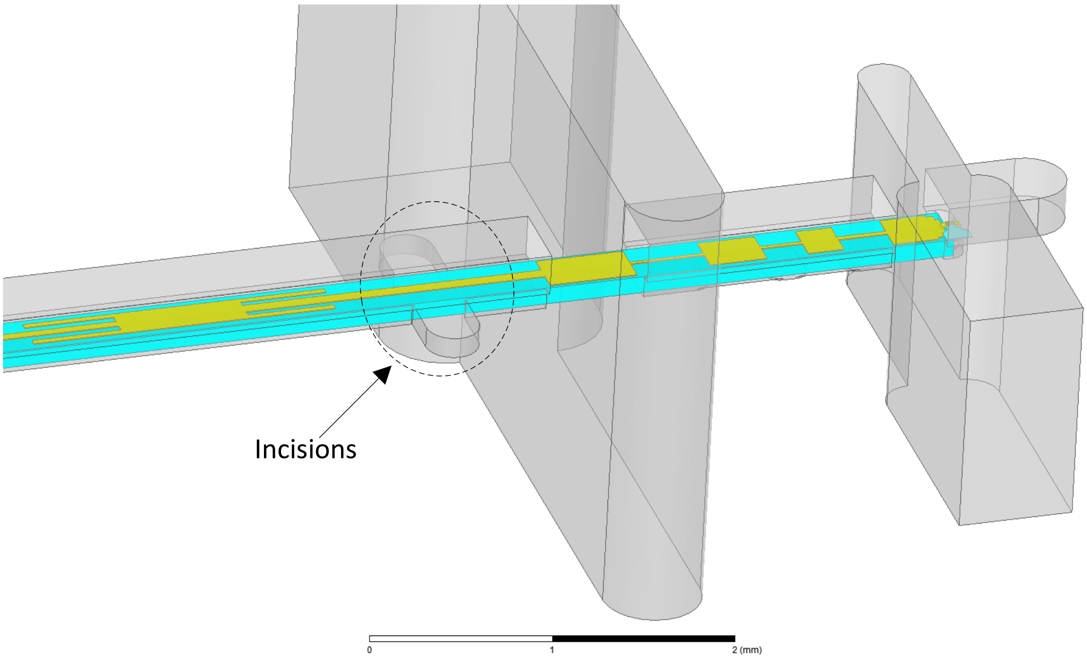

Figure 3.33: Mixer model with incisions in the cavity walls.

3.14 The mixer implemented in the front-end

The mixer was implemented in the front-end together with a IF MMIC LNA, a LNA matching network, DC-bias circuit and a 50 Ω transmission line. This front-end is seen in Figure 3.34. The LNA matching network match the high impedance of the mixer (≈ 200 Ω) to the LNA impedance which was 50 Ω. The transmission line was designed by optimising the conductor width and the length of chamfers such that a 50 Ω impedance was obtained for the whole IF-band (0.5 GHz-8 GHz).

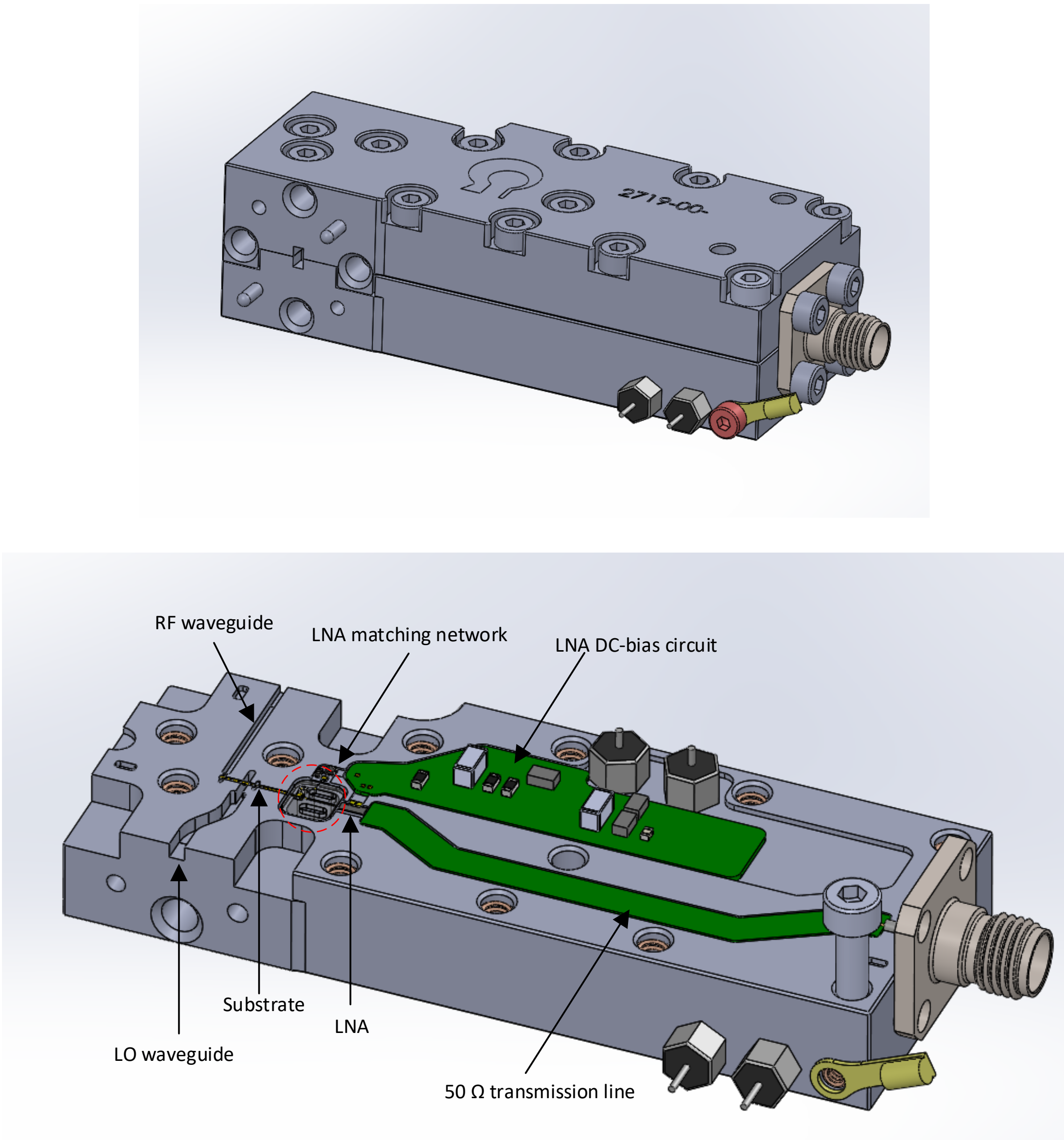

Figure 3.34: The front-end designed at Omnisys. The block measures 67 mm × 25 mm × 19 mm. In the bottom picture is the lower split-block seen where the mixer, matching network, LNA, transmission line and DC-bias circuit are indicated.

4

Results of simulation and fabrication

In this chapter the simulated performance of the final mixer is presented. The result of the fabrication error analysis is also given and the impact of the diode parameters is presented. Harmonic balance simulations were performed using the S-parameters obtained with the finite element method 3D-electromagnetic simulations.

4.1 Mixer performance

The complete mixer model with the LO probe and LO choke filter implemented is seen in Figure 4.1. This model was used in a harmonic balance simulation to investigate the mixer performance.

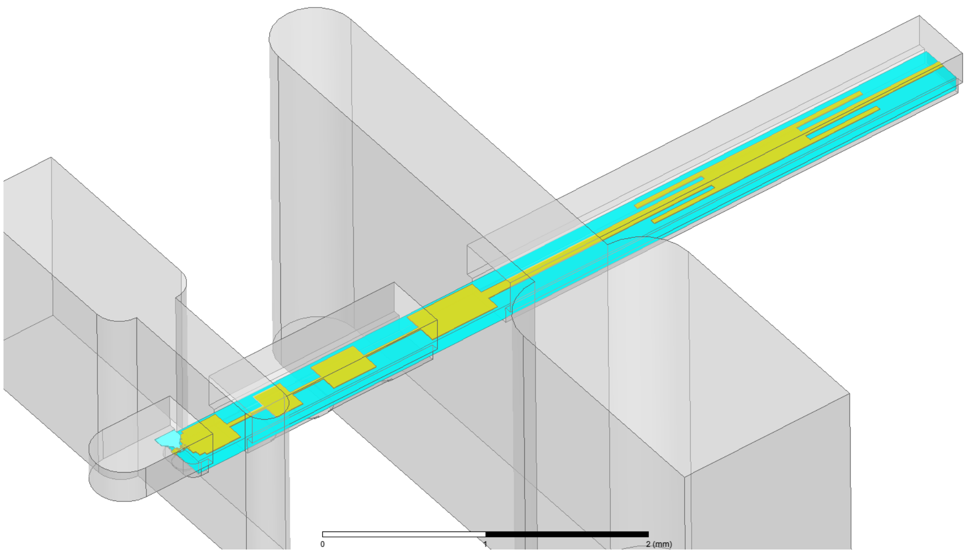

Figure 4.1: Complete mixer model.

The harmonic balance results are found in Figure 4.2, Figure 4.3 and Figure 4.4. The conversion loss is below 7 dB from 170 GHz to 198 GHz with a minimum of 6.2 dB for a LO of 91.2 GHz giving a RF bandwidth of 15 %. Comparing with the initial mixer simulation conversion loss in Figure 3.23 it can be seen that the minimum conversion loss has increased due to ohmic losses and that the LO bandwidth has increased. The increase in LO bandwidth is due to the improved impedance match between the LO probe and the RF filter which was achieved by co-tuning the two subcircuits. The sideband balance in Figure 4.2 is better than 0.5 dB for LO frequencies ranging from 87.3 GHz to 96.3 GHz. The RF port return loss, seen in Figure 4.3, is similar to the frequency response in Figure 3.24 implying that the impedance match at RF was not disturbed when connecting the LO probe and the LO choke filter. The obtained LO bandwidth was calculated from the conversion loss plot in Figure 4.2 resulting in a LO bandwidth of 6 GHz (89 GHz to 95 GHz) corresponding to about 6 %. Notice that the conversion loss is not sensitive to LO losses.

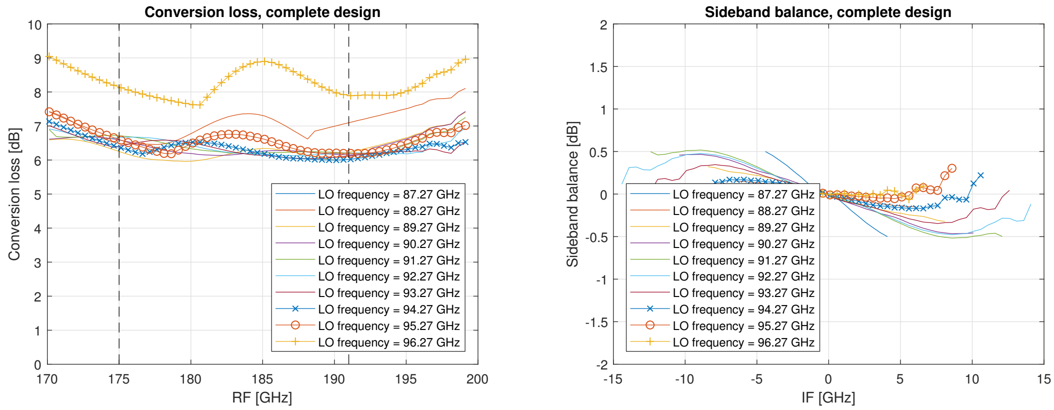

Figure 4.2: Conversion loss and sideband balance of the complete mixer design. The LO power was 2.5 dBm and the RF power was -60 dBm.

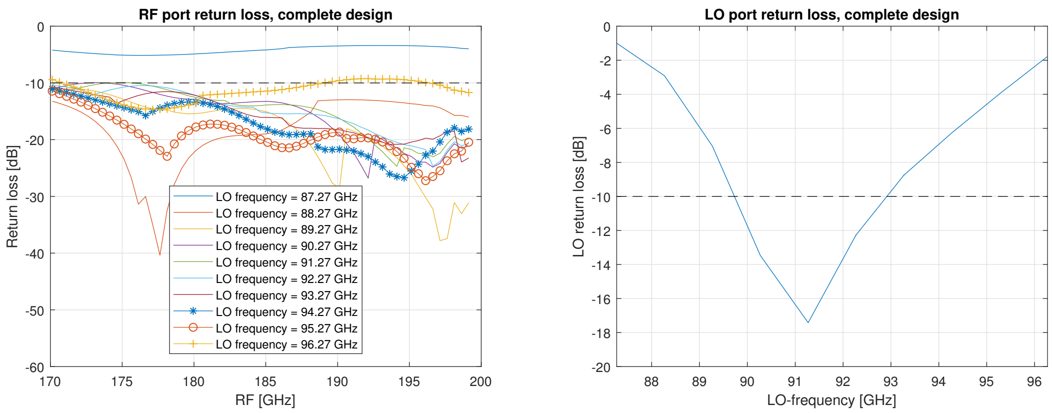

Figure 4.3: Return losses at the RF port and LO port of the complete mixer design. The LO power was 2.5 dBm and the RF power was -60 dBm.

The RF filter suppression in Figure 4.4 is higher than 25 dB. As described in section 3.9 the filter suppression is dependent on the LO probe impedance which explains the variations. Since the suppression is high for the whole RF band the conversion loss does not get disturbed and the ripple can therefore be tolerated. The LO choke filter suppression, also seen in Figure 4.4, reveals resonances at 91 GHz and at 94 GHz which is in accordance with the filter design in Figure 3.30 where resonances at 90 GHz and 94 GHz were obtained by tuning the hammerhead fingers.

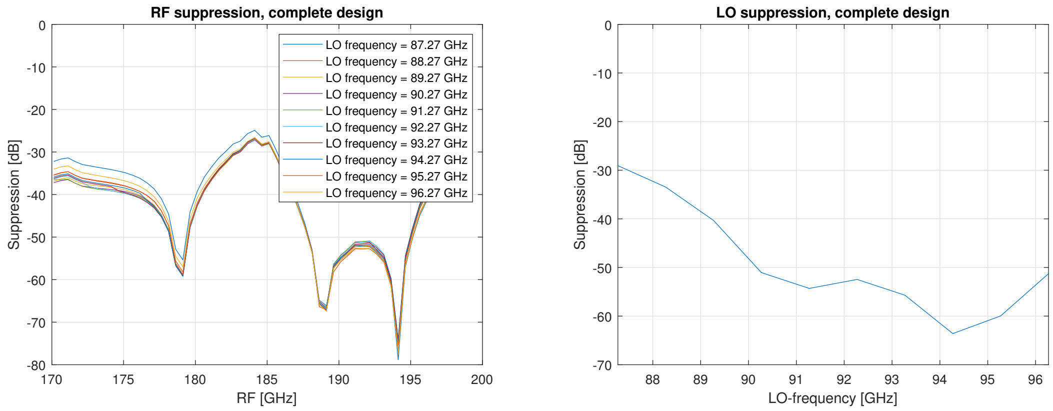

Figure 4.4: Filter performances of the complete mixer design. The RF suppression is between the RF port and the LO port and the LO suppression is between the LO port and the IF port.

The mixer DSB noise temperature was simulated with a standard harmonic balance setup which include the shot-noise and the thermal noise contributions. This simulation accounts for the ideality factor but not for the hot-electron noise which increase with LO power. The result is seen in Figure 4.5. The model used in this simulation was complemented with wall losses and the gold conductivity was set to 20.5 S/µm, which is half of the conductivity used before, to represent the surface roughness. The conversion loss for this case was similar to the one seen in Figure 4.2 but a slight increase of LO power was needed (0.5 dB). To include the RF waveguide and the IF matching network losses a 1 dB attenuator and a 0.5 dB attenuator was added to the RF port and the IF port respectively. It can be concluded that the minimum T_{DSB} is 360 K and that the optimum LO power is 4 dBm which agrees with the conversion loss. When increasing the LO power beyond the optimum point the noise increase due to the power dependent shot-noise.

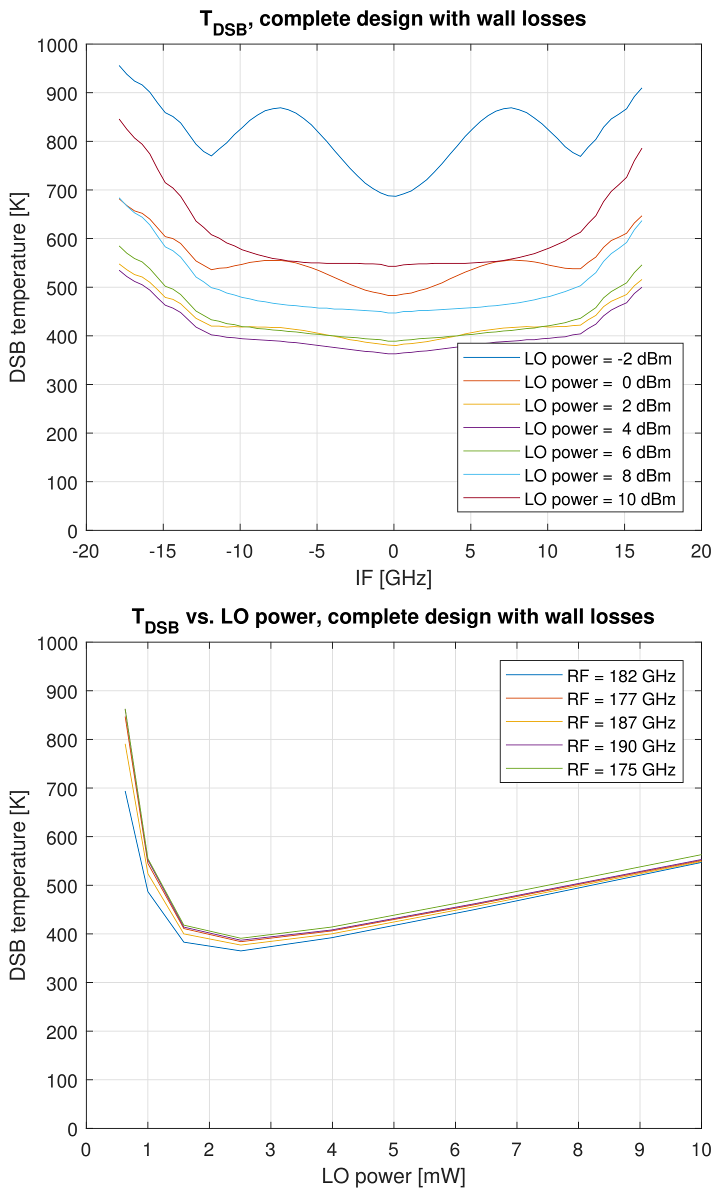

Figure 4.5: Double-sideband noise temperature of the mixer with wall and conductor losses included. The gold conductivity was set to 20.5 S/µm. External attenuators were connected to the RF port and the IF port with 1 dB and 0.5 dB of attenuation respectively.

4.2 Assembly and fabrication aspects

In this section the mixer sensitivity to fabrication errors is analysed, this to investigate whether tuning of the nominal design is required. It is also investigated how the glue impacts on the performance and the optimum diode size is determined based on the series resistance and the junction capacitance.

To investigate how the glue impacts on the performance of the mixer the model was complemented with a material having the electrical properties given in Table 4.1. Two cases were analysed, the H20E glue and the 2216 glue and Figure 4.6 shows the incisions filled with glue. The conversion loss and return losses were compared with the nominal design which can be seen in Figure 4.7 to Figure 4.9. The impact is barely noticeable, the conversion loss is the same for all cases. The RF port return loss is indicating that the position of the glue is well chosen. There is a small difference in LO port return loss, the H20E glue gives a slightly better return loss and the 2216 glue gives a small frequency shift towards lower frequencies.

Table 4.1: The electrical properties of the investigated glues.

Glue	Conductivity [S/mm]	Loss tangent	Relative permittivity
H20E	250	0	1
2216	0	0.112	5.51

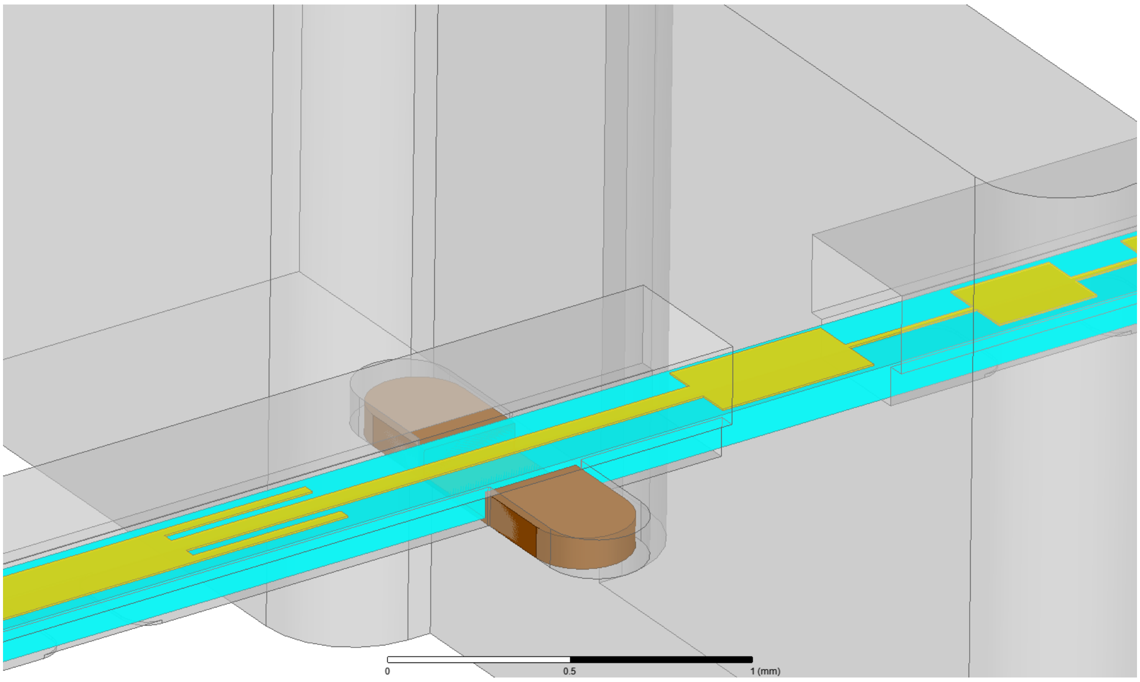

Figure 4.6: Mixer model where the incisions are filled with glue (seen in brown).

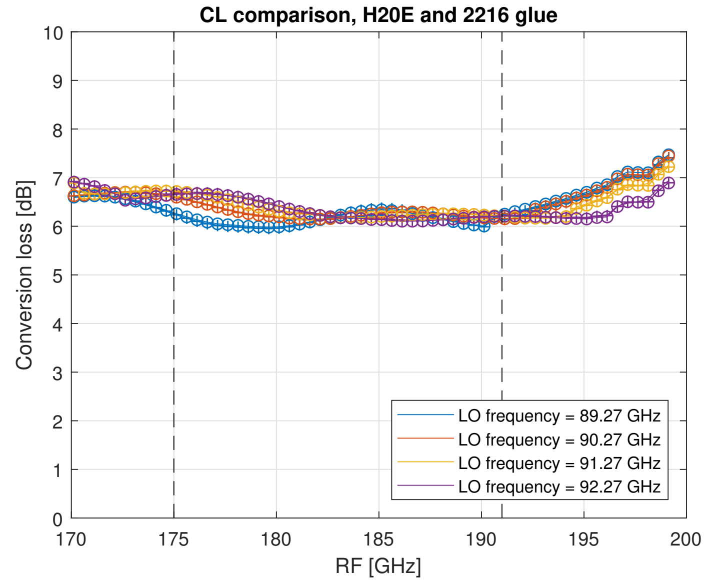

Figure 4.7: Comparison of the conversion loss at a LO power of 2.5 dBm between the nominal design (solid line), the model with H20E (+) and the model with 2216 (o).

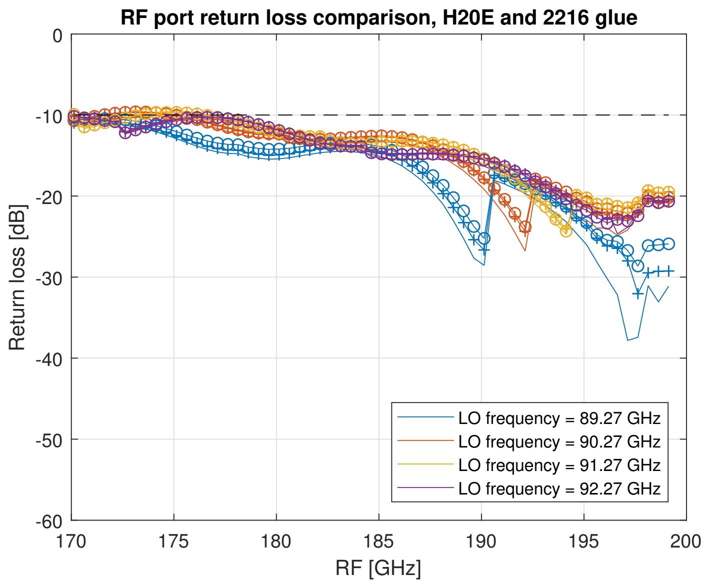

Figure 4.8: Comparison of the RF port return loss at a LO power of 2.5 dBm between the nominal design (solid line), the model with H20E (+) and the model with 2216 (o).

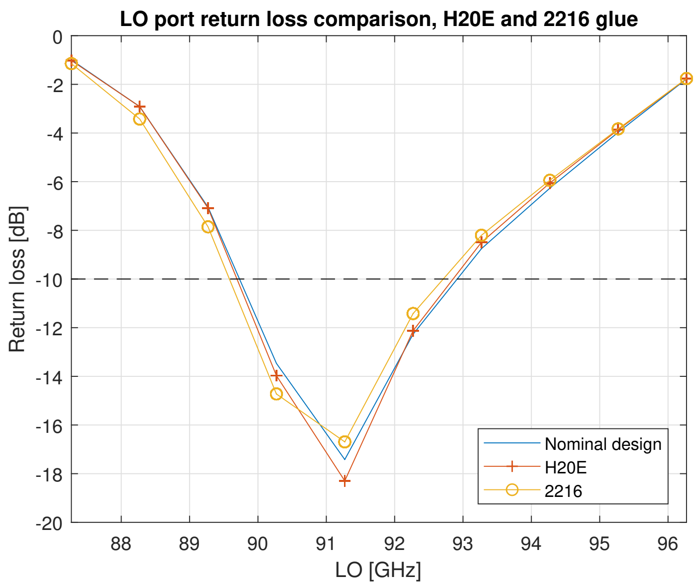

Figure 4.9: Comparison of the LO port return loss at a LO power of 2.5 dBm between the nominal design, the model with H20E and the model with 2216 glue.

4.2.1 Fabrication error analysis

During the fabrication process a number of different fabrication errors can occur. The mechanics has a certain dimension tolerance in the order of ±20 µm and a substrate misalignment of 10 µm is expected. The position of the Schottky diodes may also become different from the nominal design as well as the beamlead length. A rigorous tolerance analysis has been done where changes in substrate placement, diode placement and cavity dimensions have been investigated. The conclusion was that the mixer was most sensitive to substrate movement. Moving the substrate along the cavity did not affect the performance but a change in the vertical direction or in the horizontal direction showed to be the two most critical parameters. The substrate displacements that were analysed can be seen in Figure 4.10 where the substrate is seen in blue and the cavity walls and floor are seen in grey. Figure 4.11 shows the conversion loss at a LO frequency of 91.27 GHz where the substrate position is changed in the vertical direction. It can be seen that pushing the substrate down such that it is in perfect contact with the support platforms (delta height = 0 µm) cause a ripple in the conversion loss. This is also the case if the substrate is raised as much as 20 µm. A displacement in the horizontal direction gives a similar ripple as seen in Figure 4.12. In fact this movement is the most critical one since a displacement of only ±9 µm introduce a ripple. It is therefore crucial to make sure that the substrate is centred in the cavity.

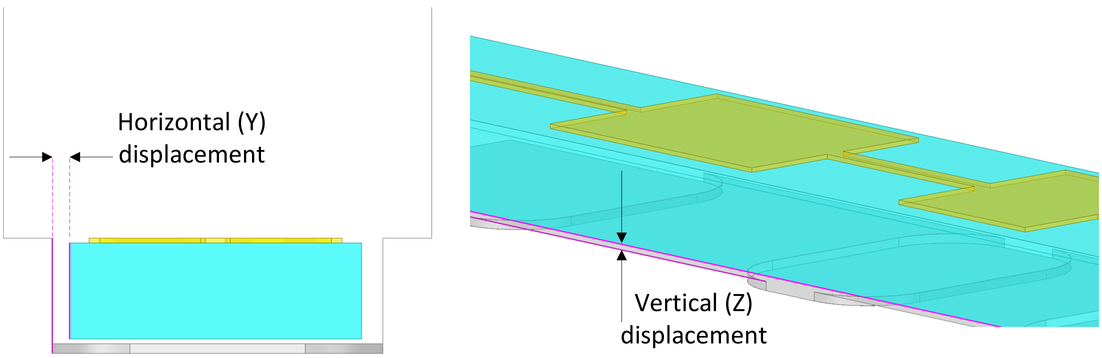

Figure 4.10: The horizontal and vertical substrate displacements analysed.

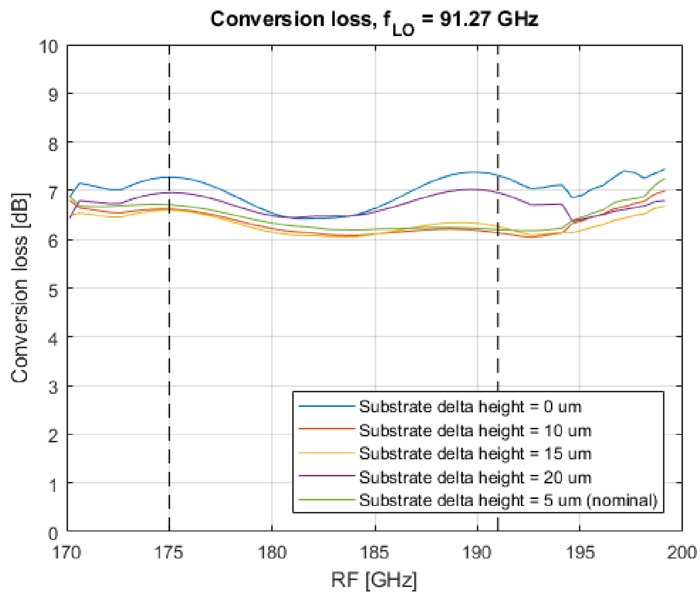

Figure 4.11: Conversion loss at $f_{LO} = 91.27\,\text{GHz}$ for a substrate movement in the vertical direction. The LO power was 2.5 dBm.

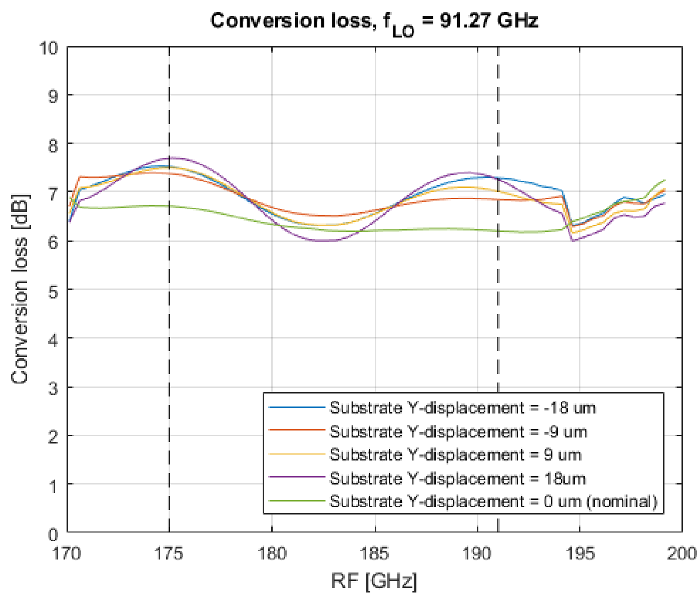

Figure 4.12: Conversion loss at $f_{LO} = 91.27\,\text{GHz}$ for a substrate movement in the horizontal direction. The LO power was 2.5 dBm

4.2.2 Diode analysis

The final analysis of the mixer was to investigate the optimum diode size based on the series resistance and the junction capacitance. The nominal anode junction area was 1.6 µm^2. Increasing the size will give a lower series resistance (lower thermal noise and better conversion loss) but as the diode gets bigger the parasitic capacitances will become more prominent. This reduces the amount of power delivered to the junction which reduces the conversion loss. The trade-off is obvious, one must find a size which gives low parasitic capacitances at the same time as R_s does not become too big. In the analysis were six different sizes used, these are given in Table 4.2. The conversion loss, LO port return loss and the RF port return loss for each of these cases are seen in Figure 4.13 and Figure 4.14. From the conversion loss only a small difference can be seen between the cases. The LO port return loss shows that the biggest size gives the worst return loss. The nominal design and the 1.4 µm^2 case are centred at 91.25 GHz but the latter gives a small increase in bandwidth. From this it was decided to fabricate two diode sizes, the nominal and 1.4 µm^2 since the nominal size gives a bit better conversion loss but the smaller size has a better LO port return loss.

Table 4.2: Investigated diodes

Area [µm^2]	R_s[Ω]	η	C_j[fF]
1.1	10.0	1.3	2.5
1.2	9.2	1.3	2.8
1.3	8.5	1.3	3.0
1.4	8.1	1.3	3.2
1.6	7.0	1.3	4.8
1.8	6.0	1.3	4.2

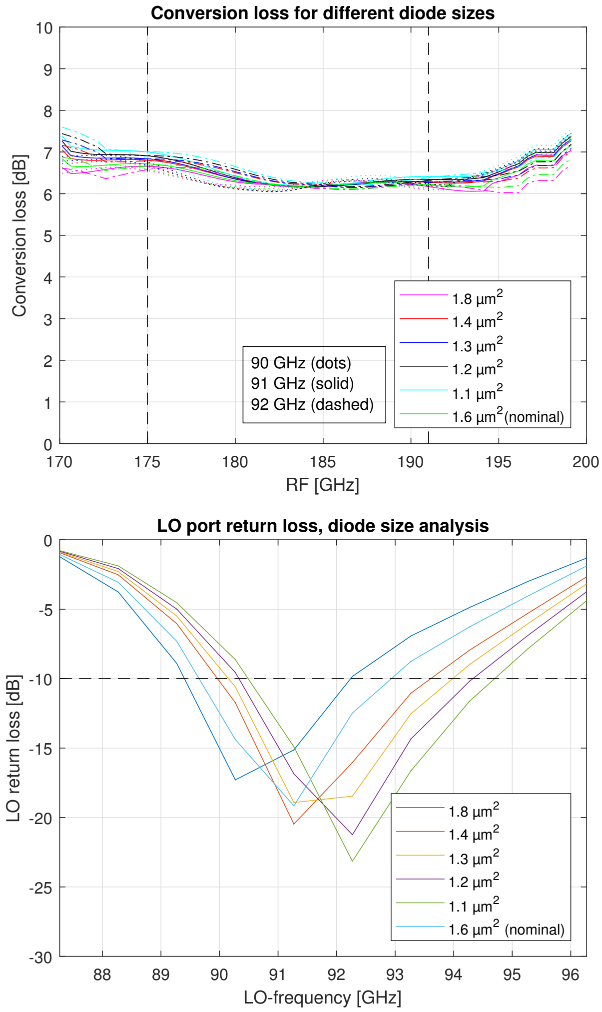

Figure 4.13: The conversion loss for different diode sizes and LO frequencies and the LO port return loss for different diode sizes. The LO power was 2.5 dBm.

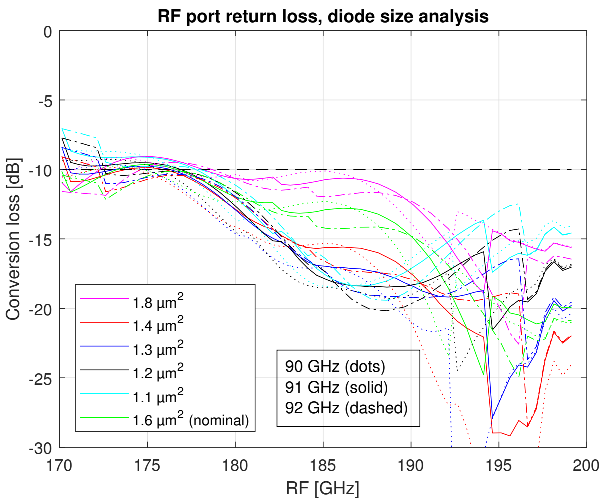

Figure 4.14: The RF port return loss for different diode sizes and LO frequencies. The LO power was 2.5 dBm.

4.3 Substrate measurements

The quartz-substrate, shown in Figure 4.15, was supplied by Applied Thin-film Products. The incoming inspection is summarised in Table 4.3 where some of the measurements are presented. It was concluded that the gold and the quartz were well within their tolerances, ±5 µm for the gold and ±25 µm for the quartz. The repeatability was observed to be within ±6 µm for the quartz measurements (upper half of Table 4.3) and ±2 µm for the gold (lower half of Table 4.3). In Figure 4.15 is a bond-pad seen, located to the right of the hammerhead filter. This pad is needed when bonding from the substrate to the LNA matching network.

Figure 4.16 shows a typical interface between a high and low impedance section. The mask used to plate the gold has created 90 °corners with some minor imperfections. The edges of two hammerhead fingers are seen in Figure 4.17 and a sideview of the substrate is seen in Figure 4.18.

Figure 4.15: Fabricated substrate, the hammerhead filter is shown to the right and the RF-probe is shown to the left. The nominal dimensions are 5.488 mm × 300 µm.

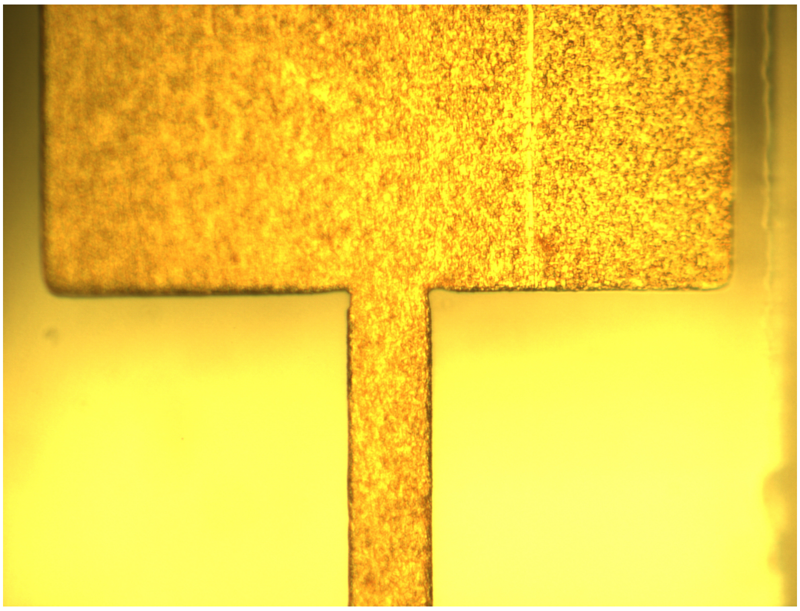

Figure 4.16: Interface between a high impedance section and a low impedance section.

Table 4.3: A summarised incoming inspection of the substrates. The quartz tolerance was ±25 µm and the gold tolerance was ±5 µm. The substrate thickness was measured at both ends of each substrate.

Identifier	**Nominal** [µm]	**Measured No. 1**[µm]	**Measured No. 2** [µm]	**Measured No. 3** [µm]
Substrate length	5488	5495	5495	5493
Substrate width	300	302	302	308
Substrate thickness	100	108 (97)	111 (107)	107 (112)
RF probe length	320	321	321	323
RF probe width	260	262	261	263
RF filter section 1 width	30	30	32	33
RF filter section 1 length	282	281	282	280

* () second measurement

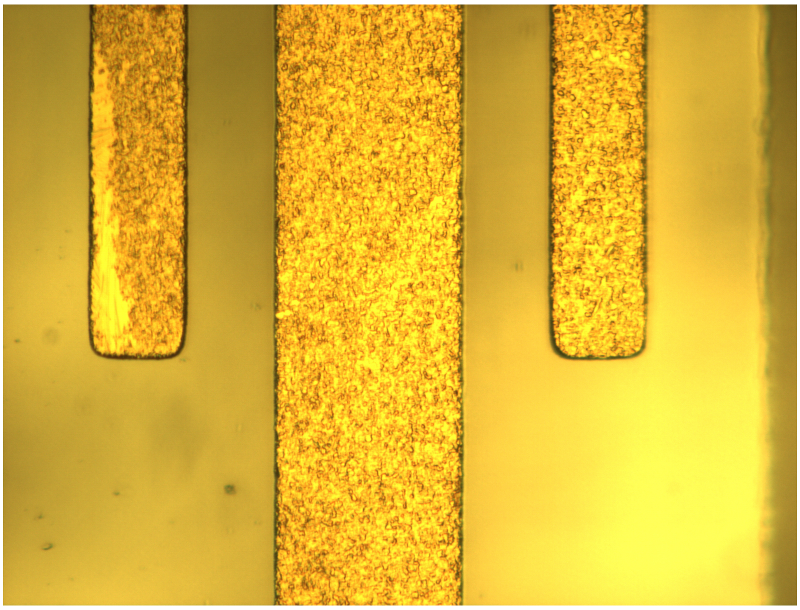

Figure 4.17: The edges of two hammerhead fingers at the LO probe side.

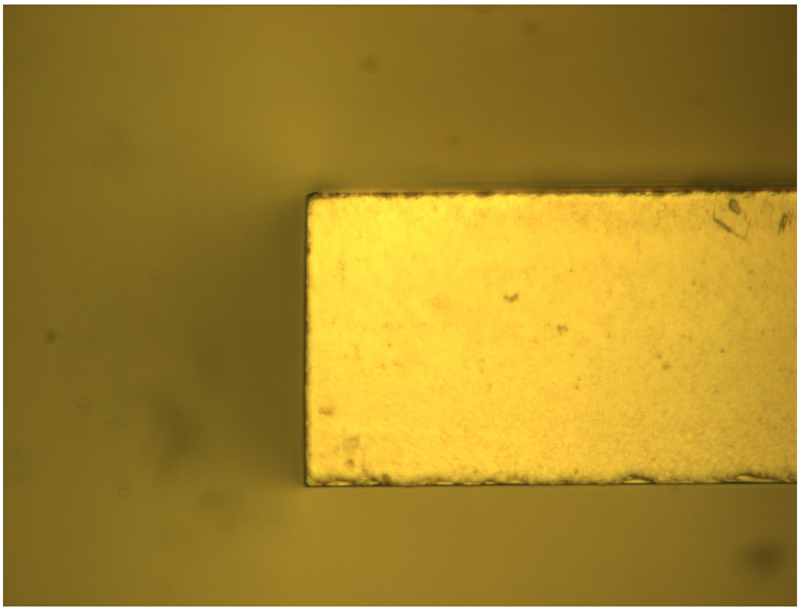

Figure 4.18: A sideview of the substrate end. The nominal thickness is 100 µm

4.4 Split-block measurements

The aluminium split-blocks were fabricated inhouse at Omnisys and a summary of the incoming inspection is given in Table 4.4. All the dimensions were within ±10 µm from the nominal value but the majority of the measurements showed a deviation of only ±5 µm.

Figure 4.19 shows two photographs of the RF waveguide and the substrate cavity. In the upper picture is the stepped impedance interface seen to the right and the backshort is seen to the left. The platform where the diode will be mounted is seen at the end of the substrate cavity. The lower photograph shows the substrate platforms which have a nominal height of 10 µm. The LO and RF waveguides are seen in Figure 4.20 together with the glue cavities at each side of the substrate cavity.

Table 4.4: A summarised incoming inspection of the lower split-block before gold plating. The split-blocks were fabricated by Omnisys.

Identifier	**Nominal** [µm]	**Measured No. 1**[µm]	**Measured No. 2** [µm]	**Measured No. 3** [µm]
RF waveguide height	653	656	657	653
LO waveguide height	1273	1276	1276	1273
Cavity height 1	110	110	108	109
Cavity height 2	120	118	121	121
LO waveguide width	570	578	573	575
RF waveguide width	310	312	309	309
RF filter cavity length	1413	1404	1409	1409

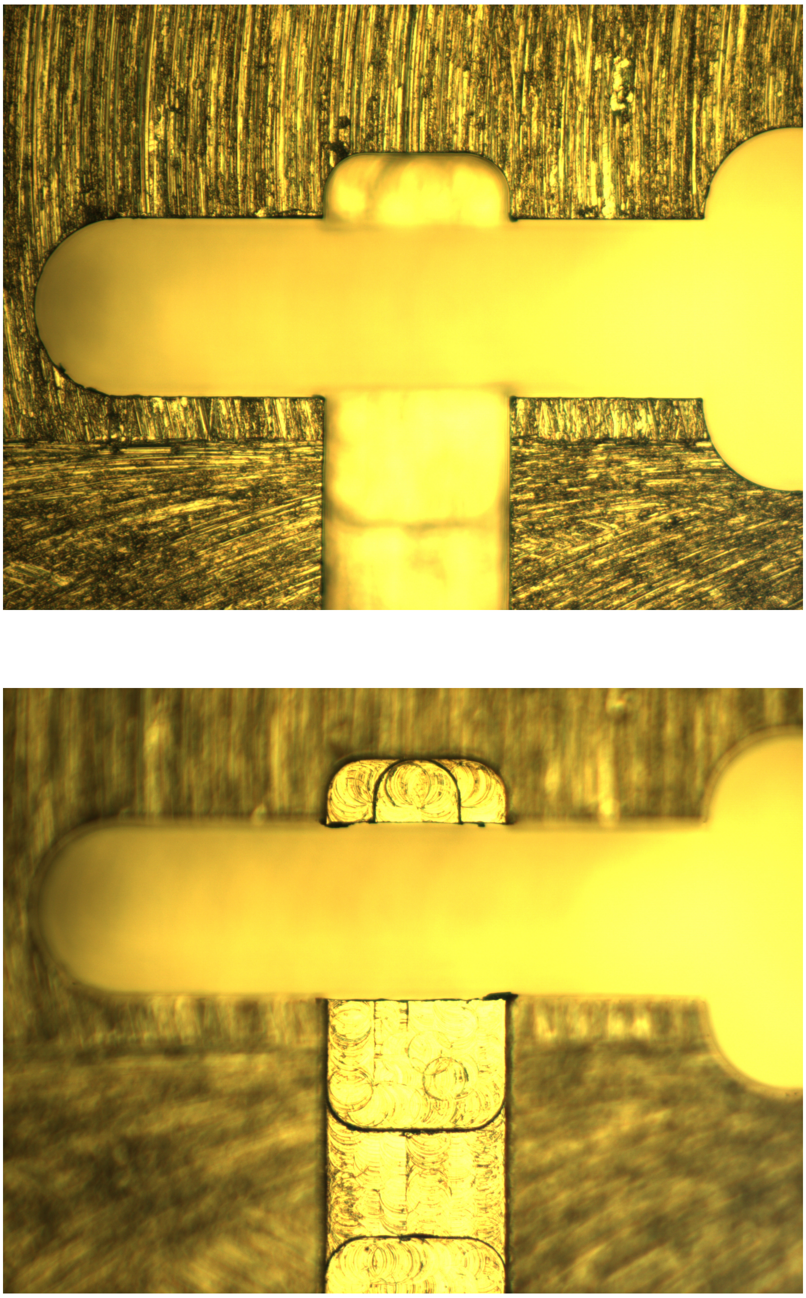

Figure 4.19: The fabricated RF waveguide and the substrate cavity. The bottom picture shows the platforms on which the substrate rests.

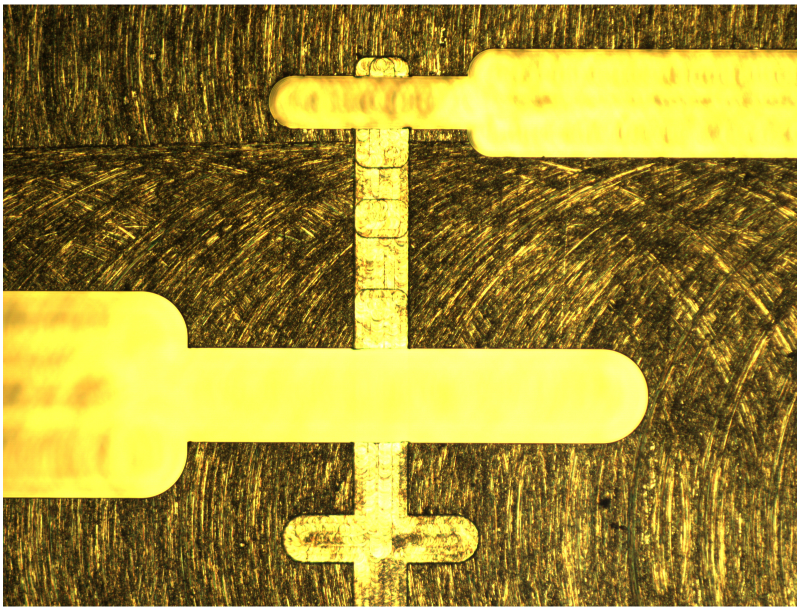

Figure 4.20: The fabricated RF and LO waveguide with the glue cavities on each side of the substrate cavity.

The substrate and the diode were mounted inside the lower split-block channel, this is seen in Figure 4.21 where the substrate is positioned in the cavity and the diode is placed at the end of the substrate. The suspended diode is shown in Figure 4.22, unfortunately was the substrate misaligned in the horizontal direction by 36 µm. This needs to be improved.

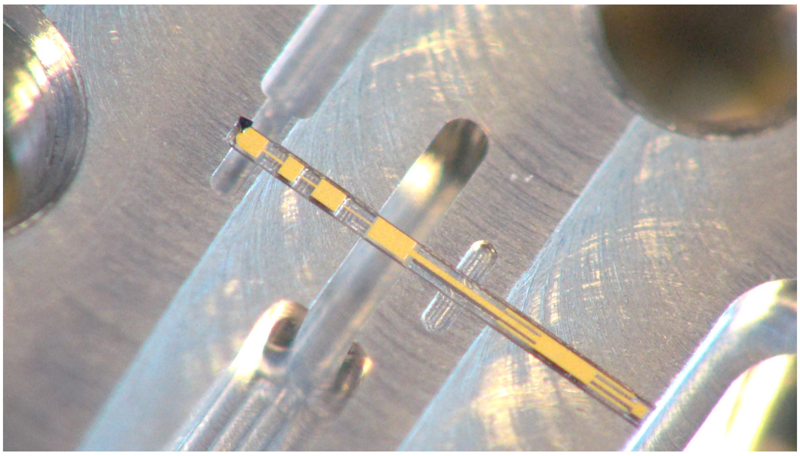

Figure 4.21: The substrate placed in the lower split-block. The diode is seen at the end of the substrate.

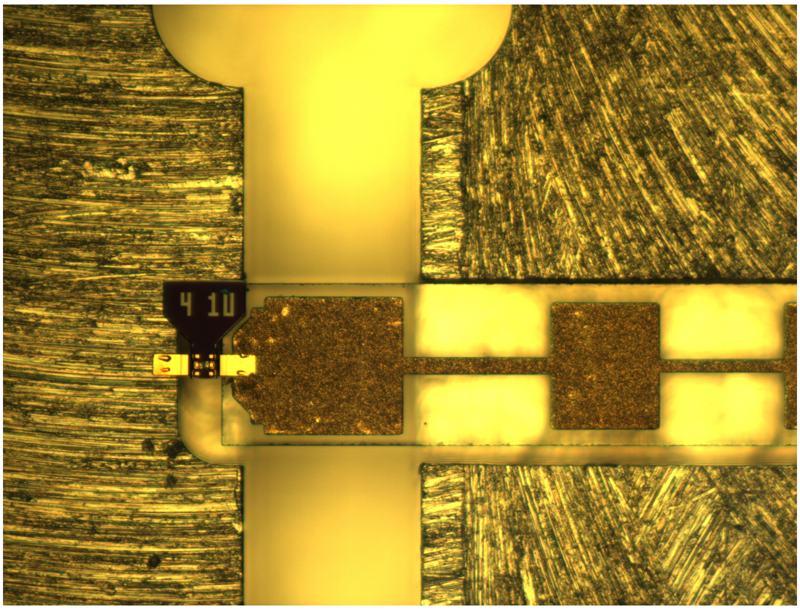

Figure 4.22: A photograph of the suspended diode.

4.5 Noise temperature measurement

The mixer with an integrated LNA was characterised by an Y-factor measurement. A hot load at 80 °C and a cold load at room temperature were used as black body radiation sources. The IF output band was divided into three regions; 2 GHz ± 2 GHz, 6 GHz ± 2 GHz and 10 GHz ± 2 GHz. The measured and simulated DSB noise temperatures are given in Figure 4.23. The receiver noise temperature has a minimum of 550 K and an average temperature of 650 K within the required IF band (0.5 GHz - 8 GHz). This includes a horn loss of approximately 0.3 dB. The mixer temperature was deduced by compensating for the LNA noise temperature of 40 K and the horn loss. It has a minimum of 400 K and an average temperature of 487 K. The noise temperature is seen to increase with frequency. This is because of the limited bandwidth of the LNA matching network. At high frequencies the degraded impedance match causes a higher noise temperature which explains the deviation from the simulated mixer noise. It can be seen that the temperature increase rapidly at DC, 4 GHz and 8 GHz. This is due to a non-optimised back-end.

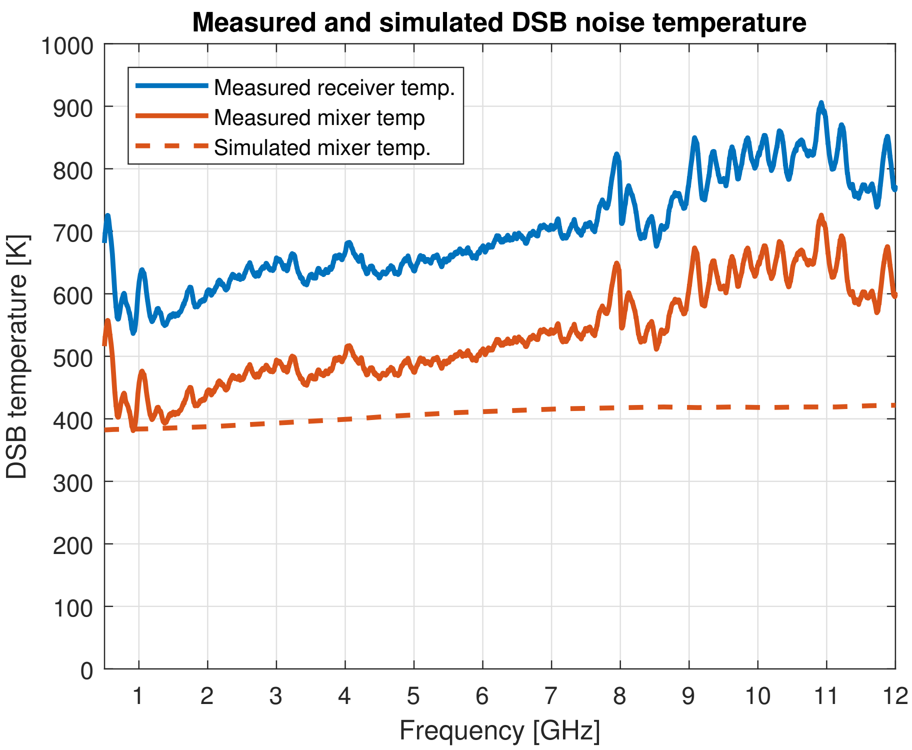

Figure 4.23: Measured and simulated DSB noise temperatures. A horn loss of approximately 0.3 dB is included for the receiver noise temperature. The integrated LNA has a typical noise temperature of 40 K. A gradient can be seen in the measured temperatures which is due to the imperfect matching network between the mixer and LNA. The LO power level was 1.6 mW.

5
Discussion and future work

The mixer showed a measured mixer noise temperature below 600 K clearly fulfilling the requirement. A minimum receiver noise DSB temperature of 550 K was reported which is a performance comparable with the best published results, see Table 5.1. However the matching network between the mixer and the LNA was only able to provide a good impedance match for the lower part of the IF band. This caused an increase in noise at higher frequencies. Since the noise temperature was well below the required 1000 K this will not cause any problems but for applications with high sensitivity requirements this might be an issue. To improve this both the mixer design and the matching network design need to be revised. The high IF impedance of the mixer makes it hard to match the LNA. If this impedance can be lowered the matching network will be able to match the LNA over the full IF band.

The final mixer design showed a conversion loss below 7 dB for a RF bandwidth of 15 % and a LO bandwidth of 6 %, both well above their respective requirements. However for other applications a much larger LO bandwidth is required ($\sim$ 20%). This is a disadvantage of the mixer. The reason for the low bandwidth is partly due to the low LO bandwidth requirement. From a LO perspective the mixer was designed to comply with the fabrication tolerances and the centre frequency. However, the circuit topology is a possible reason for the low bandwidth. It is not understood how the microstrip affects the performance of the E-probes. An interesting analysis would be to compare a probe using the microstrip topology with a probe using the suspended topology. Since a microstrip and a suspended microstrip have different fundamental field distributions the E-field of the probe will differ between the two cases. Using a microstrip topology might give a field distribution that causes a degradation of the bandwidth compared to the suspended topology. Another factor that affects the E-field is the substrate, the quartz confines the field due to its relative permittivity which is larger than one. By reducing the thickness of the substrate the field distribution gets less disturbed possibly implying an increase of bandwidth. There exists commercially available substrates with a thickness of 76 µm where the gold can be plated in the same manner as for the 100 µm thick substrates.

The fabrication error analysis concluded that the mixer was sensitive to substrate displacement in the horizontal and the vertical direction. A misalignment of ± 9 µm in the horizontal direction gave a conversion loss ripple with 1.5 dB peak to peak, the substrate is therefore required to deviate less than 9 µm from the nominal position. Using this result one can estimate an upper frequency limit of the circuit topology. A mixer at 360 GHz would require a substrate placement with a factor two improvement, i.e. the misalignment would need to be ≤ 4.5 µm which is considered to be a practical limit. The topology is therefore seen to be applicable up to about 400

GHz. A recently published mixer using hammerhead filters showed to be robust, with this in mind an improvement would be to replace the stepped impedance RF filter with a hammerhead filter. This would possibly make the design less sensitive to substrate displacement.

Table 5.1: Comparison of discrete Schottky diode mixers designed the past 30 years.

Freq. [GHz]	Harm. index	DSB loss [dB]	DSB noise temp. [K]	Ref.
183	**2**	-	**400**	**This work**
183	2	5	500	[12]
190	2	5.5	550	[6]
200	2	5.7*	795*	[16]
250	1	7.2	1310	[17]
119	1	4*	250*	[15]
330	2	6.3	700	[9]
340	2	7	900	[13]
340	2	5.5	757	[10]

*Value calculated from SSB result.

5.1 Future work

The front-end will continue to be characterised by performing Y-factor measurements with different LO power levels and frequencies. Continuous wave measurements will be performed to measure conversion loss and gain response.

The front-end is intended to be used in the ALMA observatory, which consist of multiple channels in the 84 GHz to 950 GHz range. An important qualification of the receiver is therefore to analyse the mixer spurious frequency components.

6
Conclusion

The mixer design has shown to meet the requirements. The simulated conversion loss was at minimum 6.2 dB and the RF bandwidth was 15 % at a LO power of 2.5 dBm with the microstrip conductor loss included. The noise simulation showed a DSB temperature as low as 360 K at a LO power of 4 dBm fulfilling the required 1000 K. The measured receiver noise DSB temperature had a minimum of 550 K at a LO power of 1.6 mW with the horn loss included. The minimum mixer noise temperature was 400 K. A novel microstrip circuit topology was presented providing full visual inspection and avoids mechanical stress and unreliable soldering processes which have been a major problem in previous mixer designs. The mixer was fabricated with high precision making the mixer design and the circuit topology promising.

Bibliography

[1] S. D'Addio, V. Kangas, U. Klein, M. Loiselet, and G. Mason, "The microwave radiometer on-board MetOp second generation satellites," *IEEE Metro. Aero. Space.*, pp. 599–604, 2014. DOI: `10.1109/MetroAeroSpace.2014.6865995`.

[2] M. P. Cadeddu, J. C. Liljegren, and D. D. Turner, "The atmospheric radiation measurement (ARM) program network of microwave radiometers: Instrumentation, data, and retrievals," *Atmospheric Measurement Techniques*, vol. 6, no. 9, p. 2359, Sep. 2013. DOI: `10.5194/amt-6-2359-2013`.

[3] T. D. D., "Improved ground-based liquid water path retrievals using a combined infrared and microwave approach," *Journal of Geophysical Research: Atmospheres*, vol. 112, no. D15, pp. 1–15, Aug. 2007. DOI: `10.1029/2007JD008530`.

[4] M. Allison *et al.*, "An assessment of aerosol-cloud interactions in marine stratus clouds based on surface remote sensing", *Journal of Geophysical Research: Atmospheres*, vol. 114, no. D9, pp. 1–15, May 2009. DOI: `10.1029/2008JD011006`.

[5] Omnisys Instruments AB. (2017). ALMA water vapor radiometers, [Online]. Available: `http://www.omnisys.se/product/alma-wwr/`.

[6] RPG Radiometer Physics GmbH. (2018). Subharmonic mixer narrowband 170-210 GHz, [Online]. Available: `https://www.radiometer-physics.de/products/mmwave-and-terahertz-products/mixers/mixers-subharmonic-and-harmonic-mixers/high-performance-subharmonic-mixers1/subharmonic-mixer-narrowband-170-210-ghz/#tabs-container-0`.

[7] M. Rösch *et al.*, "Low noise amplifiers for MetOp SG,", presented at the 2016 Global Symposium on Millimeter Waves (GSMM) & ESA Workshop on Millimetre-Wave Technology and Applications, Espoo, 2016. DOI: `10.1109/GSMM.2016.7500336`.

[8] P. J. Sobis, A. Emrich, and J. Stake, "A low VSWR 2SB Schottky receiver," *IEEE Trans. THz Sci. Technol.*, vol. 1, no. 2, pp. 403–411, Nov. 2011. DOI: `10.1109/TTHZ.2011.2166176`.

[9] B. Thomas, A. Maestrini, and G. Beaudin, "A low-noise fixed-tuned 300-360 GHz sub-harmonic mixer using planar Schottky diodes," *IEEE Microw. Compon. Lett.*, vol. 15, no. 12, Dec. 2005. DOI: `10.1109/LMWC.2005.859992`.

[10] C. Wang *et al.*, "Robust sub-harmonic mixer at 340 GHz using intrinsic resonances of hammer-head filter and improved diode model," *J. Infrared Milli. Terahz. Wave*, vol. 38, no. 11, pp. 1397–1415, Nov. 2017. DOI: `10.1007/s10762-017-0436-4`.

[11] P. Sobis, "ALMA WVR maintenance FE components," 2017.

[12] Virginia Diodes. (2018). Mixers - VDI Model: WR4.3SHM, [Online]. Available: `https://www.vadiodes.com/en/products/mixers?id=129`.

[13] P. Sobis, "Advanced Schottky diode receiver front-ends for terahertz applications," Ph. D dissertation, Dept. Microtechnology and nanoscience, Chalmers University of Technology, Gothenburg, Sweden, 2012, ISBN: 978-91-7385-544-0.

[14] A. Y. Tang, "Modelling and characterisation of terahertz planar Schottky diodes," Ph. D dissertation, Dept. Microtechnology and nanoscience, Chalmers University of Technology, Gothenburg, Sweden, 2013, ISBN: 978-91-7385-820-5.

[15] P. Lehikoinen, J. Mallat, P. Piironen, A. Lehto, J. Tuovinene, and A. V. Räisänen, "A 119 GHz planar Schottky diode mixer for a space application," *International Journal of Infrared and Millimeter Waves*, vol. 17, no. 5, pp. 807–818, May 1996. DOI: 10.1007/BF02101389.

[16] P. H. Siegel, R. J. Dengler, I. Mehdi, W. L. Bishop, and T. W. Crowe, "A 200 GHz planar diode subharmonically pumped waveguide mixer with state-of-the-art performance", in *1992 IEEE MTT-S Microwave Symposium Digest*, Jun. 1992, 595–598 vol.2. DOI: 10.1109/MWSYM.1992.188052.

[17] W. Y. Ali-Ahmad, W. L. Bishop, T. W. Crowe, and G. M. Rebeiz, "A 250 GHz planar low noise Schottky receiver," *International Journal of Infrared and Millimeter Waves*, vol. 14, no. 4, pp. 737–748, Apr. 1993. DOI: 10.1007/BF02084284.

[18] S. P. Rea, B. Thomas, and D. N. Matheson, "A 320-360 GHz sub-harmonically pumped image-rejection mixer for earth observation applications," in *2008 33rd International Conference on Infrared, Millimeter and Terahertz Waves*, Sep. 2008. DOI: 10.1109/ICIMW.2008.4665707.

[19] J. L. Hesler, K. Hui, S. He, and T. W. Crowe, "A fixed-tuned 400 GHz subharmonic mixer using planar Schottky diodes," in *Tenth International Symposium on Space Terahertz Technology*, Mar. 1999, pp. 95–99.

[20] K. Hui, J. L. Hesler, D. S. Kurtz, W. L. Bishop, and T. W. Crowe, "A micromachined 585 GHz Schottky mixer", *IEEE Microwave and Guided Wave Letters*, vol. 10, no. 9, pp. 374–376, Sep. 2000. DOI: 10.1109/75.867855.

[21] M. Boheim *et al.*, "A new 140 GHz planar diode finline mixer for radiometer applications", in *1994 24th European Microwave Conference*, vol. 1, Sep. 1994, pp. 664–669. DOI: 10.1109/EUMA.1994.337286.

[22] W. L. Bishop, K. McKinney, R. J. Mattauch, T. W. Crowe, and G. Green, "A novel whiskerless Schottky diode for millimeter and submillimeter wave application", in *1987 IEEE MTT-S International Microwave Symposium Digest*, vol. 2, May 1987, pp. 607–610. DOI: 10.1109/MWSYM.1987.1132483.

[23] S. D. Vogel, "Design and measurements of a novel subharmonically pumped millimeter-wave mixer using two single planar Schottky-barrier diodes", *IEEE Trans. Microw. Theory Techn.*, vol. 44, no. 6, pp. 825–831, Jun. 1996. DOI: 10.1109/22.506440.

[24] A. Hammar *et al.*, "Low noise 874 GHz receivers for the International Submillimetre Airborne Radiometer (ISMAR)", *Review of Scientific Instruments*, vol. 89, no. 5, p. 055 104, 2018. DOI: 10.1063/1.5017583.

[25] W. Schottky, *Phys. Z.*, vol. 41, p. 570, 1940.

[26] R. E. Williams, *Modern GaAs processing methods.* Artech House, Inc., 1990, ISBN: 978-08-9006-343-9.

[27] D. A. Neamen, *Semiconductor physics and devices: basic principles*, 4th, McGraw-Hill international. New York: McGraw-Hill Higher Education, 2012, ISBN: 9780071089029.

[28] P. H. Siegel and A. R. Kerr, “The measured and computed performance of a 140 - 220 GHz Schottky diode mixer”, *IEEE Microw. Theory Techn.*, vol. 32, no. 12, pp. 1579–1590, Dec. 1984. DOI: 10.1109/TMTT.1984.1132897.

[29] W. Bishop, E. Meiburg, R. Mattauch, T. Crowe, and L. Poli, “A micronthickness, planar Schottky diode chip for terahertz applications with theoretical minimum parasitic capacitance,” *IEEE MTT-S International Microwave Symposium Digest*, vol. 3, pp. 1305–1308, May 1990. DOI: 10.1109/MWSYM.1990.99818.

[30] D. M. Pozar, *Microwave Engineering*, 4th ed. Chichester: Wiley, 2012, ISBN: 978-08-9006-343-9.

[31] A. R. Kerr, “Noise and loss in balanced and subharmonically pumped mixers: Part I - Theory,” *IEEE Trans. Microw. Theory Techn.*, vol. 27, no. 12, pp. 938–943, Dec. 1979. DOI: 10.1109/TMTT.1979.1129771.

[32] H. Nyquist, “Thermal agitation of electric charge in conductors,” *Physical review*, vol. 32, no. 1, pp. 110–113, 1928.

[33] J. Johnson, “Thermal agitation of electricity in conductors,” *Physical review*, vol. 32, no. 1, pp. 97–109, 1928.

[34] T. W. Crowe and R. J. Mattauch, “Analysis and optimization of millimeter- and submillimeter-wavelength mixer diodes,” *IEEE Trans. Microw. Theory Techn.*, vol. 35, no. 2, pp. 159–168, Feb. 1987. DOI: 10.1109/TMTT.1987.1133618.

[35] C. Dragone, “Analysis of thermal and shot noise in pumped resistive diodes,” *The Bell System Technical Journal*, vol. 47, pp. 1883–1902, Nov. 1968. DOI: 10.1002/j.1538-7305.1968.tb01095.x.

[36] A. A. M. Saleh, “Theory of resistive mixers”, Cambridge, MA: MIT Press, 1971.

[37] A. R. Kerr, “Noise and loss in balanced and subharmonically pumped mixers: Part II - Application,” *IEEE Trans. Microw. Theory Techn.*, vol. 27, no. 12, pp. 944–950, Dec. 1979. DOI: 10.1109/TMTT.1979.1129772.

[38] M. Cohn, J. E. Degenford, and B. A. Newman, “Harmonic mixing with an antiparallel diode pair,” *IEEE Trans. Microw. Theory Techn.*, vol. 23, no. 8, pp. 667–673, Aug. 1975. DOI: 10.1109/TMTT.1975.1128646.

[39] P. J. Sobis, N. Wadefalk, A. Emrich, and J. Stake, “A broadband, low noise integrated 340 GHz Schottky diode receiver,” *IEEE Microw. Compon. Lett.*, vol. 22, no. 7, pp. 366–368, Jul. 2012. DOI: 10.1109/LMWC.2012.2202280.

[40] H. Zhao *et al.*, “Development of a 557 GHz GaAs monolithic membrane-diode mixer”, in *2012 International Conference on Indium Phosphide and Related Materials*, Aug. 2012, pp. 102–105. DOI: 10.1109/ICIPRM.2012.6403330.

[41] Keysight Technologies, *Advanced Design System.* 2018. [Online]. Available: https://www.keysight.com/en/pc-1297113/advanced-design-system-ads?cc=SE&lc=eng.

[42] Ansys Inc., *High Frequency Electromagnetic Field Simulator.* 2018. [Online]. Available: https://www.ansys.com/products/electronics/ansys-hfss.

[43] D. Porterfield, J. Hesler, T. Crowe, W. Bishop, and D. Woolard, “Integrated terahertz transmit/receive modules,”, presented at the 33rd Eur. Microwave Conf. Munich, 2003. DOI: 10.1109/EUMC.2003.177730.

[44] S. E. Gunnarsson *et al.*, “A 220 GHz single-chip receiver MMIC with integrated antenna,” *IEEE Microw. Compon. Lett.*, vol. 18, no. 4, pp. 284–286, Apr. 2008. DOI: 10.1109/LMWC.2008.918959.

[45] Y. Yan, Y. B. Karandikar, S. E. Gunnarsson, M. Urteaga, R. Pierson, and H. Zirath, “340 GHz integrated receiver in 250 nm InP DHBT technology,” *IEEE Trans. THz Sci. Technology*, vol. 2, no. 3, pp. 306–313, May 2012. DOI: 10.1109/TTHZ.2012.2189912.

[46] M. Abbasi *et al.*, “Single-chip 220 GHz active heterodyne receiver and transmitter MMICs with on-chip integrated antenna,” *IEEE Microw. Theory Techn.*, vol. 59, no. 2, Feb. 2011. DOI: 10.1109/TMTT.2010.2095028.

[47] American Technical Ceramics. (2018). Typical substrate properties, sputtered and electroplated materials, wafer construction, [Online]. Available: http://www.atceramics.com/thin-film-typical-substrate.aspx?id=6.

[48] A. Maestrini *et al.*, “1200 GHz and 600 GHz Schottky receivers for JUICE-SWI”, presented at the 27th International Symposium on Space Terahertz Technology, Nanjing, 2016.

[49] M. Petersson and P. Sobis, private communication, Jan. 2018.

[50] Epoxy Technology. (2018). Product detail: H20E, [Online]. Available: http://www.epotek.com/site/component/products/productdetail.html?cid[0]=84.

[51] 3M. (2018). 3M Scotch-weld epoxy adhesive 2216, [Online]. Available: https://www.3m.com/3M/en_US/company-us/all-3m-products/~/3M-Scotch-Weld-Epoxy-Adhesive-2216/?N=5002385+3293241721&rt=rud.